UC San Diego

UC San Diego Electronic Theses and Dissertations

Title

Symmetry Breaking in Space and Time within the Navier—Stokes Equations: Data-driven Modeling and Stability Analysis of Laminar—Turbulent Transition

Permalink

https://escholarship.org/uc/item/72w2v297

ISBN

9798171611248

Author

Lin, Cong

Publication Date

2026-10-23

Supplemental Material

https://escholarship.org/uc/item/72w2v297#supplemental

Peer reviewed|Thesis/dissertation

eScholarship.org Powered by the California Digital Library
University of California

UNIVERSITY OF CALIFORNIA SAN DIEGO

Symmetry Breaking in Space and Time within the Navier–Stokes Equations: Data-driven Modeling and Stability Analysis of Laminar–Turbulent Transition

A dissertation submitted in partial satisfaction of the
requirements for the degree Doctor of Philosophy

in

Engineering Sciences (Aerospace Engineering)

by

Cong Lin

Committee in charge:

Professor Oliver T. Schmidt, Chair
Professor Boris Kramer
Professor Sutanu Sarkar
Professor Shabnam J. Semnani

2026

Copyright

Cong Lin, 2026

All rights reserved.

The Dissertation of Cong Lin is approved, and it is acceptable in quality and form for publication on microfilm and electronically.

University of California San Diego

2026

TABLE OF CONTENTS

Dissertation Approval Page iii

Table of Contents iv

List of Figures vi

List of Supplemental Files viii

Acknowledgements ix

Vita xi

Abstract of the Dissertation xii

Chapter 1 Spectral Modal Decomposition of K-Type Boundary Layer Transition 1
1.1 Introduction and Overview 2
1.2 Methods: Data and Modal Decomposition Techniques 3
1.2.1 Symmetry Decomposition (D1) 3
1.2.2 Spectral Proper Orthogonal Decomposition (SPOD) 4
1.3 Direct Numerical Simulation and Validation of K-type Transition 6
1.3.1 Numerical Setup 6
1.3.2 Post-excitation, Pre-transitional Dynamics 9
1.3.3 Transition to Skin-friction Overshoot and Onset of Turbulence 9
1.4 Modal Decomposition Results 11
1.4.1 Harmonic Analysis − Deconstruction and Reconstruction 11
1.5 Conclusion 19

Chapter 2 Boundary Layer Transition as Succession of Temporal and Spatial Symmetry Breaking 21
2.1 Introduction 22
2.2 Methods 25
2.2.1 Spatio–Temporal Symmetry Decomposition 25
2.2.2 Spectral Proper Orthogonal Decomposition (SPOD) 26
2.2.3 Space-Time Proper Orthogonal Decomposition (STPOD) 26
2.3 Extracting the Resonant Fundamental Harmonic Response (FHR) 27
2.4 The Dynamics and Statistics of Temporal & Spatial Symmetry Breaking 31
2.4.1 Onset of Quasi-Periodicity and Aperiodicity 32
2.4.2 Onset of Spanwise Asymmetry 35
2.5 Inter-Modal/Inter-Symmetry Energy Transfer 35
2.6 Concluding Remarks 40

Chapter 3 Nature of Symmetry Breaking Seeds in Laminar–Turbulent Transition: Data-driven Stability Analysis 43

3.1 Introduction 44
3.2 Fundamental Harmonic Response (FHR) and symmetry-based stability framework 49
3.2.1 Direct numerical simulation and dataset 49
3.2.2 Spatio-temporal symmetry decomposition 51
3.2.3 Symmetry-decomposed Navier–Stokes equations and linear-time-periodic (LTP) stability framework 55
3.2.4 Galilean LTP-to-LTI reduction 59
3.3 Linear amplification of symmetry-breaking seeds 62
3.3.1 Seed tracking and data-driven operator inference 62
3.3.2 Eigenspectra, growth-rate consistency, and linearity tests 66
3.3.3 Agreement of operator prediction, STPOD modes and Floquet identity . 69
3.4 Temporal and spatial symmetry-breaking seed mechanics 70
3.4.1 Temporal symmetry breaking physics: symmetric seed 71
3.4.2 Spatial symmetry breaking physics: anti-symmetric seed 73
3.5 Discussion: Nonlinear symmetry breaking feedback on harmonic solutions 75
3.5.1 Impact on the skin friction curve and C_f-maximum 75
3.5.2 Implications for harmonic Navier–Stokes methods 77
3.6 Conclusions 81
3.7 Acknowledgements 85
3.8 Appendix 85
3.8.1 Exact semi-discrete descriptor systems. 85
3.8.2 Floquet Theory and Identities 87
3.8.3 Methods 88
3.8.4 Galilean Transformations in Boundary Layer Stability Analysis 91

Bibliography 97

LIST OF FIGURES

Figure 1.1. Flow regimes from deterministic K-type transition to turbulence. 6

Figure 1.2. DNS validation using disturbance-mode amplitudes and skin friction. 8

Figure 1.3. Superposition of the dominant SPOD modes $\psi_{f_n}^{(1)}$ at harmonic frequencies n in ascending order ($n = 1, 2, 4, 8, 16, 32$ harmonics). Q-criterion isosurfaces colored in the stream-wise velocity ($Q = 10^3$), corresponding to $Re_x = 2.25 - 4.75 \times 10^5$. 11

Figure 1.4. SPOD modal energy spectra for a) $\mathbf{q}_S$ and b) $\mathbf{q}_A$ symmetric and anti-symmetric components, respectively, and c) Streamwise energetic development of individual dominant SPOD modes $\psi_{f_n}^{(1)}$ at the harmonic peaks $n \in \mathbb{Z}$ and different orders of their linear combinations. 14

Figure 1.5. Harmonic transition structure at four phases of the fundamental period. . . . 18

Figure 2.1. Temporal and spatial symmetry-breaking regimes in K-type transition. . . . 23

Figure 2.2. SPOD energy spectra for (a) $\mathbf{q}^S$ symmetric and (b) $\mathbf{q}^A$ anti-sym. components; compare to Sayadi et al. (2013). (c) Superposition of N_n={1, 2, 4, 8, 16, 32} dominant SPOD modes $\psi_n^{(1)}$ at harmonic peaks f_n (2.7); Q-criterion ($Q = 10^3$) colored by u. 29

Figure 2.3. Streamwise local spectra and progressive STPOD-mode ablation. 30

Figure 2.4. Symmetric and anti-symmetric STPOD spectra and modal amplitudes. . . . 31

Figure 2.5. STPOD symmetry-breaking mode trajectories, structures, and periodicity. 33

Figure 2.6. Inter-modal and inter-symmetry energy-transfer and production pathways. 38

Figure 3.1. Overview of spatio-temporal symmetry decomposition for K-type transition. 45

Figure 3.2. Periodic formation and convection of the leading symmetric and anti-symmetric seeds over one forcing period. 46

Figure 3.3. Streamwise evolution of the flow dynamics through skin friction and the amplification and decay of distinct flow components. 50

Figure 3.4. Amplitude scale comparison of terms in the symmetric and phase-averaged Navier–Stokes equations. 59

Figure 3.5. Phase-resolved fluctuations and space–time contours used to estimate the moving frame. 63

Figure 3.6. Results of the multi-trajectory Galilean operator inference. 67

Figure 3.7. Formation process of the prototypical time-symmetry-breaking seed. 71

Figure 3.8. Formation process of the prototypical spatial symmetry breaking seed. . . . 73

Figure 3.9. C_f budget for the DNS-conditioned FHR. 78

Figure 3.10. Formation process of the prototypical time-symmetry-breaking seed. 88

Figure 3.11. Floquet identity terms evaluated for representative symmetric STPOD modes that do (e.g. (a) ϕ_1^s and (b) ϕ_2^s) and do not (e.g. (c) ϕ_3^s and higher) satisfy the identity. 89

Figure 3.12. Floquet identity terms evaluated for representative anti-symmetric STPOD modes that do (e.g. (a) ϕ_1^a) and do not (e.g. (b) ϕ_2^a and higher) satisfy the identity. 90

Figure 3.13. The equivalent phase-resolved amplitude and space-time diagrams to Fig. 3.5(a) and Fig. 3.5(b) created with the dominant symmetric and anti-symmetric STPOD modes ϕ_1^s and ϕ_1^a. 95

LIST OF SUPPLEMENTAL FILES

`Lin_Figure_2_1_transition_regimes.gif`

Supplementary Movie 1: Temporal and spatial symmetry-breaking regimes in K-type transition, corresponding to Figure 2.1.

`Lin_Figure_2_5_STPOD_modes.gif`

Supplementary Movie 2: STPOD symmetry-breaking mode trajectories, structures, and periodicity, corresponding to Figure 2.5.

`Lin_Figure_2_6_energy_transfer.gif`

Supplementary Movie 3: Inter-modal and inter-symmetry energy-transfer and production pathways, corresponding to Figure 2.6.

ACKNOWLEDGEMENTS

My gratitude goes first and foremost to my advisor, Professor Oliver T. Schmidt, for his mentorship and support throughout my doctoral studies. He has not only provided expert guidance on fluid mechanics but also allowed me the freedom to explore my own research directions. I am particularly grateful for his teachings and feedback on scientific writing and communication, which have shaped my research and presentation skills. I would also like to thank my committee members, Professors Boris Kramer, Sutanu Sarkar, and Shabnam J. Semnani, for their valuable feedback throughout the different examination stages of my PhD.

I would like to thank the members of the Computational Flow Physics lab: Brandon Yeung, Edward Lowell, Jaein Lee, Eden Taghishokrgozar, Elias Pratschke, and former members Akhil Nekkanti, Tianyi Chu, Christos Papoutsellis. You have not once hesitated to provide me with technical support on the compute clusters, insightful discussions on stability analysis and reduced-order modeling, or feedback on my ideas.

A special thanks to the *squadruple* of the command center, for that we had plenty of very fun and productive days and nights together in the garage, and my partner for her unwavering support and encouragement throughout my journey.

Last but not least, I would like to give a shout-out to my dance crews SD Popping, KnD UCSD, and Ascension UCSD for inspiring my artistic craft and constantly reminding me of a life outside of equations and code. I also thank the friendly baristas and bobaristas at Yun Tea, Camellia Rd, and other shops in Convoy for essentially providing me with a second office and a space for creativity.

Chapters 1–3 of this dissertation are based on work co-authored with Oliver T. Schmidt. Chapter 1, in part, is adapted from "Modal Decomposition of K-Type Boundary Layer Transition," AIAA Paper 2024-0495, published in the *AIAA SciTech 2024 Forum*. Chapter 2, in full, is reproduced from "Boundary Layer Transition as Succession of Temporal and Spatial Symmetry Breaking," published by Cambridge University Press in the *Journal of Fluid Mechanics*, volume

1033 (2026), R4, under the Creative Commons Attribution 4.0 International Licence (CC BY 4.0). Chapter 3, in full, consists of the manuscript "Nature of Symmetry Breaking Seeds in Laminar–Turbulent Transition: Data-driven Stability Analysis," which is to be submitted.

VITA

2016	Bachelor of Science, Mechanical and Process Engineering, Technical University of Darmstadt
2019	Master of Science, Aerospace Engineering, University of Illinois at Urbana–Champaign
2026	Doctor of Philosophy, University of California San Diego

ABSTRACT OF THE DISSERTATION

Symmetry Breaking in Space and Time within the Navier–Stokes Equations: Data-driven Modeling and Stability Analysis of Laminar–Turbulent Transition

by

Cong Lin

Doctor of Philosophy in Engineering Sciences (Aerospace Engineering)

University of California San Diego, 2026

Professor Oliver T. Schmidt, Chair

Boundary layers arise wherever a fluid moves relative to a solid surface. They govern key performance limits in aerospace and marine vehicles, energy systems and thermal management of high-performance electronics. Whether they remain laminar or become turbulent affects drag, heat transfer, mixing, noise and engineering performance. Yet laminar–turbulent transition remains a central unresolved problem in fluid dynamics.

This dissertation examines that transition through a unifying dynamical-systems framework: turbulence emerges through progressive symmetry breaking in space and time. To this end, we derive symmetry-decomposed Navier–Stokes equations and a corresponding stability

framework for temporal and spatial symmetry breaking about a symmetry-preserving reference state. High-fidelity simulations reveal that canonical transition first proceeds through precisely such a state: fully nonlinear and rich in turbulence-like vortical structure, yet time-periodic and reflection-symmetric. Unsupervised, energy-optimal modal decomposition then identifies dominant space-time structures through which this ordered state loses time-periodicity and spatial symmetry, while energy-transfer analysis reveals how they channel energy from the ordered state into broadband turbulence. Using system identification and data-driven stability analysis, we identify their earliest dynamical behavior as unstable Floquet modes of the nonlinear periodic state.

Later, at finite amplitude, symmetry breaking stresses feed back nonlinearly on the deterministic state that produced them. At peak skin friction, they oppose wall shear and supply a crucial momentum-inhibiting feedback to close the deterministic momentum balance. Symmetry breaking therefore not only initiates departure from deterministic behavior; it also provides the nonlinear saturation required to complete transition toward turbulence. Together, these results show that in deterministic transition, symmetry breaking is not random disorder appearing late in transition. It is the mechanism by which organized states lose stability, acquire new degrees of freedom and unlock broadband turbulent dynamics.

More broadly, the symmetry-decomposed governing and stability equations developed here provide a general mathematical framework for characterizing how organized nonlinear states lose symmetry and progress toward chaos. Combined with data-driven operator learning, this framework enables interpretable scientific machine learning directly from high-dimensional data without intrusive access to the underlying solver. The resulting approach is transferable to fluid flows and other complex dynamical systems.

Chapter 1

Spectral Modal Decomposition of K-Type Boundary Layer Transition

Abstract

We perform a data-driven analysis of deterministic K-type boundary layer transition using direct numerical simulation (DNS), D1 symmetry decomposition and Spectral Proper Orthogonal Decomposition (SPOD). After validating the DNS against established transition phenomenology, we identify the dominant frequency-domain coherent structures in the symmetric and anti-symmetric flow components. Our study is in part a data-driven counterpart to the harmonic-balance analysis of Rigas et al. (2021): we determine which pre-turbulence transition mechanisms can be reconstructed with increasing numbers of Fourier-type modes at the fundamental frequency and its harmonics. The progressive harmonic reconstructions capture the formation of localized vortical structures through destructive superposition, but require many harmonics for convergence. The 32-harmonic reconstruction converges to the phase mean, or fundamental harmonic response (FHR), providing a statistical benchmark for the complete deterministic harmonic transition scenario.

1.1 Introduction and Overview

Boundary layer transition caused by deterministic input actuation has been the subject of extensive study over the last few decades. In the seminal study from 1995, Rist and Fasel (1995) conducted direct numerical simulations (DNS) of controlled K-type transition in a flat-plate boundary layer, successfully reproducing wind tunnel experiments by Kachanov et al. Kachanov et al. (1985); Kachanov and Levchenko (1984) and providing valuable insights into structures within the fundamental breakdown process. Bake et al. (2002) (2002) laid the foundational groundwork for studying the complex flow randomization process that transforms the deterministic actuation into developed boundary layer turbulence through amplification of disturbances from the background and freestream. Sayadi et al. (2013) (2013) conducted comprehensive studies of complete K- and H-type transitions, demonstrating their convergence towards fully developed turbulence after the skin-friction overshoot and revealing that a periodic hairpin-packet solution in the late stages of transition yields statistical properties resembling developed turbulence. Most recently, Rigas et al. (2021) (2021) extended linear input/output (resolvent) analysis to account for nonlinear triadic interactions via a harmonic balance model with a minimal frequency-wavenumber basis, enabling the identification of worst-case finite-amplitude disturbances that maximize drag and solving various transition scenarios up to the skin friction maximum directly within the frequency domain. In our study, we use statistical modal analysis to examine the harmonic content and reflection symmetry of this controlled transition scenario.

After re-creating the controlled K-type transition scenario and validating it against the literature Rist and Fasel (1995); Sayadi et al. (2013), we use a D1 symmetry decomposition to distinguish the symmetric and anti-symmetric components. We compare our data-driven analysis to the Harmonic Balance approach in Rigas et al. (2021) by reproducing significant pre-turbulence transition mechanisms using SPOD modes at the fundamental frequency and its

harmonics. We then identify the linear combinations of SPOD modes needed to reconstruct hairpin vortices and the complete dominant harmonic transition mechanism. Their convergence to the phase mean, or FHR, quantifies the harmonic resolution required to represent the spatially localized structures of this controlled transition scenario.

1.2 Methods: Data and Modal Decomposition Techniques

In this section, we present the D1 symmetry decomposition and SPOD analysis used to compute coherent structures from the spatio-temporal flow field $\mathbf{q}(\mathbf{x},t)$.

1.2.1 Symmetry Decomposition (D1)

The symmetric component of the flow field is defined as

$$\mathbf{q}_S(x,y,z) = \frac{1}{2}\begin{bmatrix} u(x,y,z)+u(x,y,-z) \\ v(x,y,z)+v(x,y,-z) \\ w(x,y,z)-w(x,y,-z) \end{bmatrix} \tag{1.1}$$

while the anti-symmetric component is given by

$$\mathbf{q}_A(x,y,z) = \frac{1}{2}\begin{bmatrix} u(x,y,z)-u(x,y,-z) \\ v(x,y,z)-v(x,y,-z) \\ w(x,y,z)+w(x,y,-z) \end{bmatrix}. \tag{1.2}$$

In our analysis, we leverage the natural transverse D1 (Dihedral group 1) symmetry stemming from the simulation setup and the symmetry of the actuation. While not conventionally termed a *modal* decomposition method, a symmetry decomposition can be applied to the DNS data before each modal decomposition method − the additivity and linearity properties allow for its application without a loss of generality. As recommended by Sirovich (1987b), this ensures the expected statistical symmetries of resulting modes, generating either symmetric or

anti-symmetric modes without modes that are a mixture of both. Furthermore, this approach effectively cuts the computational and memory requirements in half, as the modal decompositions can then be separately applied to the symmetric and anti-symmetric components one at a time. Physically, this method also provides additional insights into the downstream mechanisms and statistics of symmetry breaking in the present flow system.

1.2.2 Spectral Proper Orthogonal Decomposition (SPOD)

Spectral Proper Orthogonal Decomposition (SPOD) Towne et al. (2017) identifies frequency-domain coherent structures that optimally represent the second-order statistics of a statistically stationary flow. Under statistical stationarity, the space-time correlation tensor depends only on the time difference $\tau = t - t'$, i.e., $\boldsymbol{C}(\mathbf{x},\mathbf{x}',t,t') \rightarrow \boldsymbol{C}(\mathbf{x},\mathbf{x}',\tau)$, which allows the cross-spectral density tensor to be defined by the Fourier transform of the two-point space-time correlation tensor:

$$\boldsymbol{S}(\mathbf{x},\mathbf{x}',f) = \int_{-\infty}^{\infty} \boldsymbol{C}(\mathbf{x},\mathbf{x}',\tau) e^{-2\pi i f \tau} d\tau = E\{\hat{\mathbf{q}}(\mathbf{x},f)\hat{\mathbf{q}}^*(\mathbf{x}',f)\} \tag{1.3}$$

where $\hat{\mathbf{q}}$ is the temporal Fourier transform of $\mathbf{q}$. The SPOD modes follow from the frequency-domain Fredholm eigenvalue problem

$$\int_V E\{\hat{\mathbf{q}}(\mathbf{x},f)\hat{\mathbf{q}}^*(\mathbf{x}',f)\}\boldsymbol{W}(\mathbf{x})\psi(\mathbf{x}',f)\,d\mathbf{x}' = \lambda(f)\psi(\mathbf{x},f), \tag{1.4}$$

as a spatial eigenvalue problem in the frequency domain for each frequency f. Thus, the discrete equivalent is realized as

$$\hat{\mathbf{Q}}_{f_k}\hat{\mathbf{Q}}_{f_k}^*\mathbf{W}\boldsymbol{\Psi}_{f_k} = \boldsymbol{\Psi}_{f_k}\boldsymbol{\Lambda}_{f_k}, \tag{1.5}$$

with $\hat{\mathbf{Q}}_{f_k}$ denoting the Fourier realizations matrix at each discrete frequency f_k, that stores different realizations of the Fourier modes $\hat{\mathbf{q}}(\mathbf{x},f_k)$ as the flow evolves. For further details on the SPOD algorithm we refer to Towne et al. (2018). The eigenvectors $\boldsymbol{\Psi}_{f_k}$ are the SPOD modes

ranked in column-order at frequency f_k and the eigenvalues $\mathbf{\Lambda}_{f_k}$ are the corresponding modal energies of each mode. Algorithmically, SPOD uses Welch's method Welch (1967a) to estimate the spectral densities.

SPOD modes are single-frequency coherent structures that are orthogonal in space-time indefinitely and optimally capture the variance of the data at that frequency. They can thus be viewed as optimal Fourier modes and are formally equivalent to resolvent modes in the case of white noise forcing as shown by Towne et al. (2018).

1.3 Direct Numerical Simulation and Validation of K-type Transition

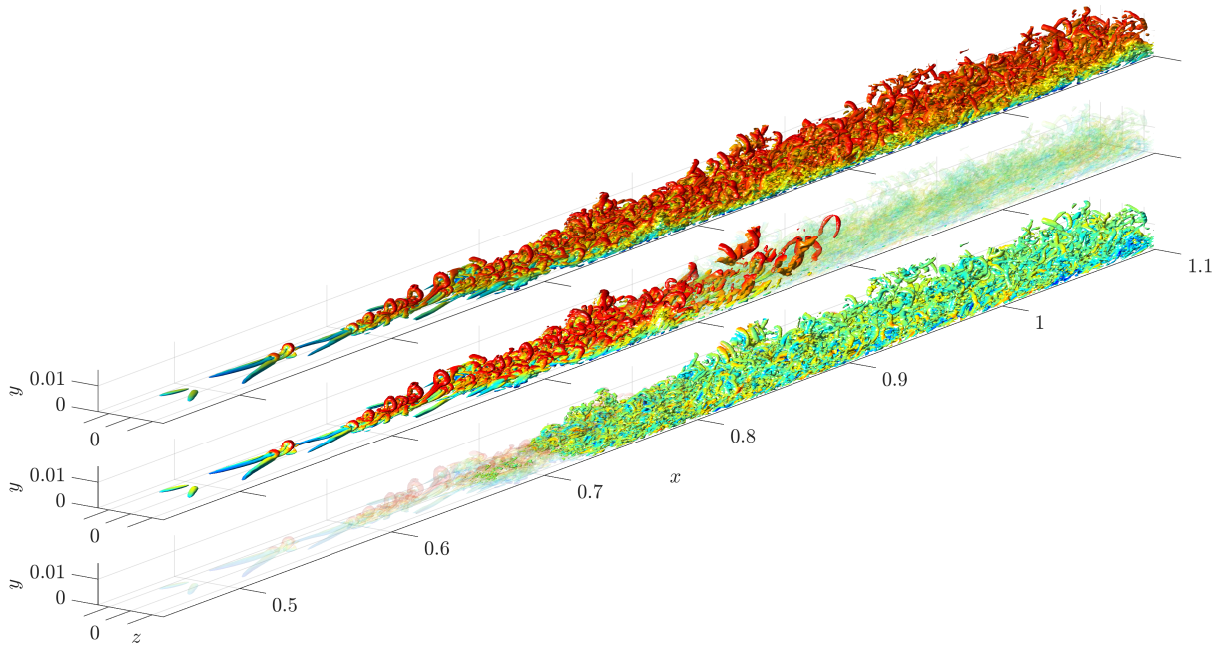


Figure 1.1. Regimes of the transition process − deterministic to turbulent. Top: instantaneous DNS snapshot; middle: phase mean, or fundamental harmonic response (FHR), $\tilde{\mathbf{q}}$; bottom: cyclo-stationary component $\mathbf{q}''$. Q-criterion isosurfaces colored in the stream-wise velocities of the respective quantities ($Q = 10^3$), corresponding to $Re_x = 2.25 - 5.5 \times 10^5$.

1.3.1 Numerical Setup

Our numerical setup takes inspiration from previous studies by Sayadi et al. (2013) and Fasel et al. (1990) that computed K- and H-type transitions. The inlet Reynolds number (taken to be the non-dimensional reference length) from the leading edge is $Re_x = xU_\infty/\nu = 10^5$, where the kinematic viscosity is $\nu = 2 \times 10^{-6}$. We use a Mach number of $M = U_\infty/c_\infty = 0.2$ making this flow weakly compressible. The computational domain and resolution by Sayadi et al. (2013) are used as a reference, however, we truncate the domain to minimize computational cost while retaining the required transition physics. With a dimensional reference length scale of $x_0 = 0.2$, our domain begins at one reference length scale from the leading edge (at $Re_x = 10^5$) and spans

$1 < x/x_0 < 5.5$ in the streamwise, $0 < y/x_0 < 1$ in the wall-normal and $-0.075 < z/x_0 < 0.075$ in the spanwise direction. This allows us to fully capture one instability wave in the span, while excluding the region of pure fully developed turbulence onset from Sayadi et al. (2013). We opt to truncate the region of fully turbulent onset, as we are mainly interested in the region of transition to turbulence and based on results from Sayadi et al. (2013), our domain extends sufficiently far into the turbulent section for all turbulence metrics to collapse to self-similarity.

Our DNS mesh consists of two regions, a finer wall region, and a coarser free stream region, each comprised of purely Cartesian cells with a single layer of polyhedral cells connecting them. We fully resolve the wall region ($0 < y/x_0 < 0.15$) such that the vertical height of the cells closest to the wall is $y^+ \equiv yu^*/\nu < 1$ in viscous wall units. The wall region mesh is resolved with $N_x = 5600$ and $N_z = 128$ cells uniformly in the streamwise and spanwise directions, respectively, and $N_y = 257$ cells in the wall-normal direction with a geometric refinement rate towards the wall to fully resolve the wall turbulence.

For the calculation of the DNS we use the compressible flow solver CharLES Brès et al. (2017) in DNS mode without subgrid scale and wall models. At the domain inlet, the laminar boundary condition is derived from the compressible Blasius self-similar solution for $Re_x = 10^5$. Unlike the previous studies, our outflow condition is a non-reflecting Navier-Stokes Characteristics-based Boundary Condition (NSCBC), combined with a volumetric sponge that spans $5.0 < x/x_0 < 5.5$ to absorb any remaining acoustic reflections and ensure a smooth outflow. The far-field boundary follows the same types of boundary conditions as the outlet, with a sponge in the region $y/x_0 > 0.75$. The spanwise boundaries are periodic. Lastly, the wall has a no-slip and no-flow condition everywhere except at the disturbance strip that is located at $1.36 < x/x_0 < 1.56$. The deterministic harmonic excitation at this disturbance strip is given by

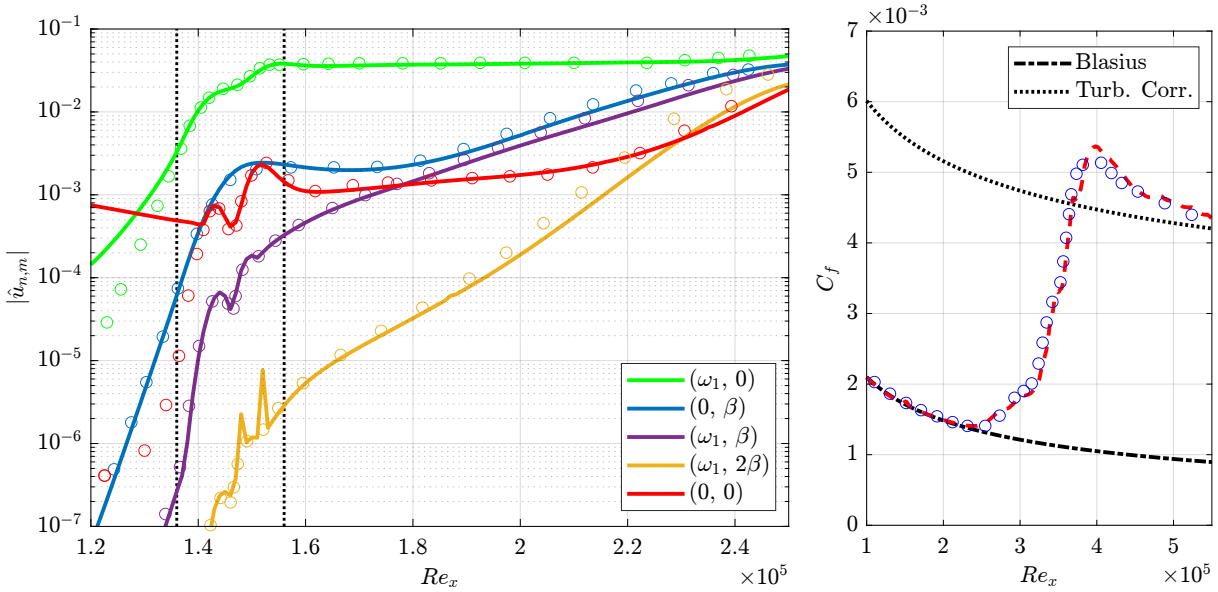
$$v(x,z,t) = A_a v_a(x)\sin(\omega_1 t) + A_s v_s(x)\cos(\beta z), \tag{1.6}$$

where $A_a = 5 \times 10^{-3}$ and $A_s = 1.3 \times 10^{-4}$ are constant factors. Concretely, the function consists

of

$$v_a(x) = \begin{cases} 15.1875\xi^5 - 35.4375\xi^4 + 20.25\xi^3, & \text{if } x_1 < x \leq x_m \\ -v_a(2x_m - x), & \text{if } x_m < x \leq x_2 \end{cases}$$
$$v_s(x) = \begin{cases} -3\xi^4 + 4\xi^3, & \text{if } x_1 < x \leq x_m \\ v_s(2x_m - x), & \text{if } x_m < x \leq x_2, \end{cases} \tag{1.7}$$

with $x_1 = 1.36x_0$, $x_2 = 1.56x_0$ and $x_m = (x_1 + x_2)/2$. Thus, there is a spanwise homogeneous part that features a fixed 5th-order polynomial shape function $v_a(x)$ modulated with a sinusoidal signal of fundamental frequency ω_1 in time and a spanwise oblique part that has fixed sinusoidal shape in z with wavenumber β and a 4th order polynomial $v_s(x)$ for weak steady inflow.



(a) **(b)**

Figure 1.2. DNS results and validation: **a)** stream-wise development of double Fourier mode $(n\omega_1, m\beta)$ amplitudes plotted against Rist and Fasel (1995), vertical dotted lines indicate the extent of disturbance strip; **b)** C_f skin friction overshoot plotted against Sayadi et al. (2013) ($C_f^{turb} = 0.455/\ln^2(0.06Re_x)$ correlation by White (2006)).

1.3.2 Post-excitation, Pre-transitional Dynamics

Fig.1.2a demonstrates a notable agreement with the literature Rist and Fasel (1995). The applied forcing creates initially planar modal Tollmien-Schlichting (TS) waves $(\omega_1, 0)$ and streaks $(0, \beta)$, at the given fundamental frequency and spanwise wavelength outlined in eq.(1.6). Nonlinear interactions then generate harmonics $(n\omega_1, m\beta)$ at integer multiples $n, m \in \mathbb{Z}$ of the fundamental frequency and wavelength as the flow develops. As perturbations progress in the streamwise direction, the streaks $(0, \beta)$, the oblique TS wave (ω_1, β), and the spanwise harmonic $(\omega_1, 2\beta)$ experience rapid amplification, driven by non-modal transient growth (lift-up mechanism) and other nonlinear interactions. The self-interaction of these higher modes, upon reaching high amplitudes, results in energy back-scattering to the mean-flow harmonic $(0, 0)$, leading to the departure of the mean flow from the Blasius base-flow and the growth of mean flow deformation. These mechanisms collectively lead to the formation of Λ-shaped vortices, which become streamwise elongated and lift away from the wall $-$ eventually evolving into the characteristic hairpin vortices in the later stages of transition. The further streamwise flow development towards the skin friction ($C_f = 2\tau_w/U_\infty^2$) maximum is governed by the rise and amplitude growth of increasingly higher harmonics via a cascade of nonlinear interactions.

1.3.3 Transition to Skin-friction Overshoot and Onset of Turbulence

In Fig.1.2b, the streamwise development of skin friction coefficient (C_f) is found to be in good agreement with DNS data computed by Sayadi et al. (2013), where we remark minor differences due to differences in the spanwise excitation function. Fig.1.2b and Fig.1.1 shows the departure of the C_f value from the laminar Blasius solution around $Re_x = 2.4 \times 10^5$ ($x = 0.48$), coinciding with the appearance of Λ vortices in that region. These Λ vortices are aligned in K-type transitions and get lifted away from the wall and progressively stretched out as they travel down the streamwise direction. They develop into hairpin vortices as their "heads" bulge further up into the freestream, transforming into Ω ring-like vortex heads via self-induction

Bake et al. (2002). The instantaneous snapshot of our DNS data in Fig.1.1 (top) reveals these organized vortical structures in the transitional region that are characteristic for K-type transition, resembling results by Bake et al. (2002); Sayadi et al. (2013); Wu and Moin (2009).

As analyzed by Bake et al. (2002), the formation of Ω ring-like vortices at the tip of the Λ-vortices initiates an intricate flow randomization mechanism. In their initial stage, these vortices are highly sensitive to background perturbations while being accompanied by regions of very high induction and shear. These perturbed vortices strongly influence the surrounding fluid and particularly the adjacent wall region where this generates increasingly disturbed instantaneous pressure fields from one instance to the next. This in turn directly modifies the vorticity production at the wall for upcoming new instances. More downstream, the interaction of vortical structures from different disturbance periods leads to further amplification of background disturbances that generate new increasingly non-periodic, *chaotic* structures. With increasing randomization the eventual breakdown to chaos occurs with characteristics typical for a turbulent boundary layer.

In the later stages of transition, characterized by broken periodicity and increasing asymmetry, hairpin packets evolve into more convolved hairpin "forests", creating a self-sustaining auto-generation mechanism that reproduces the statistical properties of developed turbulence as shown by Sayadi et al. (2013). The distinct overshoot in the present K-type transition is observed that is absent in bypass transitions, e.g. Wu and Moin (2010). Fig. 1.2b indicates that after the skin-friction maximum occurs, C_f and the statistics asymptotically collapse onto the turbulent correlations, demonstrating good alignment with the literature and indicating the sufficient capture of the transitional region within our domain.

1.4 Modal Decomposition Results

This analysis section follows a structured progression from upstream to downstream, employing methods tailored to analyze the local dynamics and statistics of each region. Given the initially periodic nature of the flow – whether viewed as deterministically periodic in the early stages or "statistically periodic" (i.e., *cyclo-stationary*) later on – we begin with statistical harmonic analysis tools. These tools are well-suited for investigating the earlier transition stages up to approximately the point of maximum skin friction.

1.4.1 Harmonic Analysis – Deconstruction and Reconstruction

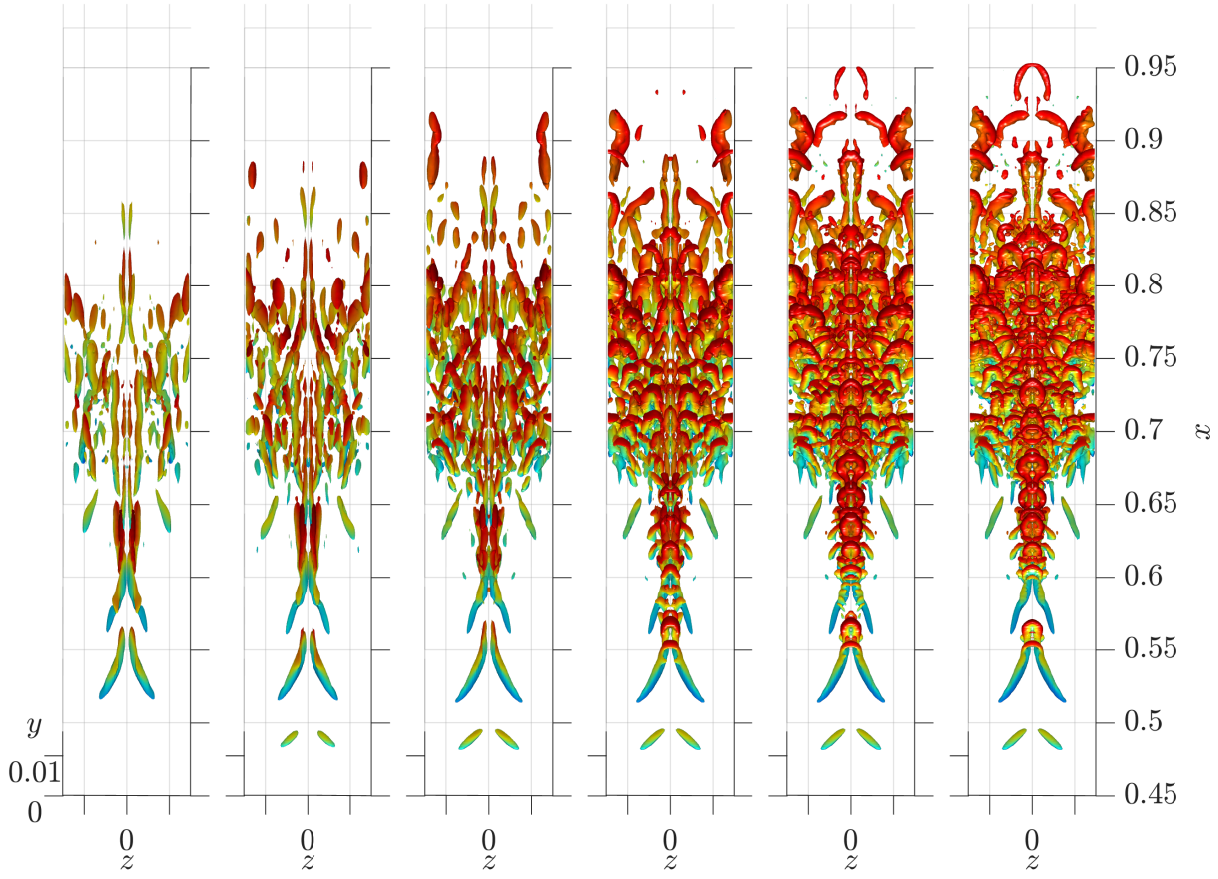


Figure 1.3. Superposition of the dominant SPOD modes $\psi^{(1)}_{f_n}$ at harmonic frequencies n in ascending order ($n = 1, 2, 4, 8, 16, 32$ harmonics). Q-criterion isosurfaces colored in the streamwise velocity ($Q = 10^3$), corresponding to $Re_x = 2.25 - 4.75 \times 10^5$.

The K-type transition, often termed fundamental due to the growth of instabilities caused by the fundamental frequency and its harmonics, has been extensively investigated in the literature using harmonic Fourier analysis methods. However, as this system is a turbulent flow that produces non-periodic statistical data, a naive (long-time) Fourier transform is insufficient, as this kind of estimate of the spectral densities does not converge with increasing data. In order to shed light on the spectral content of this flow and educe the most statistically dominant, convergent, harmonic coherent structures from data that represents this flow at the important frequencies, we apply SPOD to the symmetric and anti-symmetric components $\mathbf{q}_S$ and $\mathbf{q}_A$ individually.

To statistically converge SPOD modes, the best-practice procedure to select the necessary time sampling and spectral estimation parameters for the present K-type DNS is the following: The starting point is the fundamental (angular) excitation frequency $\omega_1 = 55$, which results in a fundamental period of $T_1 = 0.1142$. Since this is a turbulent flow, frequency contents below the lowest fundamental excitation frequency (e.g. subharmonics) could appear and having a sufficient temporal resolution is necessary. Thus we choose to fit eight periods (a convenient power of two) into one N_{FFT} window where we choose a reasonable resolution of $N_{\mathrm{FFT}} = 512$, giving each actuation cycle a resolution of $N_{t,T_1} = 64$ snapshots. This choice results in a physical snapshot sampling time of $\Delta t_{\mathrm{snap}} = 1.785 \times 10^{-3}$. This physical sampling time must be exactly met by an integer multiple of simulation time steps Δt_{DNS}. Using the CFL < 1 condition as constraint, we thus obtain a fixed DNS simulation time step of $\Delta t_{\mathrm{DNS}} = 5.95 \times 10^{-6}$, i.e. we take a snapshot every 300 DNS time steps. The sampling time Δt leads to a sampling frequency of $f_s = 560.22$, thus a Nyquist frequency of $f_{\max} = 280.11$, which has been determined to be sufficient to prevent aliasing. Thereby, the width of one frequency bin Δf, which is also the lowest frequency the SPOD can capture, is then

$$\Delta f = f_{\min} = \frac{1}{N_{\mathrm{FFT}} \Delta t}. \tag{1.8}$$

Now, to reach statistical convergence of the spectral densities we need a reasonable number of blocks (flow realizations) N_{blk}, where

$$N_{\mathrm{blk}} = \left\lfloor \frac{N_t - N_{\mathrm{ovlp}}}{N_{\mathrm{FFT}} - N_{\mathrm{ovlp}}} \right\rfloor, \tag{1.9}$$

with an overlap N_{ovlp} between blocks. We use a best-practice 50% overlap and determine with numerical convergence experiments a number of blocks of $N_{\mathrm{blk}} \geq 20$ as sufficient. This ultimately leads us to (at least) $N_t = 5376$ DNS snapshots.

Figure 1.4 provides insights into the distribution of "signal to noise" between the symmetric and anti-symmetric components in the data through the SPOD spectra for $\mathbf{q}_S$ and $\mathbf{q}_A$. In the $\mathbf{q}_S$ spectrum, a dominance by harmonics of the fundamental forcing frequency $f_1 = 8.75$ is evident, with no discernible sub- or ultra-harmonic content. Furthermore, a strong rank decay at all frequency peaks in $\mathbf{q}_S$ indicates the presence of statistically dominant structures at the fundamental frequency and its harmonics. The first SPOD modes capture on average 77% of the space-time energy among the first 8 harmonic peaks and 57% on average for the remaining higher harmonics. Conversely, the $\mathbf{q}_A$ spectrum is essentially flat, showing no distinct peaks and exhibiting very slow rank decay. Under the present energy norm, the anti-symmetric field therefore has no single globally energy-dominant harmonic SPOD mode. Hence, the statistically dominant harmonic coherent structures in the transition are symmetric. While this might seem intuitive given the symmetric periodic actuation, it is worth noting that many fluid flows with clear D1 symmetries exhibit strong anti-symmetry in their modes (e.g., cylinder flow or general bluff body flows). Our harmonic reconstruction therefore focuses on the symmetric component.

The dominant coherent structures at a given frequency are represented by the symmetric 1st SPOD modes $\psi^{(1)}_{f_k}$, corresponding to the peaks $f_k = f_n$ of Fig. 1.4a. We can assemble them into a linear combination at the harmonics $n \in \mathbb{Z}$

$$\sum_n E\left\{\psi^{(1)}_{f_n} a^{(1)}_{f_n}(n_{\mathrm{b}})\right\}_{n_{\mathrm{b}}} e^{(i2\pi f_n t)} + \bar{\mathbf{q}}(\mathbf{x}) \tag{1.10}$$

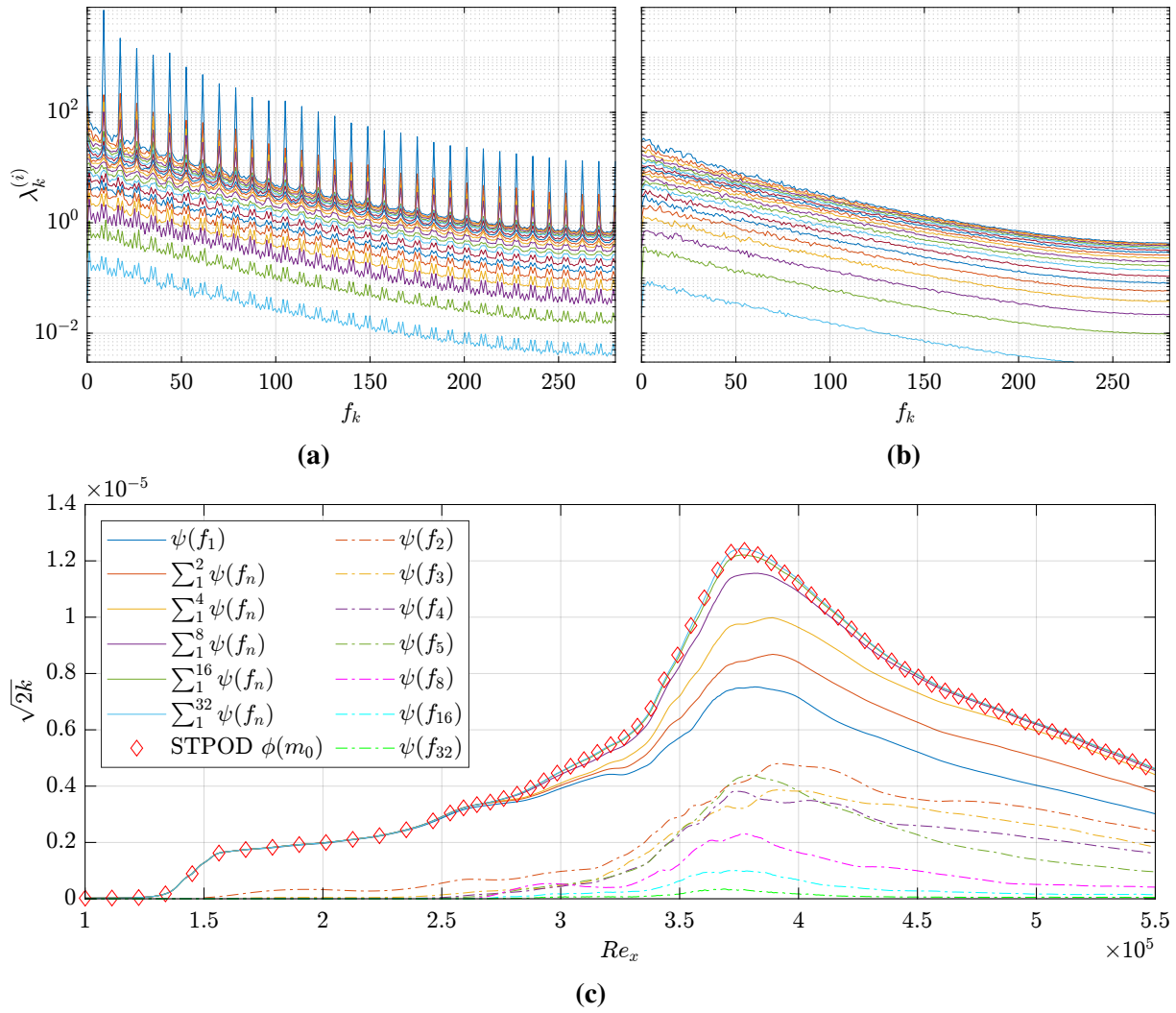


Figure 1.4. SPOD modal energy spectra for a) $\mathbf{q}_S$ and b) $\mathbf{q}_A$ symmetric and anti-symmetric components, respectively, and c) Streamwise energetic development of individual dominant SPOD modes $\psi_{f_n}^{(1)}$ at the harmonic peaks $n \in \mathbb{Z}$ and different orders of their linear combinations.

with the time-averaged mean flow $\bar{\mathbf{q}}(\mathbf{x})$, block-wise expectation operator $E\{\cdot\}_{n_\mathrm{b}}$ and the 1st block-wise SPOD expansion coefficients $a_{f_n}^{(1)}(n_\mathrm{b})$ with $n_\mathrm{b} \in [1, N_\mathrm{blk}]$, to reconstruct the dominant harmonic content of the entire transition process. Then, we can directly compare the results of various harmonic linear combinations of SPOD modes with those obtained using a harmonic balancing method, as deployed in Rigas et al. (2021). It is worth noting that their study also involves one additional decomposition into a spanwise harmonic basis in z. Specifically, eq. (1.10) is effectively an upper bound − as these modes are educed "a posteriori" from fully resolved DNS data − and thereby provides the extent to which an "a priori" truncated frequency domain model would be inadequate in capturing the complete transition mechanism at any given level of truncation n. Fig. 1.3 holistically illustrates the progression of various linear combination levels of SPOD modes at harmonics n with the Q-criterion

$$Q = 1/2(||\boldsymbol{\Omega}||^2 - ||\boldsymbol{S}||^2), \tag{1.11}$$

the second invariant of the velocity gradient tensor that is comprised of the vorticity tensor $\boldsymbol{\Omega}$ and strain rate tensor $\boldsymbol{S}$. Congruent with results by Rigas et al. (2021), indeed only a few SPOD modes are required to accurately reproduce the early transitional, pre-skin-friction-overshoot dynamics. To qualitatively capture hairpin vortices in their early stages, a range of 2-4 SPOD mode harmonics suffice to capture the Λ-vortices, the "legs" of the hairpins. Thereby, various early-stage instability mechanisms including TS, streaks, varicose and sinuous oscillations are well-captured within the 4-harmonic case, as demonstrated in Rigas et al. (2021), so we will not detail this further here. However, capturing even a semblance of the initial train of Ω ring-like vortex "heads", occurring approximately between $x = 0.55 - 0.65$ ($Re_x = 2.75 - 3.25 \times 10^5$), already requires *at least* 8 SPOD harmonics. The second more convolved formation of Ω vortices further downstream around $x = 0.65 - 0.75$ appears qualitatively captured within $n = 16$ harmonics. However, observing e.g. the section $x = 0.55 - 0.6$, one notices that adding these higher harmonics also produces higher wavenumber oscillations within space that are not physical

but merely a byproduct of the choice of a spatial basis that is harmonic in time. It requires additional harmonics to cancel out the oscillations created by preceding modes. Thus, this flow needs a substantial number of harmonics to construct spatially and temporally *localized*, compact structures via destructive superposition, and the present reconstruction achieves this only when all 32 available harmonics are included. Harmonic-balance and other reduced-order models using a harmonic basis may therefore require a comparably broad frequency range to capture the same localized structures under the present reconstruction and energy norm. This raises the question of whether a harmonic Fourier basis, whether in frequency or wavenumber space, is the most suitable choice for simulating or analyzing flow problems characterized by highly localized coherent structures.

Nevertheless, we want to dissect and understand the energetic contribution of individual components. For that purpose, we measure the streamwise energetic progression in form of the RMS of the total fluctuation vector as energy metric, given by

$$\sqrt{2\mathrm{k}} = \sqrt{E\{u'^2 + v'^2 + w'^2\}_{y,z,t}} \tag{1.12}$$

averaged in time, spanwise and/or wall-normal directions. This quantifies the average turbulent kinetic energy square-root of a flow component in any given y-z-plane along the streamwise direction x. The choice of square root is intentional, to be in the units of velocity and to not skew the view towards large or away from small values. Fig. 1.4c details that streamwise energetic development for the optimal modes $\psi_{f_n}^{(1)}$ for both the individual frequency components as well as for different levels of modal superposition. Congruent with Fig. 1.2a, it reveals that the early flow development ($Re_x \leq 2.5 \times 10^5$) is energetically dominated by the fundamental SPOD mode at f_1 (fundamental TS instability) as it carries almost of the oscillatory energy until then, with only the harmonic f_2 trailing at low energy levels beneath it. The higher harmonics only begin to take off beyond $Re_x \geq 2.5 \times 10^5$, congruent with the departure of skin-friction in Fig. 1.2b from the laminar solution and the appearance of Λ-vortices and all of them peak around the

C_f maximum. Observationally, there is a notable variability in the peaking behavior among different frequency components, as some exhibit earlier peaks while others peak later, each with varying maxima. For instance, when f_5 peaks, it demonstrates locally higher energy compared to any other components − also evident in Fig. 1.4a, where $\lambda^{(1)}_{f_5}$ displays greater energy than its adjacent harmonics. This variation in peaking behavior motivates an exploration of different triadic interactions and energy transfers between triad combinations. Methods like Bispectral Mode Decomposition (BMD) Schmidt (2020), as employed by Nekkanti et al. (2022) in the study of forced and unforced jet flows, could offer valuable insights into these dynamics.

More significantly, Fig. 1.4c highlights the convergence of the harmonic superposition of optimal SPOD modes towards the phase mean, or FHR. The superposition of 32 SPOD modes aligns with this statistically prototypical periodic transition scenario. Thus, one statistical benchmark for a harmonic modal decomposition is the phase mean, which encompasses the fundamental frequency and all its harmonics. To develop a notion for "statistically periodic", we briefly introduce the concepts of *cyclo-stationarity* and phase-averaging: A process $\mathbf{q}(\mathbf{x},t)$ is cyclostationary Gardner et al. (2006) if its mean $E\{\mathbf{q}(\mathbf{x},t)\}$ and cross-correlation $\boldsymbol{C}(\mathbf{x},\mathbf{x},t,\tau)$ functions (with some time-delay τ) are periodic with fundamental period T_1, expressed as

$$E\{\mathbf{q}(\mathbf{x},t)\} = E\{\mathbf{q}(\mathbf{x},t+T_1)\},$$
$$\boldsymbol{C}(\mathbf{x},\mathbf{x},t,\tau) = \boldsymbol{C}(\mathbf{x},\mathbf{x},t+T_1,\tau).$$

If $\mathbf{q}(\mathbf{x},t)$ contains a deterministic periodic component at cycle frequency nf_1 (where $f_1 = 1/T_1$ and $n \in \mathbb{Z}$, i.e. an integer multiple of the cycle frequency), it exhibits first-order and second-order (& higher-order) cyclo-stationarity at nf_1. The second-order component $\mathbf{q}''(\mathbf{x},t)$ is defined as

$$\mathbf{q}''(\mathbf{x},t) \equiv \mathbf{q}(\mathbf{x},t) - E\{\mathbf{q}(\mathbf{x},t)\}, \tag{1.13}$$

which separates the deterministic first-order (tonal) component from the stochastic second-order

(turbulent) component. Thus, for data that is phase-locked, the cycle-averaging operator is given by

$$\tilde{\mathbf{q}}(\mathbf{x},t) = \lim_{N_{T_1}\to\infty} \frac{1}{N_{T_1}} \sum_{m=0}^{N_{T_1}} \mathbf{q}(\mathbf{x},t+mT_1), \tag{1.14}$$

to obtain $\tilde{\mathbf{q}}(\mathbf{x},t)$ the periodic phase mean, where N_{T_1} is the number of fundamental periods contained in the data. Optionally, one can use one more decomposition into the stationary long-time mean $\bar{\mathbf{q}}(\mathbf{x})$, such as in the triple decomposition by Hussain and Reynolds (1970) or utilized by Bake et al. (2002), which results in $\mathbf{q}(\mathbf{x},t) = \bar{\mathbf{q}}(\mathbf{x}) + \tilde{\mathbf{q}}(\mathbf{x},t) + \mathbf{q}''(\mathbf{x},t)$.

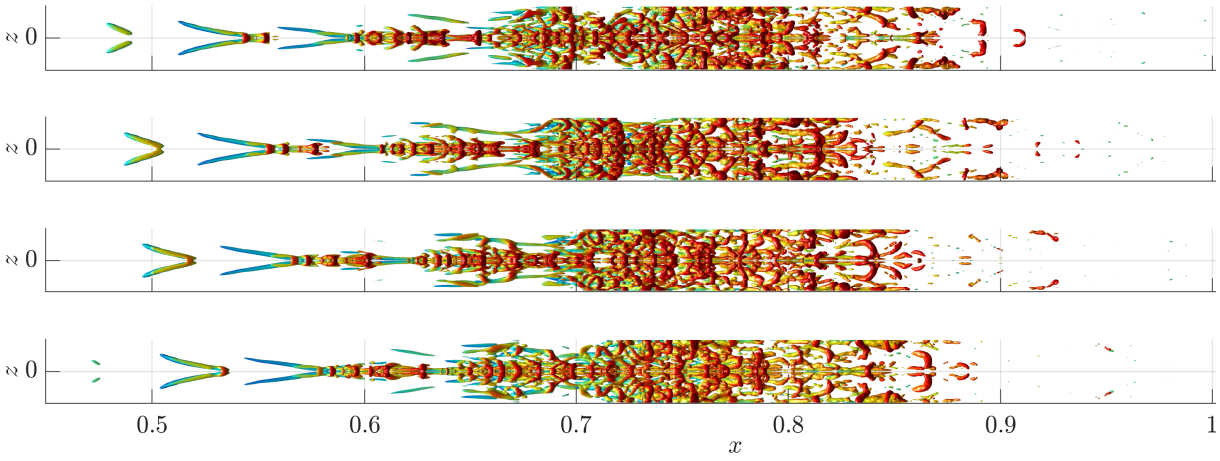


Figure 1.5. Harmonic coherent structure of the transition at four different phases $0T_1$, $0.25T_1$, $0.5T_1$, $0.75T_1$ within the fundamental period T_1 – identified by the phase mean, or FHR, and the order $n = 32$ harmonic superposition of dominant SPOD modes. Q-criterion visualization colored in streamwise velocity ($Q = 10^3$), corresponding to $Re_x = 2.25 - 5 \times 10^5$.

We note that, as it is a priori unknown to what degree a given turbulence dataset is dominated by harmonic statistics, we apply SPOD here that is generally optimal for statistically stationary flows. This is justifiable, as the present flow statistics evolve through periodic, cyclo-stationary and finally statistically stationary (fully turbulent) regimes. On the other hand, with the now a posteriori knowledge on the coherent harmonic content of the flow, one can opt to analyze to what degree this modulates the cyclo-stationary second-order statistics $\mathbf{q}''(\mathbf{x},t)$ within the frequency domain, thus, apply a more optimal spectral modal decomposition method that is specifically geared towards the statistics that are centered around a periodic phase-mean,

see Heidt and Colonius (2023). However, this was not the target of the present harmonic de-/reconstruction study here, as we are interested in the spectral energy content, i.e., the structures and energies contained in each frequency component in the classical Fourier sense.

The phase mean $\tilde{\mathbf{q}}(\mathbf{x},t)$ is therefore the FHR reference against which the convergence of the harmonic reconstruction is assessed in Figs. 1.4c and 1.5.

1.5 Conclusion

Our analysis of K-type boundary layer transition combines DNS validation, D1 symmetry decomposition and SPOD to identify the dominant harmonic structures in the early and transitional regimes. The DNS reproduces established transition phenomenology and skin-friction evolution. The SPOD spectra show that the symmetric component contains globally energy-dominant modes at the forcing frequency and its harmonics, whereas the anti-symmetric field has no single globally energy-dominant harmonic SPOD mode under the present energy norm. Progressive superpositions of the dominant harmonic SPOD modes reconstruct the Λ-vortices and hairpin-vortex heads observed in the DNS. The localized structures require destructive superposition across a broad harmonic range: low-order reconstructions capture the early vortices, while all 32 available harmonics are required for convergence under the present reconstruction and norm. The converged harmonic superposition aligns with the phase mean, or FHR, which contains the complete deterministic harmonic transition scenario. This comparison provides a direct statistical benchmark for harmonic representations of spatially localized transition structures.

Acknowledgments

We acknowledge the NSF for funding this boundary layer transition project under the grant CBET 2046311.

Acknowledgments

Chapter 1, in part, is adapted from Cong Lin and Oliver T. Schmidt, "Modal Decomposition of K-Type Boundary Layer Transition," AIAA Paper 2024-0495, *AIAA SciTech 2024 Forum* (2024), doi:10.2514/6.2024-0495. The dissertation author was the primary investigator and primary author of this work.

Chapter 2

Boundary Layer Transition as Succession of Temporal and Spatial Symmetry Breaking

Abstract

We show that both temporal and spatial symmetry breaking in canonical K-type boundary layer transition arise as organized structures with quantifiable energetic pathways rather than unstructured noise. Before the skin-friction maximum, the flow is described by a periodic, spanwise-symmetric fundamental harmonic response (FHR) to the Tollmien–Schlichting wave. The FHR is spatially compact, produces hairpin packets, and remains fully harmonic despite a turbulence-like appearance, thereby delimiting the deterministic regime. Past this point, a distinct regime change occurs: a hierarchy of quasi-periodic and aperiodic structures emerges, followed shortly by anti-symmetric structures that develop similarly despite no anti-symmetric inputs. We identify these structures as symmetry-decomposed spectral and space-time proper orthogonal modes that resolve the progression from deterministic harmonics to broadband dynamics. We introduce inter-modal and inter-symmetry energy budgets derived from symmetry-decomposed Navier–Stokes equations. They reveal a directed energy transfer from the FHR into the leading temporal and spatial symmetry breaking modes and, subsequently, into broadband residual fluctuations, showing that broadband dynamics grow only once inter-modal transfer is active, while inter-symmetry transfer also strongly amplifies broadband anti-symmetric fluctuations

once asymmetry is present. These key insights support a view of laminar-turbulent transition as a sequence of symmetry breaking events, energetically driven by dominant space-time modes that route energy from harmonic flow to broadband turbulence.

2.1 Introduction

Boundary layer transition through deterministic input actuation has been extensively studied to understand fundamental mechanisms underlying the path to turbulence. Fasel et al. (1990) and Rist and Fasel (1995) conducted seminal direct numerical simulations (DNS) of controlled K-type transition in flat-plate boundary layers, successfully reproducing wind tunnel experiments by Klebanoff et al. (1962); Kachanov et al. (1977); Kachanov and Levchenko (1984). Bake et al. (2002) studied, through a comparison of DNS and experiments, the complex flow randomization process that transforms small disturbances into developed boundary layer turbulence, providing local phenomenological insights into the breakdown of organized structures. Sayadi et al. (2013) demonstrated that complete K- and H-type transitions converge towards fully developed turbulence after the skin-friction overshoot, revealing that initially periodic "hairpin packets" eventually produce statistical properties of fully developed turbulence. Towards the stability analysis of canonical transition, Herbert (1988) established a framework for analyzing secondary instability mechanisms in the K- and H-type transition scenarios. Monokrousos et al. (2010) identified optimal forcing mechanisms and initial conditions for instability growth in the Blasius boundary layer, while Cherubini et al. (2011) investigated optimal perturbations and minimal seeds using time-domain optimization approaches. Rigas et al. (2021) extended input/output analysis to account for nonlinear triadic interactions via harmonic balance models, solving transition scenarios up to before the skin friction maximum (C_f^{max}) within the frequency domain.

Modal analysis has been a valuable tool for identifying coherent structures in transitional flows. Rempfer and Fasel (1994a,b) pioneered the application of proper orthogonal decomposi-

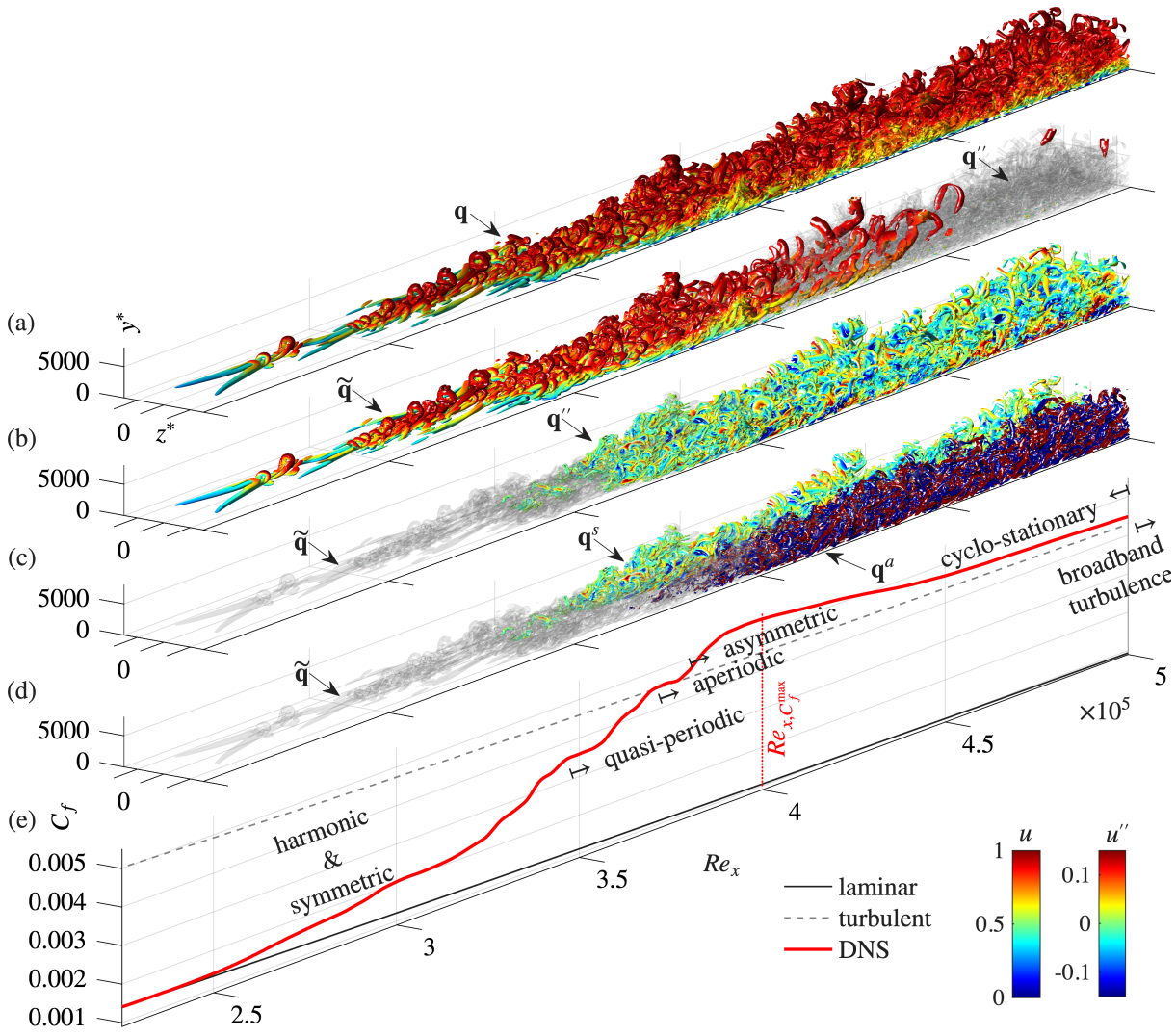


Figure 2.1. Regimes of the transition process. (a) Instantaneous snapshot of full DNS data $\mathbf{q}$. (b) Fundamental harmonic response $\tilde{\mathbf{q}}$. (c) Cyclo-stationary fluctuation $\mathbf{q}'' = \mathbf{q} - \tilde{\mathbf{q}}$. (d) Symmetric $\mathbf{q}^s$ and anti-symmetric $\mathbf{q}^a$ components of temporal and spatial symmetry breaking ($\mathbf{q}'' = \mathbf{q}^s + \mathbf{q}^a$). Q-criterion isosurfaces (all $Q = 10^3$); colored in the respective u-velocities (w-velocity for $\mathbf{q}^a$). (e) Regimes labeled on the C_f graph. See movie 1.

tion (POD) (Sirovich, 1987a; Aubry, 1991) to identify three-dimensional coherent structures and their dynamics in K-type transition. Recent advances in modal decomposition include spectral POD (Lumley, 1970; Towne et al., 2018) for extracting frequency domain modes and space-time POD (Schmidt and Schmid, 2019; Frame and Towne, 2023) for general spatio-temporal modes without imposing assumptions on time dynamics. Both methods have been applied to data from fully turbulent boundary layers (Tutkun and George, 2017; Hack and Schmidt, 2021). Heidt and Colonius (2024) extended SPOD to harmonically forced flows, assuming a frequency domain ansatz with specific periodic modal forms.

Despite these advances, the specific mechanisms driving the breaking of temporal (periodicity) and spatial (spanwise) symmetries, the hallmark phenomena of chaos and turbulence in deterministic transition, remain unclear. While the roots of aperiodicity/asymmetry are small disturbances (of numerical or physical nature) in time/space, to which the flow is inherently sensitive, the resulting transition manifests via energetically interacting coherent structures. In figure 2.1, we provide an overview of the streamwise development of flow dynamics and symmetries: The initially periodic and symmetric flow departs from the laminar solution and undergoes temporal and spatial symmetry breaking, marked by increasing non-periodicity and asymmetry, as it progresses through the C_f^{max}. Afterwards, the cyclo-stationary state converges to statistical stationarity as the statistics asymptotically collapse onto turbulent correlations (White, 2006). Throughout our analysis, we track the evolution from deterministic periodic states to quasi-periodic and broadband dynamics, and characterize a variety of coherent structures for these specific regimes. We demonstrate that both temporal and spatial symmetry breaking are identifiable as organized, energetically dominant modes with distinct dynamical properties. Finally, by analyzing their energy transfer budgets, we reveal that these modes act as a conduit, directing energy from deterministic to broadband dynamics.

2.2 Methods

We compute the DNS of K-type transition with the *CharLES* solver on a structured mesh, satisfying $y^+ < 1$ across the entire Reynolds number range from $Re_x = 1 \times 10^5$ to 6.5×10^5. Transition is triggered by a forcing strip that introduces a periodic ($f_1 = 8.75$) Tollmien-Schlichting (TS) wave with a weak symmetric peak ($f_0 = 0$). For details on the numerics and validation, we refer the reader to Lin and Schmidt (2024). To converge the dominant modes, we sample a dataset of 198 forcing periods ($T_1 = 1/f_1$) with 128 DNS snapshots each.

2.2.1 Spatio–Temporal Symmetry Decomposition

To study the transition process through the lens of spatial and temporal symmetry breaking, we introduce the following decomposition of the flow field:

$$\begin{aligned}\mathbf{q}(\mathbf{x},t) = \underbrace{\mathbf{q}^S(\mathbf{x},t)}_{\text{symmetric}} + \underbrace{\mathbf{q}^A(\mathbf{x},t)}_{\text{anti-symmetric}} &= \underbrace{\tilde{\mathbf{q}}(\mathbf{x},t)}_{\text{harmonics (FHR)}} + \overbrace{\underbrace{\mathbf{q}^s(\mathbf{x},t)}_{\text{sym. fluctuation}} + \underbrace{\mathbf{q}^a(\mathbf{x},t)}_{\text{anti-sym. fluctuation}}}^{\text{cyclo-stat. fluctuation } \mathbf{q}''} \\ &= \underbrace{\tilde{\mathbf{q}}(\mathbf{x},t)}_{\text{sym. periodic}} + \underbrace{\mathbf{q}^{\bullet}(\mathbf{x},t)}_{\text{sym. quasi-periodic}} + \underbrace{\mathbf{q}^{\circ}(\mathbf{x},t)}_{\text{sym. broadband}} + \underbrace{\mathbf{q}^{\blacktriangle}(\mathbf{x},t)}_{\text{anti-sym. quasi-periodic}} + \underbrace{\mathbf{q}^{\triangle}(\mathbf{x},t)}_{\text{anti-sym. broadband}}.\end{aligned} \tag{2.1}$$

Here, the superscripts encode spatial symmetry, while the symbols $\{\bullet/\blacktriangle, \circ/\triangle\}$ distinguish quasi-periodic mode dynamics from broadband (aperiodic) residual dynamics. The S/A components in the first line of (2.1) are obtained by the transverse D_1 (dihedral group 1) symmetry decomposition (Sirovich, 1987b) about the $z = 0$ midplane as

$$\mathbf{q}^{S/A}(x,y,z,t) = \frac{1}{2}\begin{bmatrix} u(x,y,z,t) \pm u(x,y,-z,t) \\ v(x,y,z,t) \pm v(x,y,-z,t) \\ w(x,y,z,t) \mp w(x,y,-z,t) \end{bmatrix}, \tag{2.2}$$

with the top (bottom) signs yielding $\mathbf{q}^S$ ($\mathbf{q}^A$). By contrast, separating periodic, quasi-periodic and stochastic contributions in the second line of (2.1) requires the modal decompositions introduced

below. For the K-type transition scenario, the deterministic *fundamental harmonic response* (FHR) is symmetric and periodic. Furthermore, the FHR persists under phase-averaging as it is composed exclusively of harmonics that are T_1-periodic. The anti-symmetric class contains no deterministic component and is thus purely fluctuating, implying $\mathbf{q}^A = \mathbf{q}^a$.

2.2.2 Spectral Proper Orthogonal Decomposition (SPOD)

SPOD identifies frequency-specific, time-periodic coherent structures $\psi(\boldsymbol{x}, f)$ in statistically stationary flows (Lumley, 1970; Towne et al., 2018; Schmidt and Colonius, 2020). Here, the space-time correlation tensor $\boldsymbol{C}(\boldsymbol{x},\boldsymbol{x}',\tau)$ (where $\tau = t - t'$) is Fourier-transformed to the cross-spectral density (CSD) tensor $\boldsymbol{S}(\boldsymbol{x},\boldsymbol{x}',f) = \int_{-\infty}^{\infty} \boldsymbol{C}(\boldsymbol{x},\boldsymbol{x}',\tau) e^{-2\pi i f \tau} d\tau$ to solve the respective continuous and discrete eigenvalue problems

$$\int_V \boldsymbol{S}(\boldsymbol{x},\boldsymbol{x}',f)\boldsymbol{W}(\boldsymbol{x}')\psi(\boldsymbol{x}',f)\,d\boldsymbol{x}' = \lambda(f)\psi(\boldsymbol{x},f), \tag{2.3}$$

$$1/N_b\, \hat{\mathbf{Q}}_k \hat{\mathbf{Q}}_k^* \mathbf{W} \boldsymbol{\Psi}_k = \boldsymbol{\Psi}_k \boldsymbol{\Lambda}_k, \tag{2.4}$$

where $\hat{\mathbf{Q}}_k$ stores different realizations of the Fourier modes $\hat{\mathbf{q}}_k(\mathbf{x})$ at frequency f_k and the CSD is estimated as $\mathbf{S}_k = E_b\{\hat{\mathbf{q}}_k(\mathbf{x})\hat{\mathbf{q}}_k^*(\mathbf{x})\}$ with block-wise expectation $E_b\{\cdot\}$ (Welch, 1967b). The columns of $\boldsymbol{\Psi}_k$ are discrete SPOD modes $\psi_k^{(m)}(\mathbf{x})$ and $\boldsymbol{\Lambda}_k = \mathrm{diag}(\lambda_k)$ stores their energies $\lambda_k^{(m)}$. Expansion coefficients are recovered in the rows of $\mathbf{A}_k = \boldsymbol{\Psi}_k^* \mathbf{W} \hat{\mathbf{Q}}_k$, with $\mathbf{A}_k^* \mathbf{A}_k = \boldsymbol{\Lambda}_k$. SPOD modes are single-frequency oscillatory coherent structures that optimally capture the variance of the data at that frequency and are orthonormal in the space- and infinite-time norm $\langle \cdot, \cdot \rangle_{\boldsymbol{x},t}$. They are thus statistically optimal linear combinations of Fourier modes.

2.2.3 Space-Time Proper Orthogonal Decomposition (STPOD)

STPOD extracts space-time-energy-optimal spatio-temporal modes $\phi(\boldsymbol{x},t)$ over a finite time window ΔT, chosen here as one actuation period T_1. The modes solve the respective

continuous and discrete eigenvalue problems (Lumley, 1970; Schmidt and Schmid, 2019)

$$\int_{\Delta T}\int_{V} \boldsymbol{C}(\boldsymbol{x},\boldsymbol{x}',t,t')\boldsymbol{W}(\boldsymbol{x}')\phi(\boldsymbol{x}',t')\,d\boldsymbol{x}'\,dt' = \lambda\,\phi(\boldsymbol{x},t), \tag{2.5}$$

$$1/N_j\,\mathbf{Q}\mathbf{Q}^*\mathbf{W}\boldsymbol{\Phi} = \boldsymbol{\Phi}\boldsymbol{\Lambda}, \tag{2.6}$$

over a spatial domain V, with positive-definite weight matrix $\boldsymbol{W}(\boldsymbol{x})$ and statistically estimated two-point space-time correlation tensor $\boldsymbol{C}(\boldsymbol{x},\boldsymbol{x}',t,t') = E\{\mathbf{q}(\boldsymbol{x},t)\mathbf{q}^*(\boldsymbol{x}',t')\}$. The modes $\phi(\boldsymbol{x},t)$ are orthonormal in the space- and finite-time norm $\langle\cdot,\cdot\rangle_{\boldsymbol{x},\Delta T}$. For the discrete problem, snapshots of $\mathbf{q}(\mathbf{x},t)$ are stacked column-wise over ΔT for each realization j, and different realizations are concatenated row-wise to form the data matrix $\mathbf{Q}$, which is then decomposed by (2.6). The discrete STPOD modes $\phi_m(\mathbf{x},t)$ form the columns of $\boldsymbol{\Phi}$ and $\boldsymbol{\Lambda} = \mathrm{diag}(\lambda)$ stores their energies λ_m. Realization-varying expansion coefficients $a_{m,j}$ are obtained as the rows of $\mathbf{A} = \boldsymbol{\Phi}^*\mathbf{W}\mathbf{Q}$, with $\mathbf{A}^*\mathbf{A} = \boldsymbol{\Lambda}$. Notably, STPOD specializes to space-only POD in the limit $\Delta T \to 0$ and, assuming statistical stationarity, converges to SPOD in the limit $\Delta T \to \infty$ (Frame and Towne, 2023). Here, STPOD is the most unbiased method with no assumptions about the dynamics of the space-time signal $\mathbf{q}(\mathbf{x},t)$. Unlike spectral approaches that impose periodicity by default, it produces periodic modes only when they are energetically dominant within a given window $\Delta T = T_1$ —a crucial property for symmetry breaking analysis.

2.3 Extracting the Resonant Fundamental Harmonic Response (FHR)

As we are actuating the eigenmode (TS wave) of a system with quadratic nonlinearities, a resonant response with harmonics must be expected. To extract those harmonic coherent structures, we apply SPOD to the symmetric ($\mathbf{q}^S$) and anti-symmetric ($\mathbf{q}^A$) components individually, yielding energy-optimal modes at each frequency in each symmetry class. Figure 2.2(a,b) contrasts the $\mathbf{q}^S$ and $\mathbf{q}^A$ spectra: The $\mathbf{q}^S$ spectrum is dominated by low-rank peaks at the TS frequency ($f_k/f_1 = 1$) and its harmonics, characteristic of dominant coherent structures, while

the noise-like $\mathbf{q}^A$ spectrum is broadband with slow rank decay, showing no energetically preferred modes. Thus, the FHR is symmetric, time-periodic, and represents the expected deterministic result from symmetric, periodic actuation of the Navier-Stokes equations, as predicted by classical frameworks like harmonic balance (Rigas et al., 2021). The FHR can be assembled by a linear combination of the first symmetric SPOD modes $\psi_k^{(1)}$ of the harmonic peaks $f_k = f_n$ ($n \in \mathbb{Z}$) in figure 2.2(a):

$$\tilde{\mathbf{q}}(\mathbf{x},t) \equiv \sum_n \psi_n^{(1)} a_n^{(1)} e^{(i2\pi f_n t)} + \bar{\mathbf{q}}(\mathbf{x}) = \tilde{\mathbf{q}}_{\setminus 0}(\mathbf{x},t) + \bar{\mathbf{q}}(\mathbf{x}), \tag{2.7}$$

with the time-averaged mean flow $\bar{\mathbf{q}}(\mathbf{x})$, and the block-wise estimated dominant SPOD expansion coefficients $a_n^{(1)}$. We compute the SPOD using $N_{\mathrm{FFT}} = 512$, eight periods per block and 50% block overlap. Most notably, figure 2.2(c) shows that $\tilde{\mathbf{q}}(\mathbf{x},t)$ exhibits compact spatial support when fully assembled, and, while the resulting vortical structures closely resemble hairpin "packets" or "forests" in their late stages (often characterized as "chaotic" in the turbulence literature (Adrian, 2007; Wu and Moin, 2009)), we show that such seemingly disordered structures in fact arise *deterministically* here as the system's resonant FHR to periodic actuation of its eigenmode.

As illustrated in figure 2.1 and § 2.2.1, subtracting the deterministic FHR from the full data yields a turbulent, cyclo-stationary fluctuation $\mathbf{q}'' \equiv \mathbf{q} - \tilde{\mathbf{q}}$. Further splitting this fluctuation into symmetry classes, $\mathbf{q}'' = \mathbf{q}^s + \mathbf{q}^a$, isolates the data components of temporal and spatial symmetry breaking by construction: As $\tilde{\mathbf{q}}$ is symmetric and periodic, $\mathbf{q}^s$ must contain all non-periodic symmetric fluctuations that break time symmetry, while any indication of $\mathbf{q}^a$ captures the onset of spanwise asymmetry. This results in a pivotal multiscale separation: We later show in figure 2.4(c) that the rapid surge of $\mathbf{q}^s$ and $\mathbf{q}^a$ occurs with a simultaneous decline in the $\tilde{\mathbf{q}}$ amplitude, allowing us to locate exactly where symmetry breaking arises.

We next adopt a local perspective to gain a better overview of the streamwise evolution of these components. To this end, figure 2.3 plots local integral-y^*-z^*-plane power spectral densities for each streamwise station, colored by the *local* SPOD energy ratio $\lambda^{(1)}(x)/\sum_i \lambda^{(i)}(x)$ to quantify the mode dominance: High values (blue) denote energy focused in one leading mode, while low

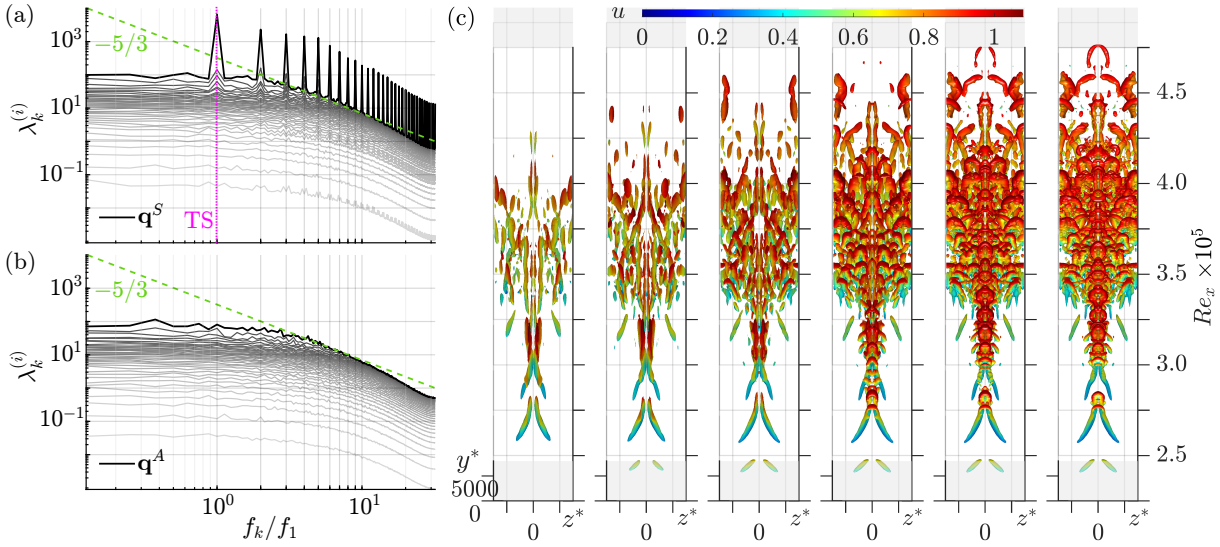


Figure 2.2. SPOD energy spectra for (a) $\mathbf{q}^S$ symmetric and (b) $\mathbf{q}^A$ anti-sym. components; compare to Sayadi et al. (2013). (c) Superposition of N_n={1, 2, 4, 8, 16, 32} dominant SPOD modes $\psi_n^{(1)}$ at harmonic peaks f_n (2.7); Q-criterion ($Q = 10^3$) colored by u.

values (red) reflect energy spread across many modes. This spatially resolved analysis reveals the statistics and dynamics that dominate at each location and frequency, guiding a subsequent search for coherent structures. The fundamental spectral evolution starts with the TS wave, marked in figure 2.3(a), whose energy level we use as reference for other components (above TS: significant / below TS: weak). Its FHR $\tilde{\mathbf{q}}$ manifests as dominant peaks that grow with increasing Re_x, while non-harmonic components remain negligible in the weak background spectrum. The initial flow is thus deterministic. As the flow gains energy towards $C_f^{\max}$ (at $Re_x \approx 4 \times 10^5$), the non-harmonic spectrum gains amplitude with decreasing mode dominance, indicating increasing stochasticity, while the harmonic peaks lose both amplitude and their initial mode dominance. Since the flow is cyclo-stationary and all its energy is initially confined to $\tilde{\mathbf{q}}$ (see figure 2.4c), the emergence of broadband content reflects energy transfer from the harmonics to $\mathbf{q}^s$, marking the transition from periodic to time-symmetry-broken states. Beyond $C_f^{\max}$, the spectrum converges towards a fully broadband, low modal dominance state, indicating statistical stationarity and turbulence.

Remarkably, figure 2.3(b) shows that even after removing the deterministic FHR $\tilde{\mathbf{q}}$, the $\mathbf{q}^s$

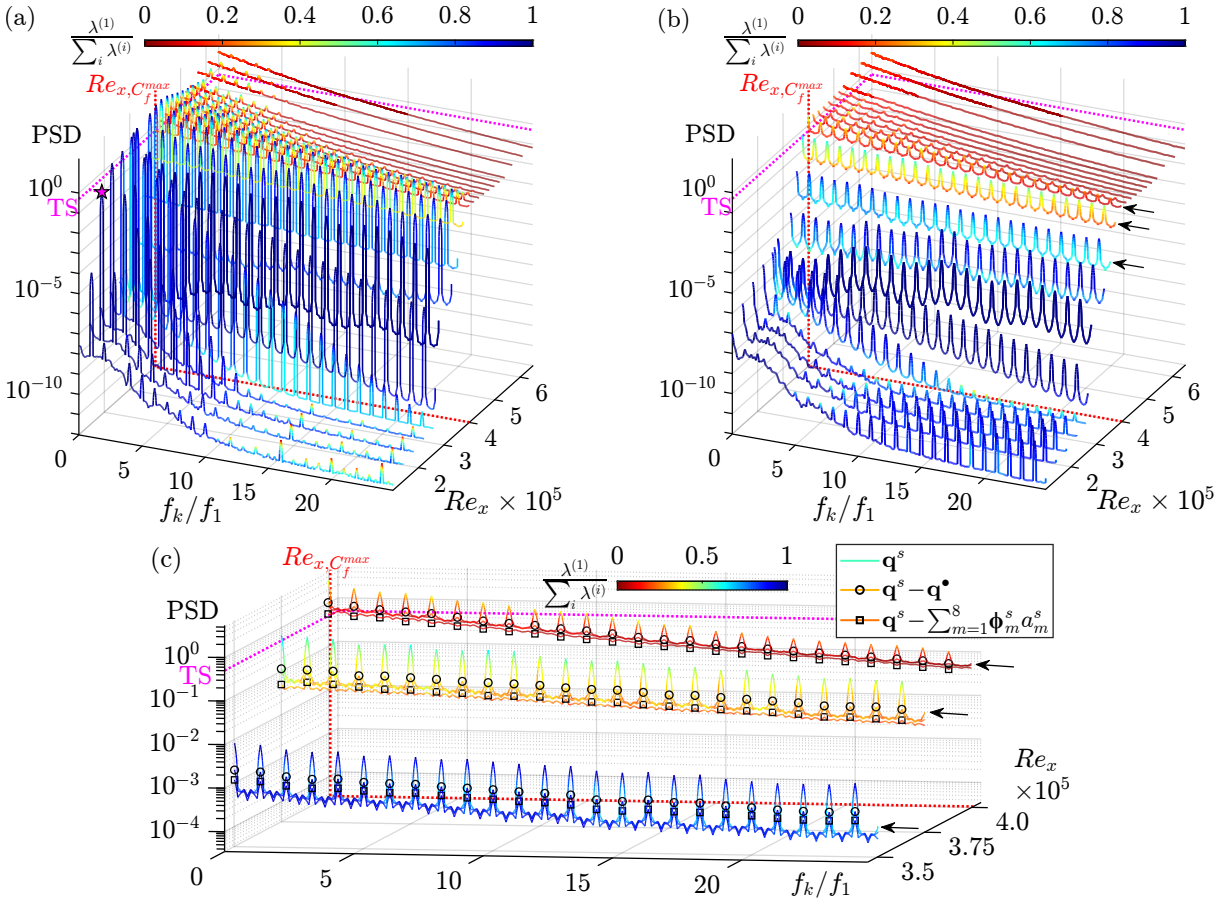


Figure 2.3. Local power spectral densities of different quantities as a streamwise function of Re_x, colored by the ratio of the dominant local SPOD energy over the full local energy $\lambda^{(1)}(x)/\sum_i \lambda^{(i)}(x)$. (a) $\mathbf{q}^S$ full symmetric data. (b) $\mathbf{q}^s$ symmetric fluctuation. (c) Zoom on amplified region, progressive ablation of STPOD modes from $\mathbf{q}^s$: first two modes (i.e. $\mathbf{q}^\bullet$; resulting in $\mathbf{q}^s - \mathbf{q}^\bullet = \mathbf{q}^\circ$ sym. residual) vs. eight modes subtracted.

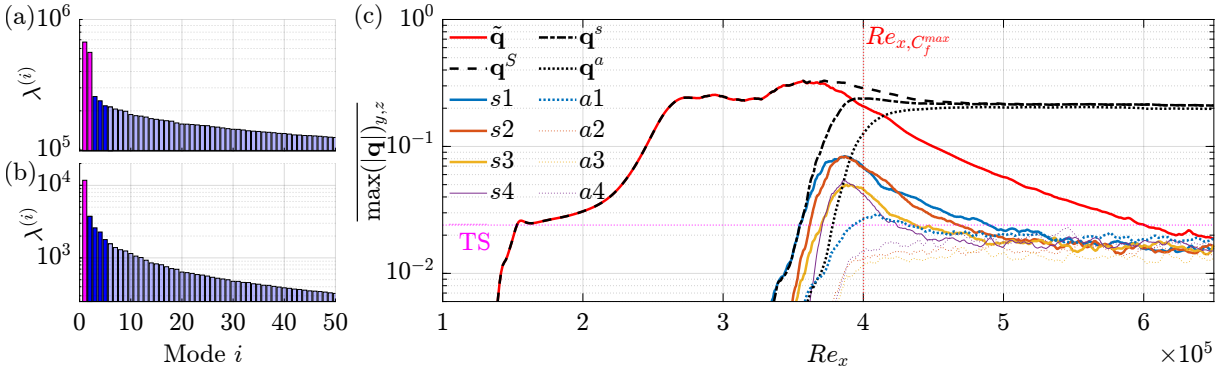


Figure 2.4. (a) $\mathbf{q}^s$ symmetric and (b) $\mathbf{q}^a$ anti-symmetric STPOD modal energy spectra; dominant modes with periodic dynamics colored magenta. (c) Streamwise amplitude development of select STPOD modes $\phi_m^{s/a}(\mathbf{x},\tau)a_{m,j}^{s/a}$, enveloped by the total $\mathbf{q}^S$, $\mathbf{q}^s$ and $\mathbf{q}^a$ components. The TS wave input amplitude level serves as significance threshold.

fluctuation spectrum still exhibits prominent harmonic peaks with high modal dominance. This crucial finding indicates that fluctuations remain largely phase-locked to the harmonics initially and can also be represented by few dominant modes at these frequencies, thereby motivating a targeted search for coherent structures that dominate symmetry breaking.

2.4 The Dynamics and Statistics of Temporal & Spatial Symmetry Breaking

We apply STPOD to the $\mathbf{q}^s$ and $\mathbf{q}^a$ fluctuations using the method outlined in § 2.2.3 to identify dominant symmetry breaking modes with minimal assumptions. As we center the data around the FHR $\tilde{\mathbf{q}}$ (which would otherwise be obtained as the first mode if not subtracted), $\tilde{\mathbf{q}}$ can be interpreted as the fundamental space-time mode, leading to the full decomposition

$$\mathbf{q}(\mathbf{x},t) = \mathbf{q}^s(\mathbf{x},t) + \mathbf{q}^a(\mathbf{x},t) + \tilde{\mathbf{q}}(\mathbf{x},t) = \sum_m \left(\phi_m^s(\mathbf{x},\tau)a_{m,j}^s + \phi_m^a(\mathbf{x},\tau)a_{m,j}^a\right) + \tilde{\mathbf{q}}(\mathbf{x},t), \qquad (2.8)$$

where $a_{m,j}^{s/a}$ with $j \in [1, N_{T_1}]$ are realization-dependent expansion coefficients describing amplitude modulations of mode $\phi_m^{s/a}$ across different flow realizations (periods) j. To further resolve the time dynamics of these space-time modes, we propose a modal multi-timescale approach via a

nested space-only POD, separating spatial and temporal information:

$$\begin{aligned}\phi_m(\mathbf{x},\tau) &= \mathbf{U}_m(\mathbf{x})\mathbf{a}_m^{\mathrm{POD}}(\tau)\\ \mathbf{q}(\mathbf{x},t) &= \sum_m \mathbf{U}_m(\mathbf{x})\mathbf{a}_m^{\mathrm{POD}}(\tau)a_{m,j} + \mathbf{U}_0(\mathbf{x})\mathbf{a}_0^{\mathrm{POD}}(t),\end{aligned} \tag{2.9}$$

with space-only POD modes $\mathbf{U}_m(\mathbf{x})$ and local POD expansion coefficients $\mathbf{a}_m^{\mathrm{POD}}(\tau)$. We choose POD for its L_2-optimality and objectivity about time dynamics, unlike DMD or Fourier methods, which assume linear or periodic dynamics. This decomposition now allows for a clear separation of timescales: the fast local dynamics $\mathbf{a}_m^{\mathrm{POD}}(\tau)$ within a realization ($\tau \in [0, T_1]$) and slow global modulation $a_{m,j}$ across realizations, where the instantaneous time becomes $t = \tau + (j-1)T_1$. Furthermore, this enables a dynamical systems analysis by resolving mode trajectory shapes in phase space with $\mathbf{a}_m^{\mathrm{POD}}(\tau)$ (Cvitanović and Gibson, 2010). For visualization, plotting the dominant three coefficients of the $\mathbf{a}_m^{\mathrm{POD}}(\tau)$ vector typically suffices, as higher coefficients generally remain periodic even when dominant ones are not.

2.4.1 Onset of Quasi-Periodicity and Aperiodicity

Figure 2.4 plots the energy spectra and streamwise amplitude development of the STPOD modes. Up to $Re_x \lesssim 3.5 \times 10^5$, the flow is governed entirely by the deterministic, spatially compact mode (FHR) of the early transition. Figure 2.4(c) shows that, as $\tilde{\mathbf{q}}$ falls below the total amplitude, new dominant symmetric STPOD modes ϕ_1^s and ϕ_2^s surge above the TS wave level around $Re_x \approx 3.5 \times 10^5$. They too are vortical and compact, seen in figure 2.5(b), and mark the onset of variance from the purely periodic $\tilde{\mathbf{q}}$. The phase space analysis in figure 2.5(a,c) reveals that these modes, remarkably, also exhibit T_1-periodic dynamics:

$$\phi_m^s(\mathbf{x}, \tau \to T_1) \begin{cases} = \phi_m^s(\mathbf{x}, \tau \to 0), & m = \{1,2\} \\ \neq \phi_m^s(\mathbf{x}, \tau \to 0), & m \geq 3. \end{cases} \tag{2.10}$$

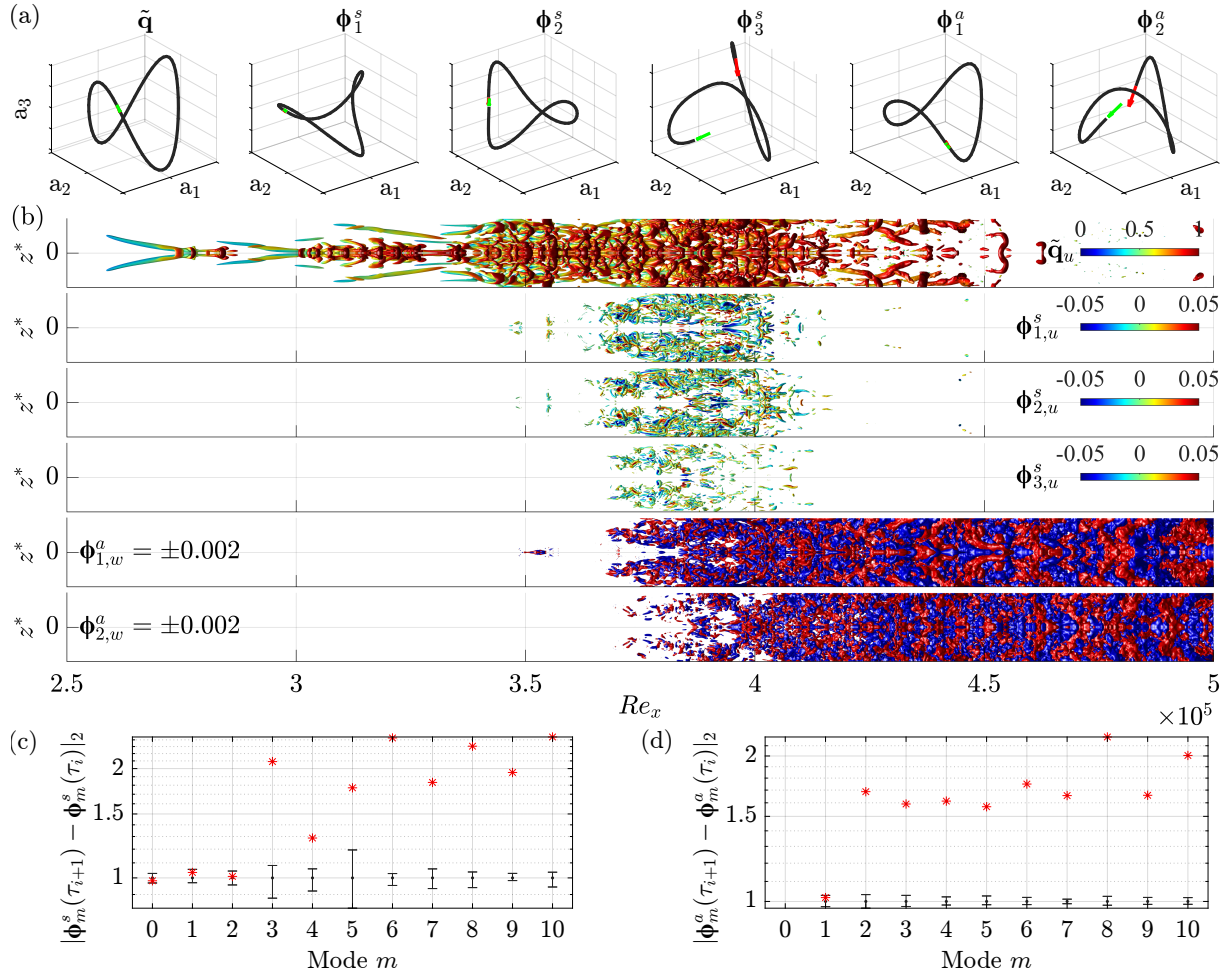


Figure 2.5. Symmetry breaking modes from STPOD. Deterministic mode $\tilde{\mathbf{q}}$ (FHR), first three symmetric modes (ϕ^s_{1-3}) and first two anti-sym. modes (ϕ^a_{1-2}). (a) $\mathbf{a}^{\text{POD}}_m(\tau)$ trajectory phase-spaces and (b) instantaneous isosurfaces at same phase. Symmetric modes shown by Q-criterion ($Q = 10^3$) colored by u-velocity; anti-sym. modes shown by w-velocity ($w = \pm 0.002$). (c) Symmetric and (d) anti-sym. mode relative L_2-norm distances between consecutive phases: Red markers denote distance from last to first phase (periodicity mismatch), error bars show the existing min/max consecutive phase distances within the period, normalized by the average phase distance in a given mode. See movie 2.

The critical distinction lies in their non-constant expansion coefficients $a^s_{1,j}$ and $a^s_{2,j}$ that vary over long timescales. This creates a region of *geometrically quasi-periodic* dynamics where the state is modulated by different periodic trajectories, i.e. for $3.4 \times 10^5 \lesssim Re_x \lesssim 3.7 \times 10^5$,

$$\mathbf{q}(\mathbf{x},t) \approx \tilde{\mathbf{q}}(\mathbf{x},t) + \mathbf{q}^{\bullet}(\mathbf{x},t) = \tilde{\mathbf{q}}(\mathbf{x},t) + a^s_{1,j}\phi^s_1(\mathbf{x},\tau) + a^s_{2,j}\phi^s_2(\mathbf{x},\tau). \tag{2.11}$$

These trajectories are statistically periodic but instantaneously depart from the deterministic state $\tilde{\mathbf{q}}$ in shapes and directions given by ϕ^s_1 and ϕ^s_2, with *amplitudes* and *timings* governed explicitly by expansion coefficients $a^s_{1,j}$ and $a^s_{2,j}$ that vary slowly over the periods j. This quasi-periodic dynamic is a categorical departure from the previous deterministic behavior, as the system now explores multiple periodic trajectories in a structured manner.

The onset of chaos begins with the emergence of ϕ^s_3 around $Re_x \gtrsim 3.7 \times 10^5$. This mode breaks the pattern of local periodicity, exhibiting a clear jump between its first and last phase (figure 2.5a,c). All higher modes ($m \geq 3$) are also aperiodic and located increasingly further downstream. This creates the spectral redistribution from harmonic to broadband frequencies, shown in figure 2.3(c): A zoom into the region of critical fluctuation growth reveals the spectral contents of the modes. Removing the periodic modes ϕ^s_1 and ϕ^s_2 eliminates precisely the mode-dominant harmonic peaks, while removing higher modes flattens the spectrum across all frequencies toward fully broadband characteristics. Since modes that are not T_1-periodic can, by definition, *not* be captured solely within the harmonic frequencies, they *must* fill the broadband spectrum between peaks, and are thus indicative of chaos and turbulence.

The progression from periodic to chaotic dynamics seen here echoes the dynamical systems view of wall turbulence (Cvitanović and Gibson, 2010; Viswanath, 2007; Kawahara and Kida, 2001), where trajectories recurrently visit the available unstable periodic orbits that "scaffold" the state space. Our hierarchical breakdown—from a single periodic base state ($\tilde{\mathbf{q}}$), through quasi-periodic modulations (ϕ^s_1, ϕ^s_2), to chaotic excursions via non-periodic modes (ϕ^s_3 and higher)—offers a data-driven perspective on this mechanism.

2.4.2 Onset of Spanwise Asymmetry

Spatial symmetry breaking follows a remarkably similar route. The anti-symmetric compo-nent $\mathbf{q}^A = \mathbf{q}^a$ remains energetically negligible until $Re_x \lesssim 3.8 \times 10^5$ (figure 2.4c), from where it rapidly amplifies toward the amplitude of $\mathbf{q}^S$. To isolate the modes that initiate asymmetry onset, we compute the STPOD for $\mathbf{q}^a$ with a spatial weight focused on the amplified region of interest ($Re_x \leq 4.0 \times 10^5$) prior to the onset of saturated downstream turbulence. Most notably, the first anti-symmetric mode ϕ_1^a also exhibits local periodicity (figure 2.5a,d)

$$\phi_m^a(\mathbf{x}, \tau \to T_1) \begin{cases} = \phi_m^a(\mathbf{x}, \tau \to 0), & m = 1 \\ \neq \phi_m^a(\mathbf{x}, \tau \to 0), & m \geq 2 \end{cases} \tag{2.12}$$

despite a total absence of anti-symmetric forcing or mean flow. Similar to equation (2.11), ϕ_1^a forms quasi-periodic asymmetric variations with $\tilde{\mathbf{q}}$, while spectral analysis analogous to figure 2.3(b,c) (omitted for brevity) confirms that higher modes again become broadband. Thus, a central finding here is that both spatial and temporal symmetry breaking emerge through coherent space-time structures in distinct dynamical hierarchies, not as random fluctuations.

2.5 Inter-Modal/Inter-Symmetry Energy Transfer

We introduce the symmetry-decomposed Navier-Stokes equations (NSE). By inserting the decomposition (2.2) into the incompressible NSE, followed by reflection about the symmetry plane and subsequent addition or subtraction of the reflection, we obtain, respectively,

$$\text{(Symmetric NSE)} \quad \partial_t u_i^S + u_j^S \partial_{x_j} u_i^S + u_j^A \partial_{x_j} u_i^A = -\partial_{x_i} p^S + \nu \partial_{x_j x_j} u_i^S, \quad \partial_{x_i} u_i^S = 0, \tag{2.13}$$

$$\text{(Anti-sym. NSE)} \quad \partial_t u_i^A + u_j^S \partial_{x_j} u_i^A + u_j^A \partial_{x_j} u_i^S = -\partial_{x_i} p^A + \nu \partial_{x_j x_j} u_i^A, \quad \partial_{x_i} u_i^A = 0. \tag{2.14}$$

As the cyclo-stationary anti-symmetric component is purely fluctuating ($u_i^A = u_i^a$), its energy budget follows from dotting (2.14) with u_i^a and phase-averaging $\widetilde{(\cdot)}$, yielding the equation

$$\underbrace{\partial_t \widetilde{k^a} + \widetilde{u}_j \partial_{x_j} \widetilde{k^a}}_{\widetilde{\mathscr{D}}_t \widetilde{k^a}} = \underbrace{-\widetilde{u_j^s \partial_{x_j} k^a}}_{\mathscr{T}^{a\leftarrow s}} \underbrace{-\widetilde{u_i^a u_j^a} \partial_{x_j} \widetilde{u}_i - \widetilde{u_i^a u_j^a \partial_{x_j} u_i^s}}_{\mathscr{P}^{\star\to a} + \mathscr{P}^{s\to a}} \underbrace{-\partial_{x_i} \widetilde{u_i^a p^a}}_{\Pi^a} + \underbrace{\nu \partial_{x_j x_j} \widetilde{k^a}}_{D^a} \underbrace{-\nu \widetilde{\partial_{x_j} u_i^a \partial_{x_j} u_i^a}}_{\varepsilon^a} \tag{2.15}$$

in which the production pathway is shear extraction from the symmetric field consisting of FHR ($\mathscr{P}^{\star\to a}$) and turbulent ($\mathscr{P}^{s\to a}$) production for a phase-averaged TKE $\widetilde{k^a} \equiv \widetilde{u_i^a u_i^a}/2$. For the symmetric NSE, we insert the cyclo-stationary decomposition $u_i^S = \widetilde{u}_i + u_i^s$ and take dot products with $\widetilde{u}_i$ and u_i^s each, followed by phase-averaging, to derive TKE budgets $k^\star \equiv \widetilde{u}_i \widetilde{u}_i/2$ and $\widetilde{k^s} \equiv \widetilde{u_i^s u_i^s}/2$ for the FHR and the symmetric fluctuations, respectively,

$$\widetilde{\mathscr{D}}_t k^\star = \underbrace{(\widetilde{u_i^s u_j^s} + \widetilde{u_i^a u_j^a}) \partial_{x_j} \widetilde{u}_i}_{-\mathscr{P}^{\star\to s} - \mathscr{P}^{\star\to a}} \underbrace{-\partial_{x_j}\big(\widetilde{u}_i (\widetilde{u_i^s u_j^s} + \widetilde{u_i^a u_j^a})\big)}_{\mathscr{T}^{\star\leftarrow s} + \mathscr{T}^{\star\leftarrow a}} \underbrace{-\partial_{x_i}(\widetilde{u}_i \widetilde{p})}_{\Pi^\star} + D^\star - \varepsilon^\star, \tag{2.16}$$

$$\widetilde{\mathscr{D}}_t \widetilde{k^s} = \underbrace{-\widetilde{u_j^s \partial_{x_j} k^s}}_{\mathscr{T}^{s\leftarrow s}} \underbrace{-\widetilde{u_i^s u_j^s}\, \partial_{x_j} \widetilde{u}_i}_{\mathscr{P}^{\star\to s}} \underbrace{-\partial_{x_j}(\widetilde{u_i^s u_i^a u_j^a})}_{\mathscr{T}^{s\leftarrow a}} \underbrace{+\widetilde{u_i^a u_j^a \partial_{x_j} u_i^s}}_{-\mathscr{P}^{s\to a}} \underbrace{-\partial_{x_i} \widetilde{u_i^s p^s}}_{\Pi^s} + D^s - \varepsilon^s. \tag{2.17}$$

The three budgets are linked by pairs of equal-and-opposite production terms, which create directed energy transfers via harmonic ($\mathscr{P}^{\star\to s}$, $\mathscr{P}^{\star\to a}$) or inter-symmetry ($\mathscr{P}^{s\to a}$) pathways. Similarly, we derive an inter-modal energy transfer between the leading modes of each symmetry class and their residual turbulent fluctuations. The symmetric fluctuation is split into $u_i^s = u_i^\bullet + u_i^\circ$. With the respective dot products and phase-averaging, the TKE budget of the leading quasi-periodic symmetric modes (i.e., $\mathbf{q}^\bullet = a_1^s \phi_1^s + a_2^s \phi_2^s$) is derived as

$$\begin{aligned} \widetilde{\mathscr{D}}_t \widetilde{k^\bullet} = \mathscr{T}^{\bullet\leftarrow s} + \Pi^\bullet + D^\bullet - \varepsilon^\bullet + \overbrace{-\widetilde{u_i^\bullet u_j^s} \partial_{x_j} \widetilde{u}_i}^{\mathscr{P}^{\star\to\bullet}} + \overbrace{-\widetilde{u_i^\bullet \partial_{x_j}(u_i^a u_j^a)}}^{(\mathscr{T}^{\bullet\leftarrow a} - \mathscr{P}^{\bullet\to a})} \\ \underbrace{-\widetilde{u_i^\bullet \partial_t u_i^\circ} - \widetilde{u_i^\bullet u_j^S \partial_{x_j} u_i^\circ} - \widetilde{u_i^\bullet \partial_{x_i} p^\circ} + \nu \widetilde{u_i^\bullet \partial_{x_j x_j} u_i^\circ}}_{\mathscr{S}^{\circ\to\bullet}} \end{aligned} \tag{2.18}$$

and the TKE budget for the symmetric residual fluctuation is given by a conjugate equation

$$\begin{aligned}\widetilde{\mathscr{D}}_t\widetilde{k^{\circ}} = \mathscr{T}^{\circ\leftarrow s}+\Pi^{\circ}+D^{\circ}-\varepsilon^{\circ}+\overbrace{-\widetilde{u_i^{\circ}u_j^{s}}\partial_{x_j}\widetilde{u}_i}^{\mathscr{P}^{\star\to\circ}}+\overbrace{-\widetilde{u_i^{\circ}\partial_{x_j}(u_i^a u_j^a)}}^{(\mathscr{T}^{\circ\leftarrow a}-\mathscr{P}^{\circ\to a})}\\ \underbrace{-\widetilde{u_i^{\circ}\partial_t u_i^{\bullet}}-\widetilde{u_i^{\circ}u_j^{S}\partial_{x_j}u_i^{\bullet}}-\widetilde{u_i^{\circ}\partial_{x_i}p^{\bullet}}+\nu\widetilde{u_i^{\circ}\partial_{x_jx_j}u_i^{\bullet}}}_{\mathscr{S}^{\bullet\to\circ}}.\end{aligned} \tag{2.19}$$

We note that the sum of (2.18) and (2.19) exactly recovers the total symmetric TKE budget (2.17). Both feature conjugate source terms, $\mathscr{S}^{\circ\to\bullet}$ and $\mathscr{S}^{\bullet\to\circ}$, that couple the energy flow between the leading modes and residual fluctuations, as well as standard production terms by the FHR ($\mathscr{P}^{\star\to\bullet/\circ}$) and, notably, interaction terms with the anti-symmetric fluctuation ($\mathscr{T}^{\bullet/\circ\leftarrow a}-\mathscr{P}^{\bullet/\circ\to a}$). Thus, we apply the split $u_i^a = u_i^{\blacktriangle}+u_i^{\triangle}$ to likewise derive the TKE budget of the leading quasi-periodic anti-symmetric mode $m=1$ (i.e. $\mathbf{q}^{\blacktriangle}=a_1^a\phi_1^a$) as

$$\begin{aligned}\widetilde{\mathscr{D}}_t\widetilde{k^{\blacktriangle}} = \mathscr{T}^{\blacktriangle\leftarrow s}+\Pi^{\blacktriangle}+D^{\blacktriangle}-\varepsilon^{\blacktriangle}+\overbrace{-\widetilde{u_i^{\blacktriangle}u_j^{a}}\partial_{x_j}\widetilde{u}_i-\widetilde{u_i^{\blacktriangle}u_j^{a}\partial_{x_j}u_i^{s}}}^{\mathscr{P}^{\star\to\blacktriangle}+\mathscr{P}^{s\to\blacktriangle}}\\ \underbrace{-\widetilde{u_i^{\blacktriangle}\partial_t u_i^{\triangle}}-\widetilde{u_i^{\blacktriangle}u_j^{S}\partial_{x_j}u_i^{\triangle}}-\widetilde{u_i^{\blacktriangle}\partial_{x_i}p^{\triangle}}+\nu\widetilde{u_i^{\blacktriangle}\partial_{x_jx_j}u_i^{\triangle}}}_{\mathscr{S}^{\triangle\to\blacktriangle}}\end{aligned} \tag{2.20}$$

and the respective conjugate TKE budget for the anti-symmetric residual fluctuation as

$$\begin{aligned}\widetilde{\mathscr{D}}_t\widetilde{k^{\triangle}} = \mathscr{T}^{\triangle\leftarrow s}+\Pi^{\triangle}+D^{\triangle}-\varepsilon^{\triangle}+\overbrace{-\widetilde{u_i^{\triangle}u_j^{a}}\partial_{x_j}\widetilde{u}_i-\widetilde{u_i^{\triangle}u_j^{a}\partial_{x_j}u_i^{s}}}^{\mathscr{P}^{\star\to\triangle}+\mathscr{P}^{s\to\triangle}}\\ \underbrace{-\widetilde{u_i^{\triangle}\partial_t u_i^{\blacktriangle}}-\widetilde{u_i^{\triangle}u_j^{S}\partial_{x_j}u_i^{\blacktriangle}}-\widetilde{u_i^{\triangle}\partial_{x_i}p^{\blacktriangle}}+\nu\widetilde{u_i^{\triangle}\partial_{x_jx_j}u_i^{\blacktriangle}}}_{\mathscr{S}^{\blacktriangle\to\triangle}}.\end{aligned} \tag{2.21}$$

Again, both (2.20) and (2.21) feature conjugate source terms ($\mathscr{S}^{\triangle\to\blacktriangle}$, $\mathscr{S}^{\blacktriangle\to\triangle}$), production terms with FHR and symmetric fluctuations, and recombine to form the total budget (2.15).

Figure 2.6 reveals that in *both* symmetry classes, the production from the FHR to the

Legend: ($\bullet/\circ$) quasi-periodic/residual symmetric; ($\blacktriangle/\triangle$) quasi-periodic/residual anti-symmetric; ($\star$) FHR.

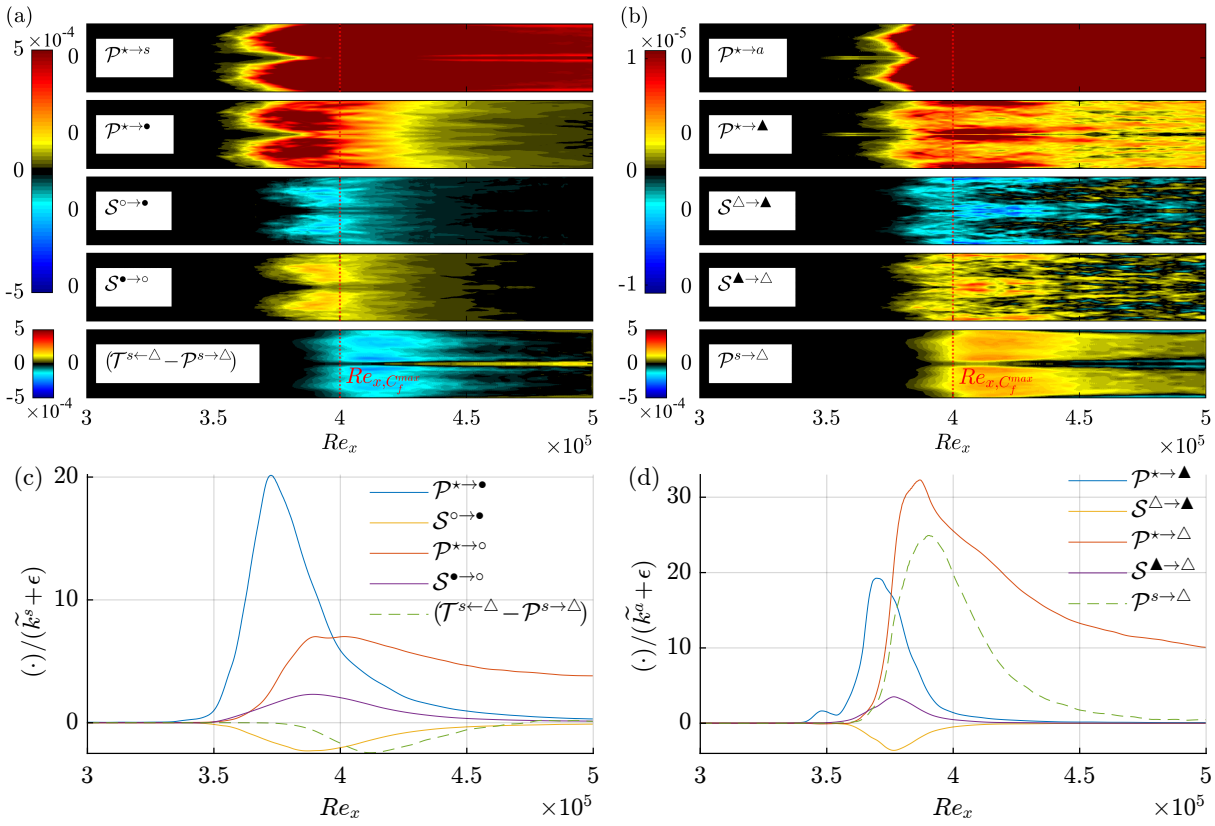


Figure 2.6. Inter-modal/inter-symmetry energy transfer and production terms. (a) symmetric and (b) anti-symmetric terms in integral-y^*, time-averaged view. (c) and (d) integral-y^*-z^*, time-averaged view, normalized by their total TKE (and small ε to avoid division by 0), yielding a TKE-specific efficacy of each pathway relative to the local energy. See movie 3.

leading modes ($\mathscr{P}^{\star\to\bullet/\blacktriangle}$) arises and peaks upstream of their residual production ($\mathscr{P}^{\star\to\circ/\triangle}$). This establishes a distinct streamwise succession: dominant modes are energized first by the FHR, serving as precursor for the subsequent growth of residual fluctuations. The mechanism underlying this transition is the inter-modal transfer, which exhibits an equal-and-opposite source-sink structure, i.e. $\mathscr{S}^{\bullet\to\circ} \approx -\mathscr{S}^{\circ\to\bullet}$ and $\mathscr{S}^{\blacktriangle\to\triangle} \approx -\mathscr{S}^{\triangle\to\blacktriangle}$, visible in both their Re_x-z^* footprints and line plots. Accordingly, we report only the transfer/production terms essential for energetic coupling of the TKE budgets (transport terms $\mathscr{T}$ are numerically negligible). Most notably, the residual production arises only in lockstep with the inter-modal transfer, and not before or independently, implying a handoff mechanism wherein the residual field does not grow until energized by the transfer from the leading modes. This sequenced, directed energy transfer suggests that the leading modes act as energetic gateway, enabling the flow of energy from the deterministic FHR to the broadband turbulent residuals.

In the anti-symmetric case, the residual production $\mathscr{P}^{\star\to\triangle}$, once energized via $\mathscr{S}^{\blacktriangle\to\triangle}$, rapidly exceeds the efficacy of the mode production as it peaks in tandem with the nonlinear inter-symmetry production $\mathscr{P}^{s\to\triangle}$. This term acts as a potent source for the anti-symmetric residual and as sink for the symmetric budget (green dashed lines in figure 2.6c,d), confirming negligible back-coupling (i.e. $(\mathscr{T}^{s\leftarrow\triangle} - \mathscr{P}^{s\to\triangle}) \approx -\mathscr{P}^{s\to\triangle}$). Its rise occurs downstream of the initial mode production $\mathscr{P}^{\star\to\blacktriangle}$ and in tandem with the surging residual production, suggesting a sequenced breakdown: anti-symmetry initially arises via the dominant mode but is subsequently amplified by nonlinear inter-symmetry transfer to produce the anti-symmetric broadband residual. Across all energy pathways, the quantities are spatially coherent in the Re_x-z^*- plane (figure 2.6a,b), demonstrating that symmetry-broken turbulence is energetically driven by space-time coherent modes rather than random noise.

2.6 Concluding Remarks

This work reveals the temporal and spatial symmetry breaking mechanisms in canonical K-type boundary layer transition. Deterministic transition begins with eigen-modal dynamics at a single frequency (TS wave) that evolve into harmonics through quadratic nonlinear interactions. This fundamental harmonic response (FHR) $\tilde{\mathbf{q}}$ is composed entirely of symmetric and periodic coherent structures, is spatially compact and persists far downstream. While $\tilde{\mathbf{q}}$ may resemble turbulence, it remains fully harmonic, clearly defining the extent of the deterministic regime. The ability to pinpoint where deterministic dynamics transition to symmetry breaking provides new clarity in distinguishing organized transition from turbulence onset.

We identify the specific space-time structures that drive this transition. The FHR $\tilde{\mathbf{q}}$ dominates until $Re_x \approx 3.5 \times 10^5$, after which organized symmetry breaking structures emerge. The dominant two symmetric modes (ϕ_1^s, ϕ_2^s) exhibit periodic dynamics with slow amplitude modulation, thereby deviating from the periodic base state in the form of quasi-periodic trajectories and creating variance around the harmonic peaks. With increasing Re_x, higher modes (ϕ_3^s and beyond) break periodicity and fill the broadband spectrum, delineating the transition to chaos and turbulence. Notably, spatial symmetry breaking follows a similar organized pattern: despite no anti-symmetric forcings, the first anti-symmetric mode (ϕ_1^a) exhibits periodic dynamics, while higher modes are aperiodic and broadband. This shows that both types of symmetry breaking unfold *not* as random unstructured fluctuations but through a hierarchy of emergent, energetically dominant space-time structures, challenging traditional views of symmetry breaking being a purely random process.

We derive inter-modal and inter-symmetry energy budgets by decomposing the Navier–Stokes equations into symmetric and anti-symmetric governing equations. These budgets reveal conjugate inter-modal source terms that exhibit a numerically confirmed equal-and-opposite conservation, thereby coupling the quasi-periodic modes and the broadband residual fluctuations with a directed energy transfer from the former to the latter. In both symmetry classes, the leading

modes are energized first by the FHR, while the residual production arises only as the inter-modal transfer becomes active, and not independently, indicating that the leading modes provide the energetic conduit for broadband residual growth. The anti-symmetric residual surge is dominated by a near-one-way inter-symmetry transfer from the symmetric fluctuations, suggesting that once asymmetry is even weakly present, the inevitable non-periodicity becomes a robust route for rapid amplification of broadband asymmetry.

Crucially, these findings allow us to define both the onset and spatial reach of new regimes, offering new criteria for quantifying, predicting, and potentially controlling transition. The resulting hierarchy, from a deterministic periodic state through quasi-periodic modulation to aperiodic broadband dynamics, provides new insight into the structure and dynamics governing canonical laminar-turbulent transition. While the exact onset location, extent or amplitude of the symmetry-breaking components can vary with configuration or disturbance level, the presented methods provide a broadly applicable framework that isolates symmetry components, identifies dominant structures, and quantifies both the location and the energetic mechanism by which deterministic states evolve to broadband turbulence.

Supplementary data. Supplementary animations are available at: movie 1, movie 2, movie 3.

Funding. We gratefully acknowledge the NSF for funding this research under grant CBET 2046311.

Declaration of interests. The authors report no conflict of interest.

Chapter Acknowledgement

Chapter 2, in full, is reproduced from Cong Lin and Oliver T. Schmidt, "Boundary Layer Transition as Succession of Temporal and Spatial Symmetry Breaking," *Journal of Fluid Mechanics*, volume 1033 (2026), R4, doi:10.1017/jfm.2026.11423. The article was published by Cambridge University Press under the Creative Commons Attribution 4.0 International licence

(CC BY 4.0). The dissertation author was the primary investigator and primary author of this work.

Chapter 3

Nature of Symmetry Breaking Seeds in Laminar–Turbulent Transition: Data-driven Stability Analysis

Abstract

We show that symmetry breaking in canonical laminar–turbulent transition begins as a linear instability of the deterministic harmonic regime and supplies the nonlinear feedback needed to close its momentum balance at the C_f maximum. Periodic Tollmien–Schlichting-wave actuation generates a nonlinear, harmonically saturated Fundamental Harmonic Response (FHR) with Λ-vortices and hairpin packets, yet it remains time-periodic, reflection-symmetric and cannot itself become broadband. We derive a stability framework from the symmetry-decomposed Navier–Stokes equations and expose early symmetric and anti-symmetric "seeds" as effectively linear perturbations governed by FHR-linearized dynamics. Galilean tracking and multi-trajectory dynamic mode decomposition identify real, synchronous unstable Floquet modes with near-identical growth rates across symmetry subspaces; the inferred operators predict held-out trajectories and independently extracted STPOD modes, while spatial growth rates and governing-equation residuals cross-validate this identification. The symmetric mode organizes successive hairpin-head disturbances into a near-wall burst, breaking temporal symmetry, whereas the anti-symmetric mode breaks reflection symmetry. Crucially, at finite amplitude, phase-averaged covariances of symmetry-breaking fluctuations supply a residual-stress feedback near

the C_f maximum that closes the FHR balance and *opposes* wall shear, suggesting that it helps suppress the overshoot. Although this feedback is periodic, it depends on the second moment of broadband fluctuations absent from the first-moment FHR: adding harmonics therefore cannot recover it, exposing a fundamental statistical closure problem in harmonic methods. Symmetry breaking is thus not a late artifact of nonlinear breakdown but the mechanism by which the FHR loses stability and the feedback required for transition to turbulence.

Keywords: *boundary layer stability, transition to turbulence, Navier–Stokes equations*

3.1 Introduction

Canonical laminar–turbulent transition requires the flow to leave the temporal and spatial symmetries of its deterministic state. In controlled K-type transition, periodic, spanwise-symmetric Tollmien–Schlichting (TS) wave actuation first produces a fully nonlinear response that remains periodic and symmetric despite containing Λ-vortices, hairpin packets and their downstream development. Controlled experiments and direct numerical simulations (DNS) have traced this reproducible route from resonant wave interactions to vortex formation and flow randomization (Klebanoff et al., 1962; Kachanov and Levchenko, 1984; Fasel et al., 1990; Rist and Fasel, 1995; Bake et al., 2002; Sayadi et al., 2013). Proper orthogonal decomposition has complemented this physical picture by extracting the coherent structures and their dynamics from transitional boundary-layer data (Rempfer and Fasel, 1994b,a), while nonlinear frequency-domain formulations have shown that much of the early transition process can be reproduced through compact sets of interacting harmonics (Rigas et al., 2021; Sleeman et al., 2026). These studies explain how the deterministic structures form and interact, but leave a fundamental question unresolved: why do non-periodic and asymmetric dynamics emerge from the initial symmetric harmonic response in the first place?

The companion study by Lin and Schmidt (2026) separated this deterministic response from the subsequent symmetry-breaking fluctuations. Periodic TS-wave actuation generates a

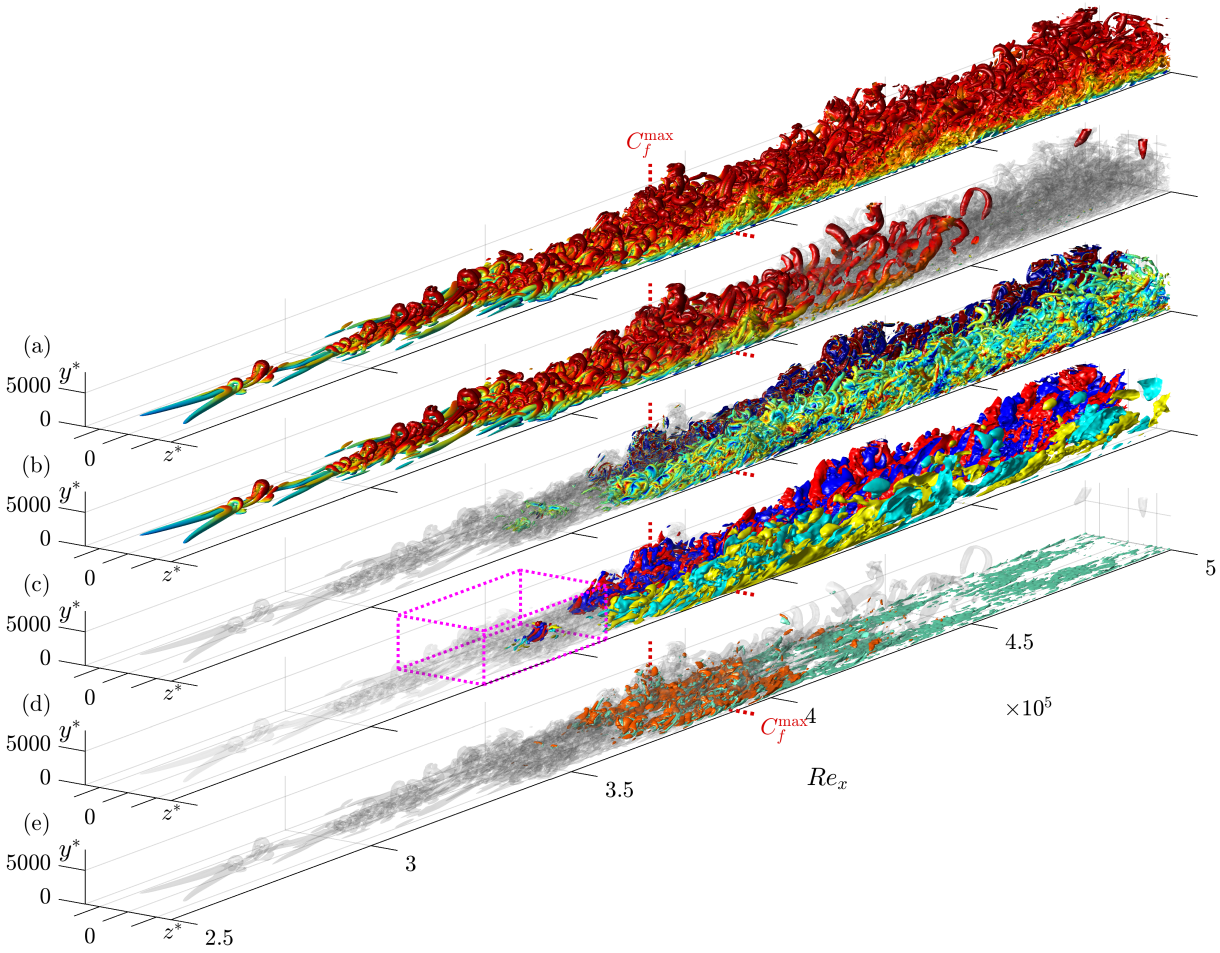


Figure 3.1. Overview of spatio-temporal symmetry decomposition for K-type transition: (a) full DNS field $\boldsymbol{q}$; (b) Fundamental Harmonic Response (FHR) $\tilde{\boldsymbol{q}}$; (c) symmetric and anti-symmetric cyclo-stationary fluctuations, $\boldsymbol{q}^s$ and $\boldsymbol{q}^a$; (d) leading space-time POD modes, $\boldsymbol{\phi}_1^s$ and $\boldsymbol{\phi}_1^a$; and (e) streamwise component of nonlinear symmetry breaking stress feedback $\tilde{\mathscr{R}}^s$, with negative (momentum-inhibiting) and positive (momentum-accelerating) contributions shown in orange and turquoise, respectively. Yellow/cyan depict positive/negative streamwise velocity in the symmetric fields; red/blue depict positive/negative spanwise velocity in the anti-symmetric fields. The magenta box marks the travelling Moore neighbourhood used to construct finite-time Galilean seed trajectories, while the red dotted guides mark the streamwise location of $C_f^{\max}$.

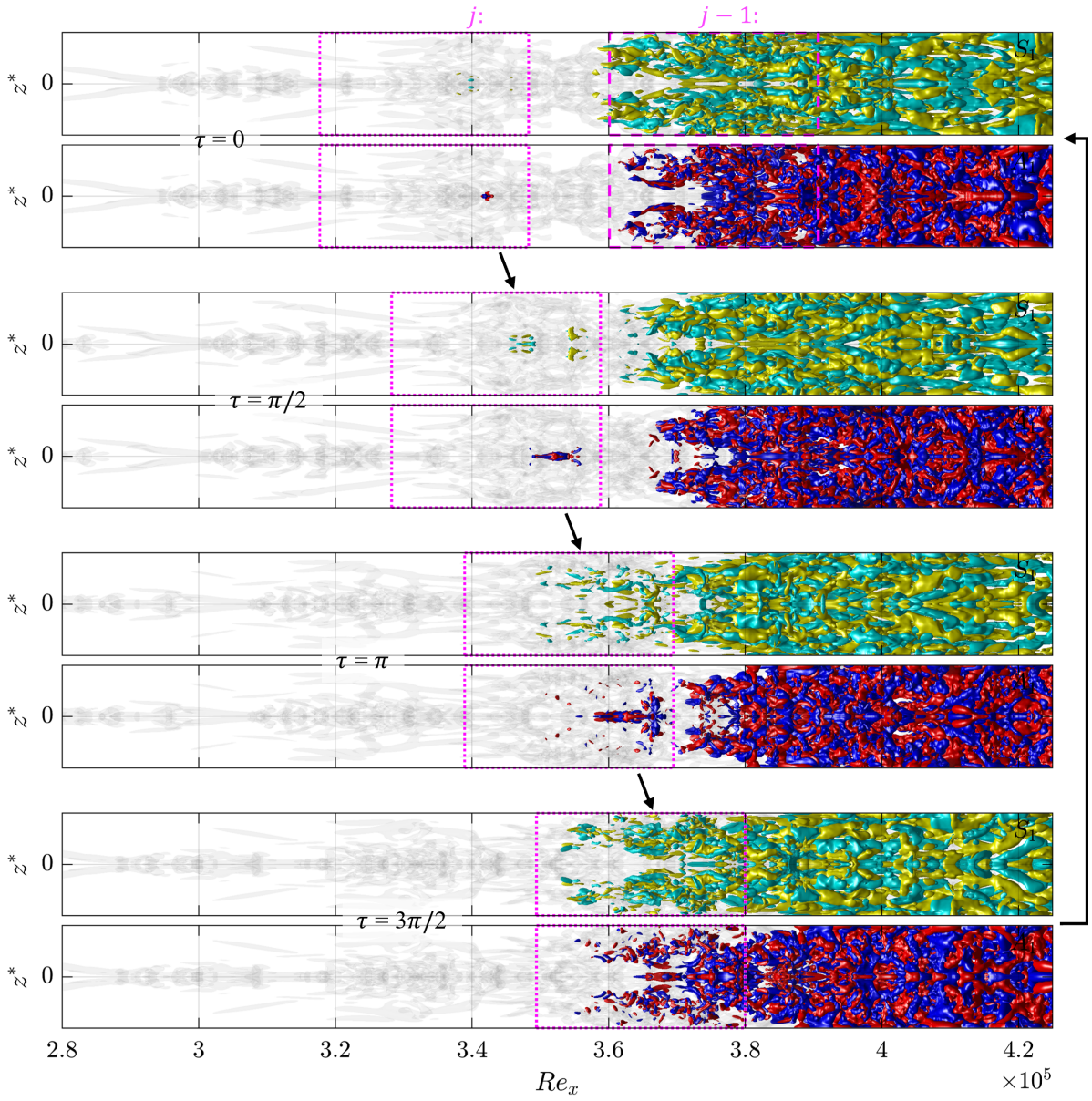


Figure 3.2. Periodic formation and convection of the leading symmetric and anti-symmetric seeds over one forcing period. Paired rows show the first symmetric and anti-symmetric STPOD modes, $\boldsymbol{\phi}_1^s$ and $\boldsymbol{\phi}_1^a$, at four equidistant phases $\tau = 0, \pi/2, \pi, 3\pi/2$, superposed on the FHR. Transparent grey isosurfaces depict the FHR Q-criterion at $Q = 10^3$. Yellow/cyan isosurfaces show the positive/negative streamwise-velocity component of $\boldsymbol{\phi}_1^s$ at $\pm 1.25 \times 10^{-2}$; red/blue isosurfaces analogously show the spanwise-velocity component of $\boldsymbol{\phi}_1^a$ at $\pm 1.25 \times 10^{-3}$. Magenta dotted outlines mark the traveling Moore neighbourhood used to track the amplifying seed. At $\tau = 0$, the dotted and dashed outlines identify consecutive seed realizations j and $j-1$.

spatially developing, time-periodic and spanwise-symmetric Fundamental Harmonic Response (FHR), whose mean, fundamental and higher harmonics contain the familiar vortical structures of K-type transition. Figure 3.1 makes the separation visible: the FHR captures the developed deterministic structure, while the symmetry decomposition exposes localized symmetric and anti-symmetric fluctuations that arise near the spanwise symmetry plane. Here, we use disturbance for weak background noise and seed for the first localized near-wall structure that emerges from it and amplifies as it convects downstream. Figure 3.2 follows the leading symmetric and anti-symmetric seeds over one forcing period and shows that both form and convect synchronously with the FHR, though their amplitudes vary between realizations. The symmetric seed therefore breaks time-periodicity, while the anti-symmetric seed additionally leaves the reflection-symmetric subspace. The present work explores whether these first seeds are linear instabilities of the FHR or products of an already nonlinear breakdown.

As the FHR is time-periodic, the natural view for this question is the stability of periodic solutions. In the forcing-phase-augmented formulation of a periodically driven system, an exact response that repeats after every forcing period corresponds to a *forced* limit cycle: a periodic orbit of the extended system (Guckenheimer and Holmes, 1983; Frantz et al., 2023) parametrized by the forcing input. Floquet stability is the cycle-to-cycle stability of periodic orbits. Linearization about the periodic response/orbit produces a linear time-periodic system, and advancing a small perturbation through one period defines a linear monodromy map. Its eigenvalues are the Floquet multipliers: a magnitude below unity implies cycle-to-cycle decay, whereas a magnitude above unity identifies an unstable direction that amplifies. A periodic response may therefore attract perturbations in some state-space directions while repelling them in others, making the corresponding periodic orbit saddle-type in the full state space. Classical secondary-instability theory applies this principle to finite-amplitude TS waves (Herbert, 1988), and subsequent analyses have extended it to more complex boundary-layer distortions (Liu et al., 2008). Floquet analysis has likewise identified three-dimensional and symmetry-breaking instabilities of time-periodic wakes (Barkley and Henderson, 1996; Blackburn et al., 2005).

More recently, data-driven learning of Poincaré maps has provided a route to nonlinear Floquet stability directly from observed trajectories (Bramburger and Kutz, 2020) and has been used to identify and stabilize periodic orbits (Bramburger et al., 2021). Here, we test the resulting saddle-type picture for the full spatially developed FHR and the seeds observed directly in DNS.

The DNS already contains the required perturbation trajectories, but extracting their cycle-to-cycle growth requires the appropriate frame of reference: it cannot be recovered at one fixed location. Once a periodically forced turbulent flow has reached cyclo-stationary equilibrium, each forcing period brings a new seed realization past a fixed observer; the resulting record does not follow the cycle-to-cycle evolution of any one seed. However, this evolution remains observable in the *spatial* development of the flow. As Fig. 3.3(b) shows, the symmetric and anti-symmetric fluctuations containing the seeds amplify rapidly in the streamwise direction. The seeds also convect synchronously with the FHR at a near-constant phase speed. Following the classical moving-frame treatment of secondary instability (Herbert, 1988) and the moving event-neighborhood strategy of Hack and Schmidt (2021), we exploit this synchronization to track each seed realization within a Moore neighborhood moving at their common convection speed. This moving view converts the spatial amplification into a finite-time Galilean trajectory and renders the local FHR quasi-steady, allowing the inference of an autonomous operator from multiple realizations.

Dynamic mode decomposition (DMD) can then be used as a data-driven algorithm to learn a one-step-forward map between consecutive states along these trajectories (Rowley et al., 2009; Schmid, 2010; Mezić, 2013). The measured linearity of the perturbation dynamics makes this a system-identification problem (Tu, 2013; Herrmann et al., 2021): the learned map is the local linear propagator governing the seed trajectories, and its eigendecomposition yields their growth rates and mode shapes in the Galilean frame. We do not assume this interpretation; we establish it through a series of independent checks against the governing equations and data: the exact symmetry-decomposed Navier–Stokes equations identify the common FHR-linearized dynamics; direct equation-term comparisons establish the seed-growth interval as a

linear perturbation regime; and spatial growth rates, held-out trajectories, independently obtained STPOD structures and mode-wise Floquet residuals cross-validate the inferred instability.

Using this framework, we identify the leading symmetric and anti-symmetric seeds as unstable structures of the FHR-linearized Floquet dynamics. Their receptivity pathways differ, but both amplify coherently and synchronously with the FHR until nonlinear saturation. Temporal symmetry breaking thus provides the required route from a deterministic harmonic state to broadband dynamics, while the anti-symmetric instability additionally drives the present flow out of the subspace of reflection-symmetric states. Once these fluctuations reach finite amplitude, their phase-averaged covariance feeds back on the FHR momentum balance and supplies the residual-stress contribution required to close its wall-stress budget near the skin-friction maximum. This feedback can be represented in the harmonic domain, but cannot be determined from the FHR harmonics alone. Symmetry breaking therefore performs two fundamental roles in canonical transition: it provides the linear route out of the deterministic harmonic regime and the nonlinear feedback required as the flow proceeds towards turbulence.

Section 3.2 introduces the FHR, symmetry decomposition and corresponding linear time-periodic stability framework. Section 3.3 identifies and validates the unstable seed dynamics, and section 3.4 connects them to the physical seed-formation mechanisms. Section 3.5 then examines their finite-amplitude feedback on the FHR and its implications for harmonic descriptions of transition.

3.2 Fundamental Harmonic Response (FHR) and symmetry-based stability framework

3.2.1 Direct numerical simulation and dataset

We compute deterministic K-type transition in a zero-pressure-gradient flat-plate boundary layer using the *CharLES* solver in DNS mode, without a subgrid-scale or wall model. A Blasius profile is prescribed at the inlet, the spanwise boundaries are periodic, and characteristic

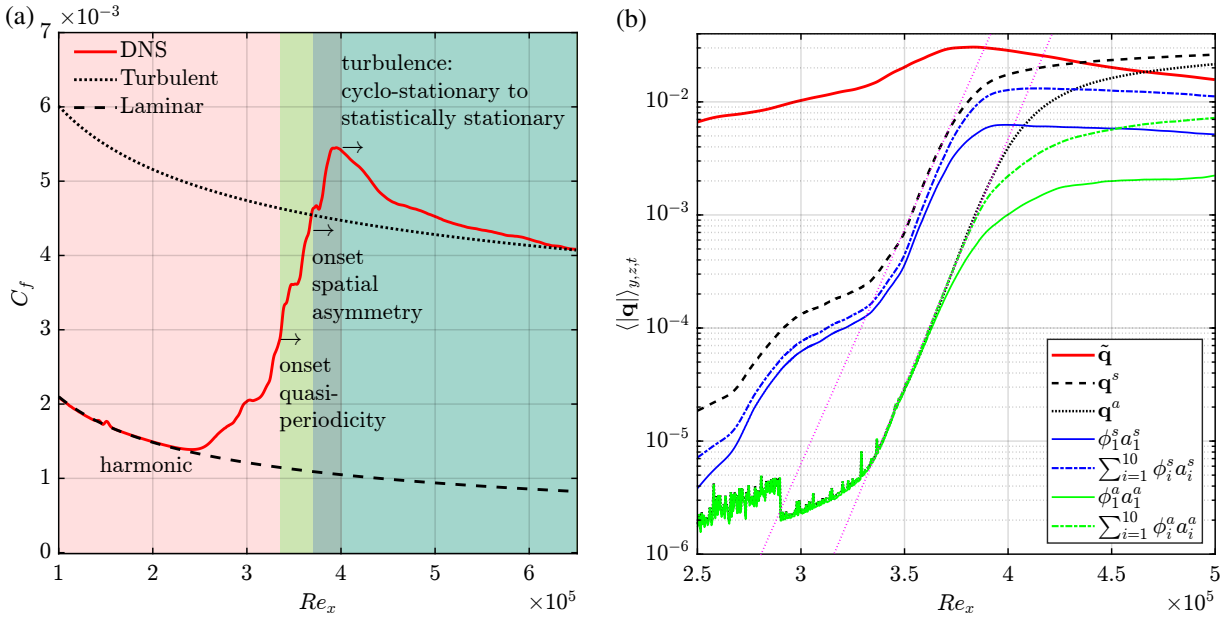


Figure 3.3. Streamwise evolution of the flow dynamics, shown through the skin-friction coefficient and the amplification and decay of distinct flow components. (a) DNS skin friction together with the laminar and turbulent correlations; background shading marks the harmonic, quasi-periodic, spatially asymmetric and turbulent regimes. After the C_f maximum, the flow evolves from cyclo-stationarity toward statistical stationarity, while C_f asymptotically approaches the broadband turbulent correlation. (b) Streamwise plot of time- and y-z-averaged vector amplitudes of the harmonic response $\tilde{\mathbf{q}}$ and the total symmetric and anti-symmetric fluctuations $\mathbf{q}^s$ and $\mathbf{q}^a$, together with their one- and ten-mode STPOD reconstructions. The harmonic response peaks immediately upstream of the C_f maximum and subsequently decays, while both fluctuations amplify rapidly. The magenta guide lines mark their amplification over $Re_x \approx 3.4$–3.8×10^5, before nonlinear saturation at finite amplitude.

conditions with sponge regions are applied at the outflow and far field. The flow has kinematic viscosity $\nu = 2 \times 10^{-6}$ and inlet Reynolds number $Re_x = 10^5$. With non-dimensional $y^* \equiv U_\infty y/\nu$ and $z^* \equiv U_\infty z/\nu$ coordinates, the domain spans $1 \times 10^5 < Re_x < 6.5 \times 10^5$, $0 < y^* < 1 \times 10^5$ and $-7.5 \times 10^3 < z^* < 7.5 \times 10^3$. The wall region uses a $N_x \times N_y \times N_z = 6400 \times 257 \times 128$ structured mesh with progressive wall-normal refinement and maintains $y^+ < 1$. Further details on the numerical setup and its validation are provided in Lin and Schmidt (2024).

The canonical modal transition is forced through a narrow, wall-normal velocity disturbance strip between $1.36 \times 10^5 < Re_x < 1.56 \times 10^5$. It introduces a spanwise-uniform periodic Tollmien–Schlichting (TS) wave of amplitude $A_a = 5 \times 10^{-3}$ and frequency $f_1 = 8.75$ with a weak spanwise-symmetric peak component of amplitude $A_s = 1.3 \times 10^{-4}$ (Rist and Fasel, 1995). The post-transient dataset contains 198 forcing periods $T = 1/f_1$, sampled at 128 equidistant phases per period, for statistical convergence of the FHR and dominant space-time modes. A complete discussion on the modal decompositions, characterizations and energy transfers is given in Lin and Schmidt (2026).

3.2.2 Spatio-temporal symmetry decomposition

We globally decompose the DNS field as

$$\boldsymbol{q}(\boldsymbol{x},t) = \tilde{\boldsymbol{q}}(\boldsymbol{x},t) + \boldsymbol{q}^s(\boldsymbol{x},t) + \boldsymbol{q}^a(\boldsymbol{x},t), \tag{3.1}$$

where $\tilde{\boldsymbol{q}}$ is the time-periodic, spanwise-symmetric *Fundamental Harmonic Response* (FHR), while $\boldsymbol{q}^s$ and $\boldsymbol{q}^a$ are the symmetric and anti-symmetric fluctuations about it.

The FHR is the finite-amplitude nonlinear flow response generated by the periodic TS-wave actuation. Following Lin and Schmidt (2026), we represent it through the leading symmetric SPOD modes at the harmonic frequencies $f_n = nf_1$,

$$\tilde{\boldsymbol{q}}(\boldsymbol{x},t) = \sum_n \hat{\boldsymbol{\psi}}_n^{(1)}(\boldsymbol{x}) a_n^{(1)} e^{i2\pi f_n t} + \bar{\boldsymbol{q}}(\boldsymbol{x}), \tag{3.2}$$

where $\hat{\boldsymbol{\psi}}_n^{(1)}$ and $a_n^{(1)}$ denote the leading SPOD mode (Lumley, 1970; Towne et al., 2018; Schmidt and Colonius, 2020) and its expansion coefficient at the n-th harmonic. Thus, $\tilde{\boldsymbol{q}}$ comprises the mean $\bar{\boldsymbol{q}}$, fundamental and higher harmonics generated by the nonlinear evolution of the forced TS wave. This harmonic state contains most of the familiar transitional vortex phenomena, including Λ-vortices, hairpin packets and their downstream evolution. Despite its turbulence-like appearance, the FHR is a single deterministic, time-periodic coherent structure. Its compact spatial support in Fig. 3.1 marks the finite streamwise reach of this deterministic harmonic regime, beyond which symmetry-breaking and broadband dynamics increasingly dominate. The FHR therefore provides the natural time-periodic base state for the stability analysis developed below.

As the present DNS is phase-locked and sampled at fixed forcing phases, the FHR also coincides with the phase mean of the data here and can be easily computed by phase averaging. However, the conceptual difference is important to note: phase averaging is a statistical operation, whereas the FHR is the physical harmonic response it happens to recover in this flow. While a phase mean can always be computed from suitably sampled data, it need not *generally* identify a dynamically/energetically meaningful flow structure.

Consequently, the decomposition in (3.1) has a direct interpretation. Upstream, the dynamics are entirely described by the periodic and spanwise-symmetric FHR. Subtracting this state from the DNS removes the deterministic phase-locked dynamics and leaves a cyclo-stationary fluctuation, $\boldsymbol{q}'' \equiv \boldsymbol{q} - \tilde{\boldsymbol{q}}$. Splitting this fluctuation by spanwise symmetry, $\boldsymbol{q}'' = \boldsymbol{q}^s + \boldsymbol{q}^a$, then isolates the two forms of symmetry-breaking by construction: The symmetric fluctuation $\boldsymbol{q}^s$ preserves spanwise reflection symmetry but is not phase-locked from one forcing period to the next, and therefore indicates the breaking of time-periodicity. The anti-symmetric fluctuation $\boldsymbol{q}^a$ likewise breaks time-periodicity in the present flow, but additionally introduces an (anti-)symmetry subspace absent from both the forcing and the FHR. Its appearance therefore marks the onset of spatial symmetry breaking. Growth of $\boldsymbol{q}^s$ and $\boldsymbol{q}^a$ fluctuations is thus the exact

signature by which the present flow departs from the deterministic harmonic regime.

We next formalize the spatial symmetry underlying this decomposition. Reflection about the spanwise midplane reverses the spanwise coordinate and, because velocity is a vector, also reverses the spanwise velocity component:

$$\mathscr{S}_z \boldsymbol{q}(x,y,z,t) = [u(x,y,-z,t),\, v(x,y,-z,t),\, -w(x,y,-z,t),\, p(x,y,-z,t)]^\top. \tag{3.3}$$

The corresponding projectors $\mathscr{P}_S = (I+\mathscr{S}_z)/2$ and $\mathscr{P}_A = (I-\mathscr{S}_z)/2$ extract the $+1$ and -1 eigenspaces of this reflection, respectively. Thus, $\boldsymbol{q}^S = \mathscr{P}_S \boldsymbol{q}$ and $\boldsymbol{q}^A = \mathscr{P}_A \boldsymbol{q}$, or explicitly

$$\boldsymbol{q}^S(x,y,z) = \frac{1}{2}\begin{bmatrix} u(x,y,z)+u(x,y,-z) \\ v(x,y,z)+v(x,y,-z) \\ w(x,y,z)-w(x,y,-z) \\ p(x,y,z)+p(x,y,-z) \end{bmatrix}, \tag{3.4}$$

$$\boldsymbol{q}^A(x,y,z) = \frac{1}{2}\begin{bmatrix} u(x,y,z)-u(x,y,-z) \\ v(x,y,z)-v(x,y,-z) \\ w(x,y,z)+w(x,y,-z) \\ p(x,y,z)-p(x,y,-z) \end{bmatrix}. \tag{3.5}$$

Accordingly, u, v and p are even and w is odd in the symmetric subspace, with the opposite parity in the anti-symmetric subspace. This decomposition is thus a linear operation and the full flow field is exactly recovered as $\boldsymbol{q} = \boldsymbol{q}^S + \boldsymbol{q}^A$.

As the geometry, forcing and FHR all preserve this transverse reflection symmetry, the deterministic periodic state resides entirely in the symmetric subspace. In the present configuration, any anti-symmetric component is therefore necessarily a symmetry-breaking fluctuation, so that $\boldsymbol{q}^A = \boldsymbol{q}^a$, while the full symmetric component contains the FHR together with the temporal symmetry-breaking fluctuation, $\boldsymbol{q}^S = \tilde{\boldsymbol{q}} + \boldsymbol{q}^s$. These two invariant parity classes

provide the natural starting point for the symmetry-decomposed Navier–Stokes equations derived next.

The effectiveness of eq. (3.1) is evident in the streamwise amplitudes of Fig. 3.3(b). The FHR dominates the upstream transitional flow before the symmetric and anti-symmetric fluctuations rapidly amplify as its amplitude saturates and subsequently declines. The decomposition therefore creates a highly effective multiscale separation: it isolates the nonlinear harmonic state from the fluctuations through which temporal and spatial symmetry breaking emerge, which in turn directly localize where the flow becomes significantly non-periodic or asymmetric.

As established in Lin and Schmidt (2026), the $\boldsymbol{q}^{s/a}$ fluctuation fields themselves possess a pronounced modal hierarchy. The earliest symmetric departures are dominated by the first two symmetric STPOD modes, ϕ_1^s and ϕ_2^s, whose T-periodic intra-cycle geometry is modulated by realization-dependent amplitudes. The onset of spatial asymmetry is similarly organized by the leading time-periodic anti-symmetric mode ϕ_1^a. Higher STPOD modes in both symmetry classes become increasingly aperiodic and constitute the broadband residual fluctuations associated with the subsequent progression towards turbulence (Fig. 3.3(a)).

This periodicity is not prescribed by STPOD. The decomposition maximizes captured space-time energy over a given finite time window (here chosen as $1T$) without imposing any particular time dynamics on its modes; they may therefore be periodic, aperiodic, or general transients depending on what is truly energetic in the data. The T-periodicity of ϕ_1^s, ϕ_2^s and ϕ_1^a is learned from a mostly phase-incoherent fluctuation field after the deterministic periodic FHR has already been removed, which may seem paradoxical at first. Figure 3.2 depicts the physical manifestation of this organization: the leading modes repeatedly form "seeds" that arise around the $z = 0$ symmetry plane, which convect and amplify in synchrony with the FHR (while their amplitudes vary between realizations). This combination of periodic intra-cycle geometry and realization-dependent amplitude motivates a central question pursued here: whether these leading symmetry-breaking modes are structural instability modes of the periodic FHR. The stability framework required to address this question is developed next.

3.2.3 Symmetry-decomposed Navier–Stokes equations and linear-time-periodic (LTP) stability framework

We next apply the same symmetry decomposition directly to the governing equations. Using the full velocity–pressure state $\boldsymbol{q} = [u_1, u_2, u_3, p]^\top = [\boldsymbol{u}, p]^\top$, we write $u_i = u_i^S + u_i^A$ and $p = p^S + p^A$. Substitution into the incompressible Navier–Stokes equations (NSE) followed by projection onto the two reflection subspaces gives the exact systems

$$\frac{\partial u_i^S}{\partial t} + u_j^S \frac{\partial u_i^S}{\partial x_j} + u_j^A \frac{\partial u_i^A}{\partial x_j} = -\frac{\partial p^S}{\partial x_i} + \nu \frac{\partial^2 u_i^S}{\partial x_j^2}, \qquad \text{with} \quad \frac{\partial u_i^S}{\partial x_i} = 0, \tag{3.6}$$

$$\frac{\partial u_i^A}{\partial t} + u_j^S \frac{\partial u_i^A}{\partial x_j} + u_j^A \frac{\partial u_i^S}{\partial x_j} = -\frac{\partial p^A}{\partial x_i} + \nu \frac{\partial^2 u_i^A}{\partial x_j^2}, \qquad \text{with} \quad \frac{\partial u_i^A}{\partial x_i} = 0. \tag{3.7}$$

Reflection symmetry imposes a simple selection rule on the nonlinear interactions. Products of fields with the same parity feed the symmetric subspace, while mixed symmetric–anti-symmetric interactions feed the anti-symmetric subspace. Consequently, the symmetric equation contains the *SS* and *AA* interactions, whereas the anti-symmetric equation contains only the mixed *SA* interactions. Equations (3.6) and (3.7) are thus an exact repartition of the full NSE and could be solved on a half-domain.

To expose the stability problem about the FHR, we now separate the periodic base state from the fluctuations within these two exact symmetry classes,

$$\boldsymbol{q}^S(\boldsymbol{x},t) = \tilde{\boldsymbol{q}}(\boldsymbol{x},t) + \boldsymbol{q}^s(\boldsymbol{x},t), \qquad \boldsymbol{q}^A(\boldsymbol{x},t) = \boldsymbol{q}^a(\boldsymbol{x},t), \tag{3.8}$$

where $\tilde{\boldsymbol{q}} = [\tilde{\boldsymbol{u}}, \tilde{p}]^\top$ and $\boldsymbol{q}^{s/a} = [\boldsymbol{u}^{s/a}, p^{s/a}]^\top$. We note that equation (3.8) (or equivalently (3.1)) is an exact decomposition of the DNS field throughout the entire domain. However, its applicability as a perturbation expansion is more restrictive and is used only where $\boldsymbol{q}^{s/a}$ remains verifiably small relative to the FHR.

For this purpose, we classify terms by their degree in the fluctuation amplitudes: FHR-

only terms are nominally zeroth order, terms containing one factor of $\boldsymbol{q}^{s/a}$ are first order, and products of two fluctuations are second order. Inserting $\boldsymbol{q}^A = \boldsymbol{q}^a$ into the anti-symmetric equation gives

$$\underbrace{\frac{\partial u_i^a}{\partial t} + \tilde{u}_j \frac{\partial u_i^a}{\partial x_j} + u_j^a \frac{\partial \tilde{u}_i}{\partial x_j} + \frac{\partial p^a}{\partial x_i} - \nu \frac{\partial^2 u_i^a}{\partial x_j^2}}_{1^{st}\text{-order anti-symmetric fluctuation terms}} = \underbrace{-\left(u_j^s \frac{\partial u_i^a}{\partial x_j} + u_j^a \frac{\partial u_i^s}{\partial x_j} \right)}_{2^{nd}\text{-order terms } \mathscr{N}_i^a(u^s,u^a)} + \underbrace{0}_{\substack{0^{th}\text{-order} \\ \text{(no anti-sym.} \\ \text{base flow)}}} . \tag{3.9}$$

There is no zeroth-order anti-symmetric contribution as the FHR is strictly symmetric. The leading dynamics for the anti-symmetric fluctuation $\boldsymbol{q}^a$ are therefore linear about the FHR, while coupling to the symmetric fluctuations enters only at second order through $\mathscr{N}_i^a$.

Similarly, substituting $\boldsymbol{q}^S = \tilde{\boldsymbol{q}} + \boldsymbol{q}^s$ into the symmetric equation gives

$$\begin{aligned} \underbrace{\frac{\partial u_i^s}{\partial t} + \tilde{u}_j \frac{\partial u_i^s}{\partial x_j} + u_j^s \frac{\partial \tilde{u}_i}{\partial x_j} + \frac{\partial p^s}{\partial x_i} - \nu \frac{\partial^2 u_i^s}{\partial x_j^2}}_{1^{st}\text{-order symmetric fluctuation terms}} &= \underbrace{-\left(u_j^s \frac{\partial u_i^s}{\partial x_j} + u_j^a \frac{\partial u_i^a}{\partial x_j} \right)}_{2^{nd}\text{-order terms } \mathscr{N}_i^s(u^s,u^a)} \\ &\quad \underbrace{- \left(\frac{\partial \tilde{u}_i}{\partial t} + \tilde{u}_j \frac{\partial \tilde{u}_i}{\partial x_j} + \frac{\partial \tilde{p}}{\partial x_i} - \nu \frac{\partial^2 \tilde{u}_i}{\partial x_j^2} \right)}_{0^{th}\text{-order base-state residual } \tilde{\mathscr{R}}_i^s(\tilde{\boldsymbol{q}})} . \end{aligned} \tag{3.10}$$

Thus, the symmetric fluctuation $\boldsymbol{q}^s$ has the same FHR-linearized first-order dynamics, accompanied by quadratic symmetric forcing $\mathscr{N}_i^s$ and the base-state residual $\tilde{\mathscr{R}}_i^s$. The latter can, at first glance, be viewed as the residual obtained by evaluating the Navier–Stokes equations on the empirical FHR base state, so it is nominally 0^{th}-order. Indeed, we find that $\tilde{\mathscr{R}}^s \simeq 0$ where the chosen base state $\tilde{\boldsymbol{q}}$ satisfies the NSE well.

However, upon closer inspection, the latter has a direct physical interpretation: Phase-averaging the exact symmetric equation (3.10) yields the time-periodic identity

$$\underbrace{\frac{\partial \tilde{u}_i}{\partial t} + \tilde{u}_j \frac{\partial \tilde{u}_i}{\partial x_j} + \frac{\partial \tilde{p}}{\partial x_i} - \nu \frac{\partial^2 \tilde{u}_i}{\partial x_j^2}}_{0^{th}\text{-order base-state residual } \tilde{\mathscr{R}}_i^s(\tilde{\boldsymbol{q}})} = \underbrace{-\left(\widetilde{u_j^s \frac{\partial u_i^s}{\partial x_j}} + \widetilde{u_j^a \frac{\partial u_i^a}{\partial x_j}} \right)}_{2^{nd}\text{-order periodic term}}, \qquad \frac{\partial \tilde{u}_i}{\partial x_i} = 0. \tag{3.11}$$

Thus, $\tilde{\mathscr{R}}^s$ exactly equates the mean quadratic feedback of the symmetry-breaking fluctuations on the empirical FHR at each forcing phase. Hence, $\tilde{\mathscr{R}}^s$ is 2^{nd}-order in our case, and thereby small within the early linear-growth region considered for stability analysis. However, we foreshadow here that they need not be insignificant once the fluctuations reach finite amplitude. We further remark that averaging eq. (3.11) again over the forcing period yields the well-established (time-averaged) Reynolds-averaged Navier–Stokes (RANS) equations.

Collecting the first-order terms for both symmetry classes gives a common time-periodic linear operator in primitive-variable form,

$$\underbrace{\begin{bmatrix} I & 0 \\ 0 & 0 \end{bmatrix}}_{\mathscr{M}} \frac{\partial}{\partial t} \begin{bmatrix} \boldsymbol{u}^{s/a} \\ p^{s/a} \end{bmatrix} = \underbrace{\begin{bmatrix} -\big(\tilde{\boldsymbol{u}}(t)\cdot\boldsymbol{\nabla}\big)\{\cdot\} - \big(\{\cdot\}\cdot\boldsymbol{\nabla}\big)\tilde{\boldsymbol{u}}(t) + \nu\Delta\{\cdot\} & -\boldsymbol{\nabla}\{\cdot\} \\ \boldsymbol{\nabla}\cdot\{\cdot\} & 0 \end{bmatrix}}_{\mathscr{A}(t)\text{ Linear Time-Periodic NSE operator}} \begin{bmatrix} \boldsymbol{u}^{s/a} \\ p^{s/a} \end{bmatrix} + \begin{bmatrix} \boldsymbol{f}^{s/a} \\ 0 \end{bmatrix}. \tag{3.12}$$

Here, $\mathscr{A}(t)$ is the Navier–Stokes operator linearized about the T-periodic FHR velocity $\tilde{\boldsymbol{u}}(t)$, while pressure remains the algebraic constraint enforcing incompressibility. The remaining terms $\boldsymbol{f}^a = \mathscr{N}^a$ and $\boldsymbol{f}^s = \mathscr{N}^s - \tilde{\mathscr{R}}^s$ describe the exact departures from the linear dynamics.

After spatial discretization and collecting the velocity and pressure into vectors $\mathbf{q}^{s/a} = [(\mathbf{u}^{s/a})^\top, (\mathbf{p}^{s/a})^\top]^\top$, the symmetric and anti-symmetric equations then take the semi-discretized unified descriptor form

$$\begin{gathered} \mathbf{M}\frac{d\mathbf{q}^{s/a}}{dt} = \mathbf{A}(t)\mathbf{q}^{s/a} + \mathbf{f}^{s/a}, \qquad \mathbf{A}(t+T) = \mathbf{A}(t), \\ \mathbf{f}^s = \underbrace{\begin{bmatrix} \mathbf{N}^s - \tilde{\mathbf{R}}^s \\ 0 \end{bmatrix}}_{2^{nd}\text{-order}}, \qquad \mathbf{f}^a = \underbrace{\begin{bmatrix} \mathbf{N}^a \\ 0 \end{bmatrix}}_{2^{nd}\text{-order}}. \end{gathered} \tag{3.13}$$

The detailed semi-discrete formulation and its component operators are given in Appendix 3.8.1.

Since the FHR is T-periodic and symmetric in z, $\mathbf{A}(t)$ is a linear time-periodic (LTP) Navier–Stokes operator, belonging to the symmetric class: it preserves both parity subspaces.

Consequently, $\mathbf{q}^s$ and $\mathbf{q}^a$ evolve under the *same* FHR-linearized operator, and are restricted to the symmetric and anti-symmetric (i.e., their own) subspaces, respectively. In other words, at first order, a symmetric disturbance cannot generate an anti-symmetric evolution and vice versa. Quadratic and residual contributions only enter through the class-specific terms $\mathbf{f}^{s/a}$ at higher-order.

Equations (3.12) and (3.13) remain exact rearrangements of the symmetry-decomposed NSE. Their usefulness here is that every term is available directly or post-computable from the DNS data, allowing the validity of a linear stability description to be tested rather than assumed.

Figure 3.4(a) provides the first part of this test. Within the growth window of interest, the FHR residual $|\tilde{\mathbf{R}}^s|$ remains at least one order of magnitude smaller than both the FHR dynamics and symmetric-fluctuation dynamics in the L_2 vector norm. The class-specific nonlinear contributions are evaluated separately along the tracked seed trajectories in Section 3.3 and are likewise negligible over the corresponding amplification windows (Fig. 3.6(a_3,b_3)). Together, these measured comparisons show that the fluctuation dynamics can be treated as effectively homogeneous (unforced) over this interval,

$$\mathbf{M}\frac{d}{dt}\mathbf{q}^{s/a} \approx \mathbf{A}(t)\,\mathbf{q}^{s/a}. \tag{3.14}$$

This approximation is an a posteriori characterization of the DNS dynamics, *not* an imposed assumption or synthesis of idealized linear trajectories. In other words, the DNS symmetry-breaking seed trajectories already behave as linear perturbations within the window of interest. Hence, this measured dominance of the first-order dynamics permits the subsequent operator inference in Section 3.3 to be interpreted as system identification of the underlying stability operator.

Since $\mathbf{A}(t+T) = \mathbf{A}(t)$, solutions of the homogeneous system admit the Floquet form

$$\mathbf{q}'(t) = \varphi(t)\,e^{\mu t}, \qquad \varphi(t+T) = \varphi(t), \tag{3.15}$$

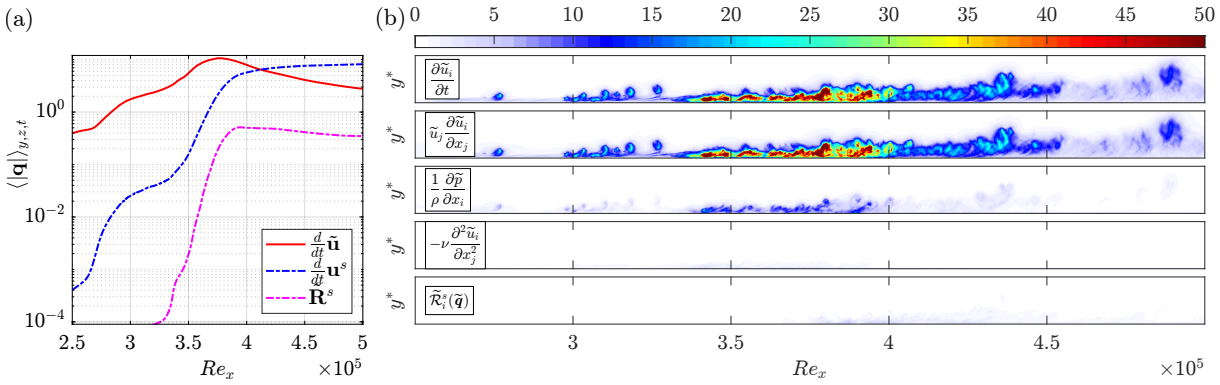


Figure 3.4. (a): Amplitude scale comparison of various terms in the symmetric Navier-Stokes equations (3.10) and phase-averaged Navier-Stokes equations (3.11), measured in their expected vector amplitude (integrated in y, z and averaged in time) as a function of Re_x. **(b)**: Instantaneous vector amplitudes (integrated in z) of the terms within the symmetric phase-averaged Navier-Stokes equations (3.11).

where μ is the Floquet exponent and $\varphi(t)$ is the corresponding T-periodic mode structure. This ansatz provides the dynamical form against which leading symmetric and anti-symmetric seeds are tested in later sections.

3.2.4 Galilean LTP-to-LTI reduction

We exploit the Galilean invariance of the NSE and transform into a coordinate system with more favorable mathematical representation to isolate the instability physics. We transform to a frame moving with a selected bulk FHR tracking speed c_x,

$$\underline{x} = x - c_x t, \qquad \underline{t} = t, \tag{3.16}$$

and track localized seed trajectories inside the bounds of a traveling Moore neighborhood (Fig. 3.5(b)). We show in the following that this transformation can simplify the analysis by effectively removing the periodic time dependence of the base flow that largely convects instabilities at the selected speed.

Consider an instability wave with streamwise wavenumber α, frequency ω, and real

temporal growth rate μ. Its laboratory- and moving-frame representations are

$$\begin{aligned} \boldsymbol{q}(x,y,z,t) &= \hat{\boldsymbol{q}}(y,z)\exp(i\alpha x - i\omega t + \mu t)\,, \\ \underline{\boldsymbol{q}}(\underline{x},y,z,t) &= \hat{\boldsymbol{q}}(y,z)\exp(i\alpha\underline{x})\exp(\mu t + i(\alpha c - \omega)t)\,, \end{aligned} \tag{3.17}$$

where $x = \underline{x} + ct$ and c denotes an arbitrary frame speed. The factor $\exp(\mu t)$ governs amplification or decay, while $\exp\big(i(\alpha c - \omega)t\big)$ describes phase drift relative to the moving frame. For the synchronous choice $c = \omega/\alpha$, this phase drift vanishes and

$$\underline{\boldsymbol{q}} = \hat{\boldsymbol{q}}(y,z)\exp(i\alpha\underline{x})\exp(\mu t)\,. \tag{3.18}$$

The mode is then stationary in $\underline{x}$ and changes only in amplitude. For a non-synchronous mode, μ remains its temporal growth rate and the frequency mismatch produces residual phase drift or oscillations.

The same cancellation applies to a traveling harmonic of a base velocity field:

$$\begin{aligned} \boldsymbol{u}(x,y,z,t) &= \hat{\boldsymbol{u}}(y,z)\exp(i\alpha x - i\omega t)\,, \\ \underline{\boldsymbol{u}}(\underline{x},y,z,t) &= \hat{\boldsymbol{u}}(y,z)\exp(i\alpha\underline{x})\exp[i(\alpha c - \omega)t] \xrightarrow{c=\omega/\alpha} \hat{\boldsymbol{u}}(y,z)\exp(i\alpha\underline{x})\,. \end{aligned} \tag{3.19}$$

A synchronous frame therefore removes the explicit time-periodicity of the traveling base wave while isolating the exponential growth of the disturbance.

This methodology underlies the classical secondary-instability framework of Herbert (1988). There, a finite-amplitude traveling TS wave superposed on the steady laminar solution forms the time-periodic base velocity field in the laboratory frame. The corresponding perturbation problem is LTP, but becomes LTI via the above methodology as the primary wave is

rendered effectively quasi-steady in its synchronous Galilean frame:

$$\begin{aligned} \mathbf{M}\frac{d}{dt}\mathbf{q}^{(2)} &= \mathbf{A}\big(\mathbf{u}^{(1)}(t)\big)\mathbf{q}^{(2)}, \quad \text{laboratory frame (LTP)}, \\ \mathbf{M}\frac{d}{dt}\underline{\mathbf{q}}^{(2)} &= \underline{\mathbf{A}}\big(\underline{\mathbf{u}}^{(1)}\big)\underline{\mathbf{q}}^{(2)}, \qquad \text{Galilean frame (LTI)}. \end{aligned} \tag{3.20}$$

Here, quasi-steady means that the co-moving base velocity changes only slowly over the growth interval of the secondary disturbance. Together with local parallelism and weak nonlinear distortion, this separation of rates permits the base velocity and its linearized operator to be treated as locally frozen. The Galilean transformation thus reduces the time-Floquet problem to an autonomous LTI eigenvalue problem. The core result Herbert (1988) found is that the most amplified secondary modes have a real eigenvalue and travel phase-locked with the primary TS wave, as this synchronization provides the optimal condition for energy transfer into the three-dimensional instability. As we will show in Sec. 3.3, this result of classical secondary-instability theory is highly relevant for symmetry-breaking instabilities of the FHR.

The present flow uses the FHR in lieu of the finite-amplitude primary wave, while the symmetric and anti-symmetric seeds form the disturbances evolving about it. Their stationary-frame dynamics follow the homogeneous LTP system in equation (3.14). Over the tracked linear-growth interval, however, the seed amplitudes increase by several orders of magnitude while the FHR amplitude changes comparatively slowly (as seen in Fig. 3.3(b)). The relevant FHR dynamic is that sampled within the predominantly near-wall spatial support of the instability. The speed c_x removes its leading convection there, which coincides with the speed of the instability seeds. While the y-variation of phase speed can produce slower residual phase drift/elongation closest to the wall and faster convection by the hairpin heads near the freestream, neither of these effects happen to affect the initial seed formation and growth dominantly. The moving-frame FHR is therefore also locally quasi-steady relative to each tracked seed trajectory,

$$\underline{\tilde{\boldsymbol{u}}}(\underline{x},y,z,t) \approx \underline{\tilde{\boldsymbol{u}}}(\underline{x},y,z),$$

and the inertial-frame LTP dynamics from equation (3.14) simplifies locally to

$$\mathbf{M}\frac{d}{dt}\underline{\mathbf{q}}^{s/a} = \underline{\mathbf{A}}\big(\underline{\tilde{\mathbf{u}}}\big)\underline{\mathbf{q}}^{s/a}, \tag{3.21}$$

which is LTI. Equation (3.21) thus provides the local linear model ansatz for the operator inferred from tracked DNS seed trajectories in Sec. 3.3.

3.3 Linear amplification of symmetry-breaking seeds

We now identify the local linear Galilean operator that Equation (3.21) requires directly from tracked DNS trajectories. To that end, we deploy a multi-trajectory adaptation of DMD to identify the local linear propagator. As the nonlinear and residual terms remain demonstrably small relative to $d\underline{\mathbf{q}}^{s/a}/dt$ within the region of interest, this approach constitutes a *system-identification* procedure, rather than merely a reduced-order surrogate model of the data. Its eigendecomposition then naturally reflects a data-driven stability analysis that yields Galilean-frame growth rates and mode shapes of the seed dynamics. Contrary to Herbert's secondary-instability analysis, which prescribes a streamwise Floquet basis *a priori* (Herbert, 1988) due to streamwise periodicity assumptions, the spatially developing boundary layer exhibits no natural prescribed streamwise periodicity. Thus, both the reduced operator and the spatial basis on which it acts are inferred from an ensemble of tracked DNS seed trajectories.

3.3.1 Seed tracking and data-driven operator inference

The phase-resolved amplitudes in Fig. 3.5(a) reveal the intra-period evolution of both symmetric and anti-symmetric seed fluctuations, while the corresponding space–time diagrams in Fig. 3.5(b) identify their common bulk convection speed, $c_x \simeq 0.741U_\infty$. This speed defines the Galilean frame in which individual seed realizations are tracked. The magenta bounds enclose the relevant space–time fluctuation band over the fitted growth interval; leakage through these bounds marks the limit of the localized-window approximation. The seeds from each realization

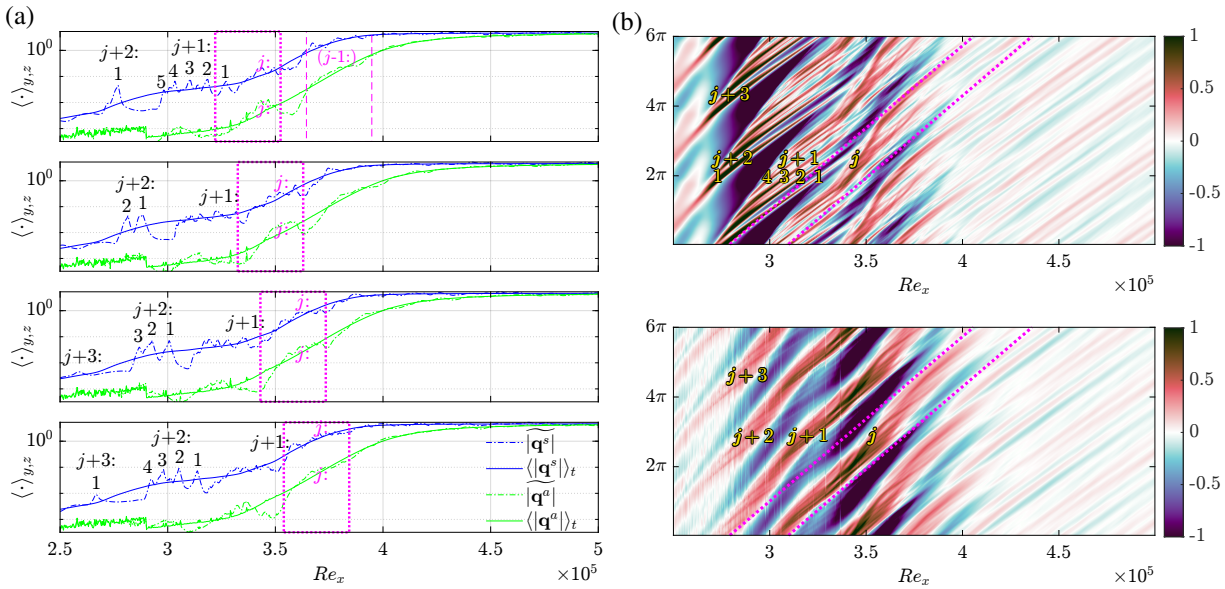


Figure 3.5. Phase-resolved fluctuations and space–time contours used to estimate the moving frame. **(a)** Streamwise amplitudes of symmetric and anti-symmetric fluctuations (in their expected vector amplitude, ensemble-averaged over the dataset) at four equidistant phases, $\{0, \pi/2, \pi, 3\pi/2\}$ from top to bottom. **(b)** Space–time diagram of the same quantities, with the symmetric component above and the anti-symmetric component below, concatenated over three periods for ease of visualization. The dominant space-time fluctuation band exhibits a slope of $c_x \simeq 0.741 U_\infty$, and the magenta lines mark the corresponding moving Moore-neighborhood bounds used for operator inference.

are followed for $3T$ inside a traveling Moore neighborhood spanning $\Delta Re_x \simeq 3.06 \times 10^4$, $0 \leq y^* \leq 8.83 \times 10^3$, and $-7.5 \times 10^3 \leq z^* \leq 0$ on the symmetry-reduced half-span. The spatial extent of this neighborhood is visualized in Fig. 3.1.

For operator inference, we restrict these trajectories to one-period windows sampled from the streamwise region in which both symmetry classes exhibit pronounced linear growth in the stationary-frame diagnostics of Fig. 3.3. This is the regime in which the homogeneous linear approximation of Eq. (3.14) is supported: the measured nonlinear and residual contributions remain negligible relative to the first-order dynamics. Each regression window contains $N_T + 1 = 129$ consecutive states spanning one forcing period plus the first state of the next period. While the full $3T$ trajectories are retained for seed tracking, the inferred operator and its stability interpretation are restricted to this one-period growth window.

For each symmetry class, the input and output pairs of M independently tracked realizations are assembled as

$$\underline{\mathbf{X}}^{s/a}_{\mathscr{J}} = \left[\underline{\mathbf{X}}^{s/a}_1 \quad \underline{\mathbf{X}}^{s/a}_2 \quad \cdots \quad \underline{\mathbf{X}}^{s/a}_M\right], \qquad \underline{\mathbf{Y}}^{s/a}_{\mathscr{J}} = \left[\underline{\mathbf{Y}}^{s/a}_1 \quad \underline{\mathbf{Y}}^{s/a}_2 \quad \cdots \quad \underline{\mathbf{Y}}^{s/a}_M\right], \tag{3.22}$$

to form an ensemble $\mathscr{J}$, where

$$\underline{\mathbf{X}}^{s/a}_j = \left[\underline{\mathbf{u}}^{s/a}_{0,j} \quad \cdots \quad \underline{\mathbf{u}}^{s/a}_{N_T-1,j}\right], \qquad \underline{\mathbf{Y}}^{s/a}_j = \left[\underline{\mathbf{u}}^{s/a}_{1,j} \quad \cdots \quad \underline{\mathbf{u}}^{s/a}_{N_T,j}\right], \tag{3.23}$$

that is, $\underline{\mathbf{X}}^{s/a}_j$ and $\underline{\mathbf{Y}}^{s/a}_j$ contain the same time-ordered trajectory with the latter shifted forward by one snapshot.

The corresponding least-squares best-fit operator,

$$\underline{\mathbf{A}}^{s/a} = \underline{\mathbf{Y}}^{s/a}_{\mathscr{J}} \left(\underline{\mathbf{X}}^{s/a}_{\mathscr{J}}\right)^{\dagger},$$

is necessarily rank-deficient in the original spatial coordinates, since the number of spatial

degrees of freedom greatly exceeds the number of available snapshots. Therefore, we instead compute the compact singular value decomposition

$$\underline{\mathbf{X}}^{s/a}_{\mathscr{J}} = \underline{\mathbf{U}}^{s/a}\boldsymbol{\Sigma}^{s/a}\left(\mathbf{V}^{s/a}\right)^{\top}, \tag{3.24}$$

and infer the reduced operator

$$\underline{\mathbf{A}}^{s/a}_{r} = \left(\underline{\mathbf{U}}^{s/a}\right)^{\top}\underline{\mathbf{Y}}^{s/a}_{\mathscr{J}}\mathbf{V}^{s/a}\left(\boldsymbol{\Sigma}^{s/a}\right)^{-1} = \left(\underline{\mathbf{U}}^{s/a}\right)^{\top}\underline{\mathbf{A}}^{s/a}\underline{\mathbf{U}}^{s/a}. \tag{3.25}$$

The resulting model advances the POD coefficient vector according to

$$\mathbf{a}^{s/a}_{k+1} \approx \underline{\mathbf{A}}^{s/a}_{r}\mathbf{a}^{s/a}_{k}, \qquad \underline{\mathbf{u}}^{s/a}_{k} \approx \underline{\mathbf{U}}^{s/a}\mathbf{a}^{s/a}_{k}, \tag{3.26}$$

where $\underline{\mathbf{u}}^{s/a}_{k}$ denotes the reconstructed seed state within the moving neighborhood at discrete time step k.

The columns of $\underline{\mathbf{U}}^{s/a}$ are constructed exclusively from velocity snapshots that already satisfy incompressibility and therefore span a divergence-free reduced state space. Projection onto this basis eliminates the need for the pressure constraint together with the singular mass matrix $\mathbf{M}$, leaving a standard velocity evolution problem in coefficient space. Although the same FHR-linearized operator governs both symmetry classes and leaves their parity subspaces invariant, we infer $\underline{\mathbf{A}}^{s}_{r}$ and $\underline{\mathbf{A}}^{a}_{r}$ independently. Their POD bases $\underline{\mathbf{U}}^{s}$ and $\underline{\mathbf{U}}^{a}$ are different, and separate regressions preserve parity invariance, prevent symmetry mixing, and expose the growth rates and mode shapes specific to each symmetry-breaking mechanism.

The eigendecomposition

$$\underline{\mathbf{A}}^{s/a}_{r}\mathbf{W}^{s/a} = \mathbf{W}^{s/a}\boldsymbol{\Lambda}^{s/a}, \qquad \boldsymbol{\Omega}^{s/a} = \frac{\log\left(\boldsymbol{\Lambda}^{s/a}\right)}{\Delta t}, \tag{3.27}$$

defines the projected DMD modes

$$\underline{\boldsymbol{\Xi}}^{s/a} = \underline{\mathbf{U}}^{s/a}\mathbf{W}^{s/a}. \tag{3.28}$$

The evolution of any seed realization j is consequently represented as

$$\underline{\mathbf{u}}_j^{s/a}(\underline{x},y,z,t) = \underline{\boldsymbol{\Xi}}^{s/a}(\underline{x},y,z)\, e^{\boldsymbol{\Omega}^{s/a}t}\, \mathbf{b}_{0,j}, \qquad \mathbf{b}_{0,j} = \left(\underline{\boldsymbol{\Xi}}^{s/a}\right)^{\dagger} \underline{\mathbf{u}}_{0,j}^{s/a}, \tag{3.29}$$

where $\mathbf{b}_{0,j}$ is the projection of an initial seed state onto the inferred eigenmode basis.

The real parts of the eigenvalues in $\boldsymbol{\Omega}^{s/a}$ quantify amplification or decay in the Galilean frame, while their imaginary parts measure phase motion relative to the selected bulk speed c_x. Relative motion may arise from shear-induced deformation and drift, real oscillatory dynamics, or finite-window and model error. The DMD eigendecomposition eq. (3.29) therefore constitutes a data-driven stability analysis of the seed dynamics: its modes are high-dimensional eigenfunctions of the inferred local linear operator, restricted to the divergence-free POD subspace sampled by the tracked DNS trajectories.

3.3.2 Eigenspectra, growth-rate consistency, and linearity tests

The inferred symmetric and anti-symmetric operators are each dominated by a single unstable mode with a real continuous-time eigenvalue, $\omega_r^s \approx 31.0$ and $\omega_r^a \approx 34.17$, respectively (Fig. 3.6(a_2) and Fig. 3.6(b_2)). Subdominant eigenvalues correspond to weaker amplifying or decaying modes that are required to recompose the inherently multiscale structure of the amplifying seeds, with non-zero imaginary parts describing oscillation or phase drift relative to the selected Galilean speed. The dominant real eigenvalues are therefore precisely the spectral signature expected for seeds that amplify approximately synchronously with the FHR: their leading convection is removed by the Galilean transformation, leaving primarily exponential amplification in time.

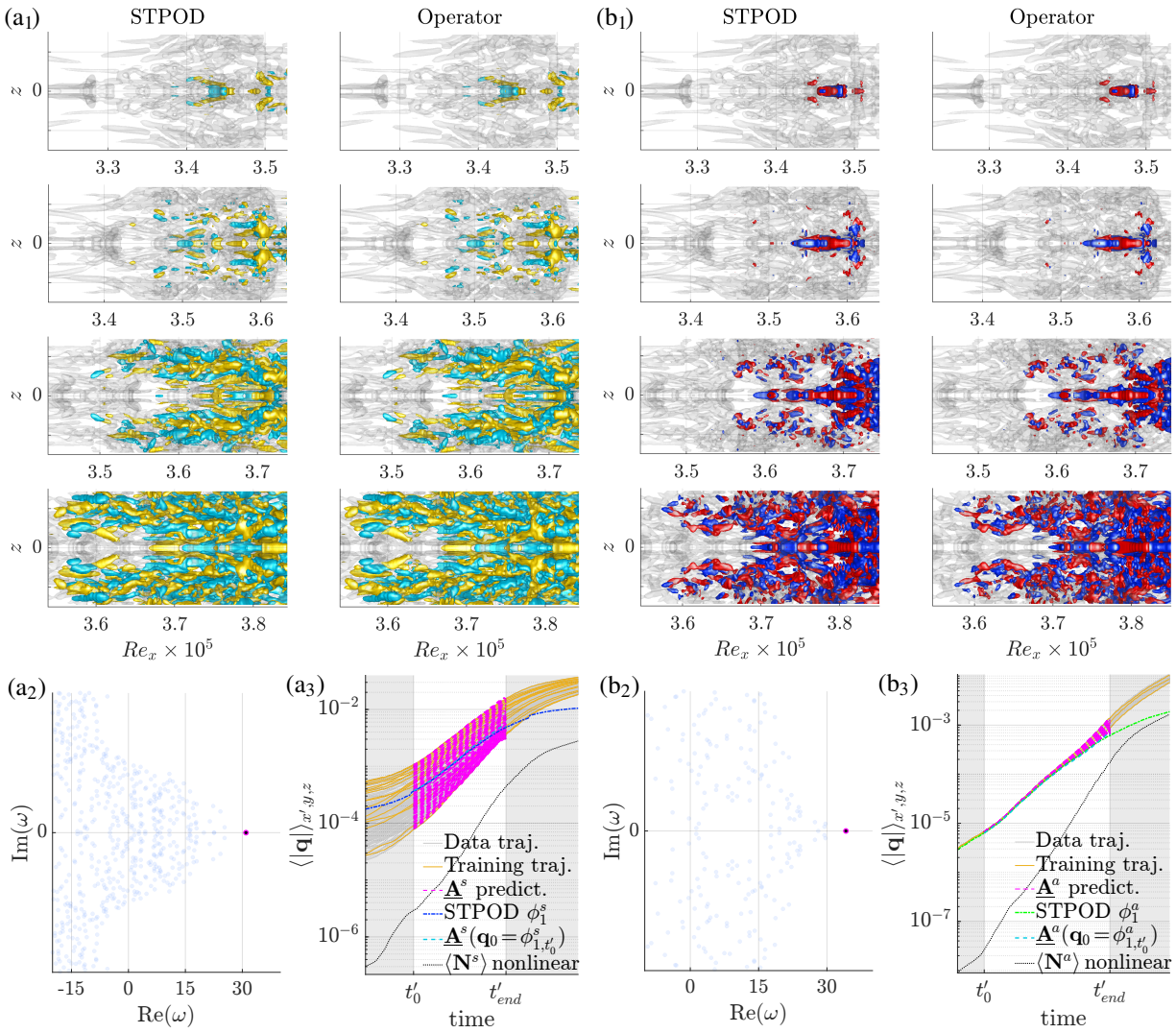


Figure 3.6. Results of the multi-trajectory Galilean operator inference. Left half: symmetric component $\mathbf{q}^s$. Right half: anti-symmetric component $\mathbf{q}^a$. Panels (a_1,b_1) compare the operator-predicted spatio-temporal evolution of the seed with the corresponding dominant STPOD mode, panels (a_2,b_2) show the eigenspectra of the learned Galilean operators, and panels (a_3,b_3) compare measured DNS seed amplitudes with operator predictions and nonlinear contributions; grey bands delimit the Galilean operator prediction window.

This result can be tested directly against the laboratory-frame *spatial* amplification in Fig. 3.3(b): Under the approximation of constant phase speed c_x for convected $\mathbf{q}^{s/a}$ fluctuations, the measured spatial logarithmic slope can be transformed into a temporal growth rate via

$$\mu_{x\to t} = \frac{d\ln(A)}{dRe_x}\frac{dRe_x}{dt} \approx \frac{\Delta\ln(A)}{\Delta Re_x}\frac{U_\infty c_x}{\nu}. \tag{3.30}$$

Fitting the marked linear-growth windows in Fig. 3.3(b) and using $c_x = 0.741U_\infty$ yields

$$\mu^s_{x\to t} \approx 33.26, \qquad \mu^a_{x\to t} \approx 35.11.$$

These laboratory-frame estimates agree with the corresponding Galilean eigenvalues to within 7.3% and 2.7%, respectively. The spatial amplification measured in the laboratory frame and the temporal instability inferred in the co-moving frame therefore quantify the same growth process.

The multi-trajectory inference achieves this agreement with remarkably little training data. The anti-symmetric and symmetric operators are trained on only 3 and 15 of the 198 available trajectories, respectively, selected through an even sweep across initial and final amplitudes and net amplification to sparsely span the observed seed dynamics. Nevertheless, the inferred operators predict both the amplification curves and the spatio-temporal structures of trajectories excluded from the fit (Fig. 3.6(a_3) and Fig. 3.6(b_3)). The learned operators therefore not only reproduce their training trajectories, but also generalize across trajectories that were *not* included in the training ensemble $\mathscr{J}$, demonstrating that the observed amplification is governed by a low-complexity linear mechanism.

The black dotted curves in Fig. 3.6(a_3) and Fig. 3.6(b_3) provide the final linearity confirmation: the corresponding nonlinear terms remain significantly smaller than the dominant linear dynamics throughout the Galilean trajectories. The quantitative agreement between laboratory- and Galilean-frame growth rates, the out-of-sample prediction of complete seed trajectories, and the sustained dominance of linear over nonlinear terms jointly identify the learned eigenspectra

as approximations of the underlying Galilean-frame stability operator. Both symmetry classes thus exhibit the same defining instability signature: a dominant, synchronous, exponentially growing real mode with nearly equal growth rate. This identifies temporal and spatial symmetry breaking as synchronous Floquet instabilities of the FHR, analogous to secondary instability, for the present nonlinear harmonic base state.

3.3.3 Agreement of operator prediction, STPOD modes and Floquet identity

A particularly striking result is the agreement between the learned operators and the independently obtained STPOD modes (Fig. 3.6(a_1) and Fig. 3.6(b_1)). When initialized with the Galilean-transformed initial seeds of the representative STPOD modes ϕ_1^s and ϕ_1^a, the learned operators $\mathbf{A}_r^s$ and $\mathbf{A}_r^a$ predict trajectories and spatio-temporal distributions that closely reproduce the corresponding STPOD modes.

This is highly remarkable for multiple reasons: The multi-trajectory operator inference is trained only on raw seed data and has no knowledge of the STPOD modes or their exact spatio-temporal structure. Conversely, STPOD assumes neither linear dynamics nor a least-squares fit to a propagator. The agreement of these independent methods in amplification and flow-structure evolution therefore provides a strong, non-trivial cross-validation of the central hypothesis that the leading time-periodic STPOD modes identify physical eigenmodes of the underlying linear stability operator, i.e. the active Floquet modes driving symmetry breaking of the FHR, in the identified region of interest.

The above still omits a subtle nuance: STPOD is a data-driven decomposition where the modes are optimized to represent ensemble space-time energy and are *not* individually constrained to satisfy either the NSE or their stability equations on a mode-by-mode basis. Governing-equation consistency is therefore *not* inherited merely because the modes or independently learned operators originate from DNS data.

This admits a more direct equation-level test (derivation in Appendix 3.8.2). For a Floquet

solution $\mathbf{q}'(t) = e^{\mu t}\varphi(t)$, with $\varphi(t+T) = \varphi(t)$, a mode should satisfy

$$\dot{\varphi}(t) - \big(\mathbf{A}(t) - \mu\mathbf{I}\big)\varphi(t) = \mathbf{r}_F(t), \tag{3.31}$$

where $\mathbf{r}_F(t) = \mathbf{0}$ for an exact Floquet mode. It is the LTP analogue of verifying an ordinary LTI eigenvector by substituting it back into $\mathbf{A}\mathbf{v} = \lambda\mathbf{v}$ (an actual eigenvector returns with exactly the evolution prescribed by its eigenvalue). Using the growth rate μ estimated independently from the Galilean-frame amplification, we evaluate this residual for the STPOD modes. It remains small for the leading symmetric modes ϕ_1^s and ϕ_2^s (Figs. 3.11a and 3.11b) and for the leading anti-symmetric mode ϕ_1^a (Fig. 3.12a), but is substantially larger for higher modes, including ϕ_3^s and ϕ_2^a (Figs. 3.11c and 3.12b).

The leading modes therefore satisfy a dynamical constraint that is not imposed by STPOD and is not satisfied by the remaining modes. Together, the two tests provide complementary evidence: the operator predictions reproduce their independently extracted spatio-temporal evolution, while the small Floquet residuals show that this evolution is consistent with the governing equations linearized about the FHR. This mode-selective agreement supports the identification of ϕ_1^s, ϕ_2^s, and ϕ_1^a as the active Floquet structures underlying the initial symmetry-breaking dynamics. The identified modes thus establish repelling directions of the FHR. Conversely, after periodic forcing is applied to the steady laminar boundary-layer initial condition, the flow rapidly approaches the FHR as initialization transients decay, which indicates attracting directions. Together, these observations support the saddle-type interpretation introduced in Sec. 3.1.

3.4 Temporal and spatial symmetry-breaking seed mechanics

We now describe the physical mechanisms, kinematics, and formation phenomena by which the symmetric and anti-symmetric instability seeds arise. We preface that no stochastic forcing or deliberate noise was imposed in this DNS. Small finite disturbances may nevertheless

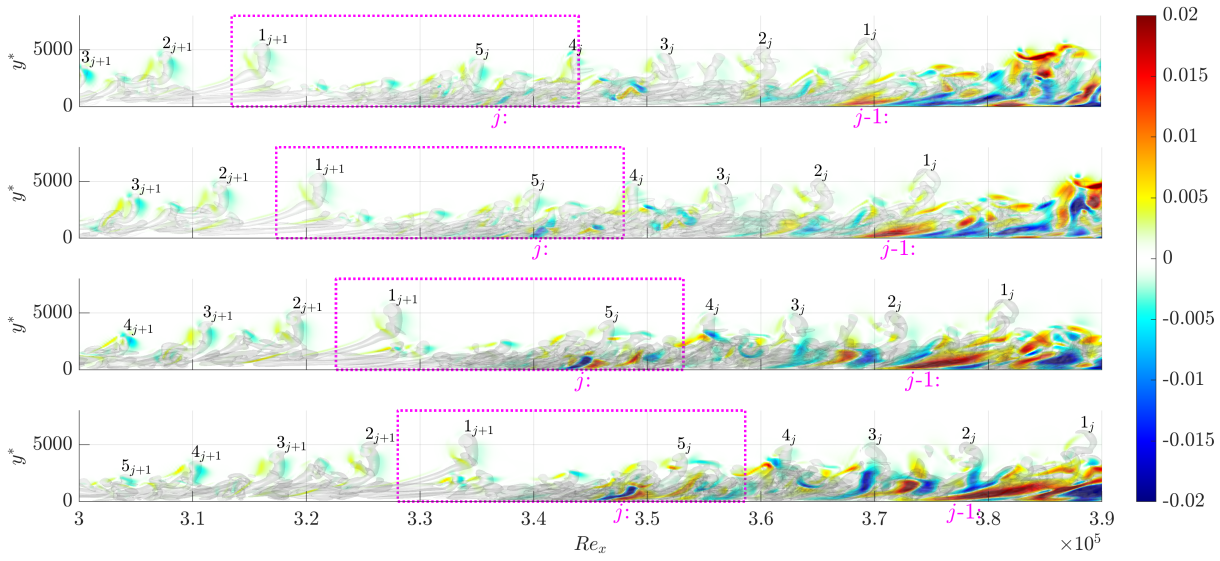


Figure 3.7. Formation process of the prototypical time-symmetry-breaking seed: symmetric ϕ_1^s mode shown by u-velocity contours on the centre plane $z^* = 0$ at four equidistant phases, in the context of Q-criterion isocontours ($Q = 10^3$) of the FHR. Labels indicate structures from three consecutive actuation periods/realizations ($j-1$, j, $j+1$): black labels enumerate Ω-like vortices formed from the evolved, lifted-up hairpin-vortex head, and magenta labels denote the corresponding near-wall disturbance "burst" which marks the seed emergence. The magenta box marks the travelling Moore neighbourhood used for Galilean tracking.

arise by imperfections of numerical nature (despite a structured grid) or by unavoidable upstream-propagating disturbances from downstream turbulence. These are plausible receptivity pathways for either symmetry breaking class. However, once a supplied disturbance projects onto an unstable symmetry breaking mode, its subsequent amplification becomes deterministic.

3.4.1 Temporal symmetry breaking physics: symmetric seed

The earliest time-periodicity-breaking departures from the FHR are dominated by the leading STPOD modes ϕ_1^s and ϕ_2^s. Their realization-dependent amplitudes vary slowly between forcing periods, while their intra-period geometry remains locally periodic (i.e., geometrically quasi-periodic (Lin and Schmidt, 2026)). Figure 3.7 follows the formation of the prototypical seed ϕ_1^s (while ϕ_2^s is topologically very similar and available in the Appendix in Fig. 3.10). Phenomenologically, the spatio-temporal behavior of this mode exhibits two physical processes: initial disturbance receptivity, and near-wall seed formation and amplification. Each developing

Ω/ring-like vortex head is flanked by weak positive and negative streamwise-velocity fluctuations. This dipolar signature is consistent with small local modulations of the periodic vortex structure and identifies the vortex-head-formation process as a receptive location for weak disturbances. From each head, the disturbance signature extends towards the wall along and between the hairpin legs, consistent with induction and the associated high-shear environment guiding the perturbation into the near-wall region.

Importantly, the disturbances visible near the vortex heads do not amplify there. Their principal growth, and hence the emergence of the seed, occurs close to the wall, where wall-normal variations in convection speed have spread the disturbances in the streamwise direction and brought contributions delivered during successive forcing periods into the same near-wall interaction region. Fig. 3.7 shows that this near-wall amplification initiates over the narrow window $3.4 \times 10^5 \lesssim Re_x \lesssim 3.5 \times 10^5$, after several vortex heads have passed through the region.

This process can therefore be understood as an inter-period disturbance interaction: disturbances associated with different realizations $j-1$, j and $j+1$ are delivered into the same near-wall region, where they overlap spatially and amplify within the unstable mode. At the onset of the seed amplification in the fourth panel of Fig. 3.7, the first vortex head of the next realization $j+1$ has already entered the amplification region associated with the current realization j. This mechanism is also depicted in the phase-resolved and space–time diagnostics in Fig. 3.5(a) and Fig. 3.5(b). Farther downstream, the earlier heads of realization j similarly catch up with the more slowly moving already-amplified near-wall structure produced during $j-1$. The resulting disturbance field ultimately organizes into a localized, amplified near-wall burst that takes the form of the time-symmetry-breaking seed and constitutes the physical expression of temporal symmetry breaking.

This sequence closely parallels the randomization phenomenology reported by Bake et al. (2002): ring-vortex formation provides a receptive environment for small disturbances; the outer vortices influence the near-wall flow through induction and wall-pressure gradients; and the resulting perturbations amplify within the strong near-wall velocity gradients, as interactions

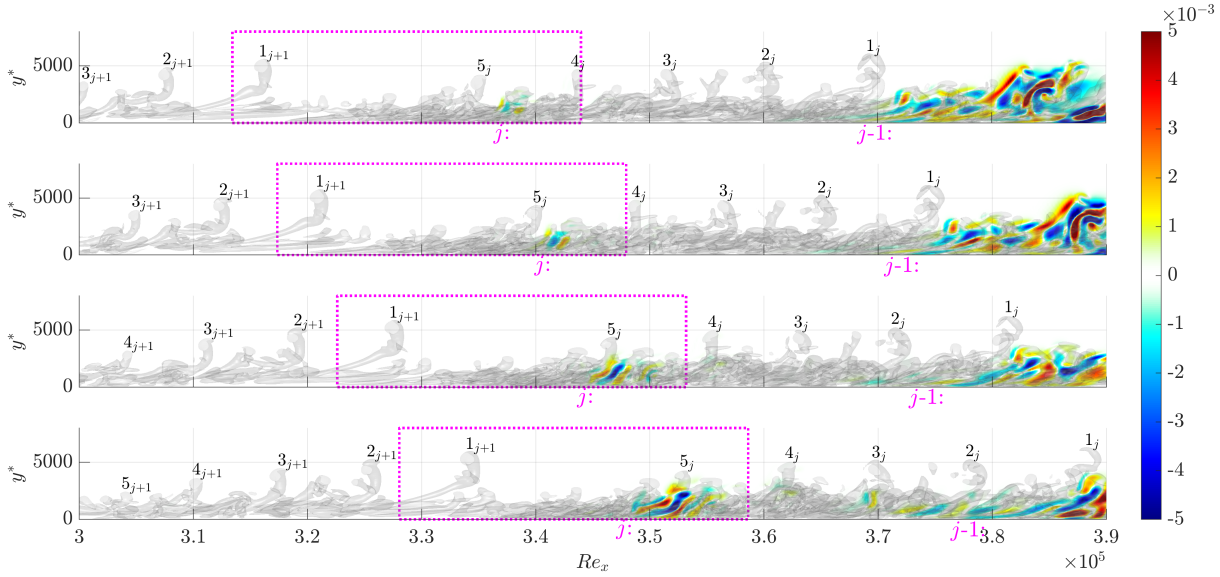


Figure 3.8. Formation process of the prototypical spatial symmetry breaking seed: anti-symmetric ϕ_1^a mode visualized with w-velocity contours of the center plane $z^* = 0$ at four equidistant phases, in the context of Q-criterion isocontours ($Q = 10^3$) of the FHR. Labels and annotations follow the same convention as in Fig. 3.7.

between structures generated during successive periods provide a continuous supply of this cycle. The present STPOD and Floquet analyses isolate the organized, reproducible stage of this process: once a supplied disturbance projects onto the unstable symmetric mode, its development into the wall-burst seed structure is coherent and deterministic, preceding the fully aperiodic and chaotic flow farther downstream.

3.4.2 Spatial symmetry breaking physics: anti-symmetric seed

The leading anti-symmetric seed ϕ_1^a is most directly revealed by a non-zero spanwise velocity on the symmetry plane. At $z = 0$, the full symmetric and anti-symmetric states satisfy

$$\boldsymbol{q}^S(x,y,0,t) = \left[u^S,\ v^S,\ 0,\ p^S\right]^\top, \qquad \boldsymbol{q}^A(x,y,0,t) = \left[0,\ 0,\ w^A,\ 0\right]^\top. \tag{3.32}$$

Hence any $w(x,y,0,t) = w^A(x,y,0,t) \neq 0$ represents motion across the symmetry plane and is a direct local signature of the anti-symmetric component becoming active, i.e., of instantaneous

spatial symmetry breaking (Fig. 3.8).

The flow fields show no analogous hairpin-head precursor for the anti-symmetric seed. The inability to reproduce the same midplane signature is kinematically enforced by parity: u^A and v^A are odd in z, whereas w^A is even; correspondingly, ω_x^A and ω_y^A are even, while ω_z^A is odd. Consequently, $\omega_z^A = 0$ on the symmetry plane and ϕ_1^a cannot contain the same midplane spanwise-vorticity disturbance that accompanies the hairpin-head receptivity of the symmetric seed. This difference is particularly evident in the phase-resolved and space–time diagnostics of Fig. 3.5(a) and Fig. 3.5(b). In the symmetric component, the disturbances associated with successive hairpin heads produce distinct, countable amplitude peaks and corresponding streaks in the space–time contours. No comparable hairpin-head-associated signature can be identified in either anti-symmetric diagnostic. Nevertheless, the anti-symmetric seed appears directly within the same spatial region as the symmetric seed, after which both structures evolve in synchrony along the same dominant space–time band until they approach nonlinear saturation. The two instability seeds therefore share the same amplification region and timing, despite their different mode shapes and receptivity pathways.

Since no anti-symmetric disturbance is deliberately imposed in the DNS, we hypothesize that its initial receptivity originates in small but finite mesh asymmetries or other numerical imperfections. This would not diminish the physical significance of the instability: the present DNS already represents an exceptionally low-disturbance environment, yet, apparently weak numerical disturbances are sufficient to activate the unstable anti-symmetric subspace. The larger unavoidable asymmetries of experimental and natural environments would therefore be expected to excite the same instability at least as readily. Other plausible sources include upstream-propagating pressure disturbances generated by the downstream symmetry-broken turbulence. Generally, pressure-mediated near-wall receptivity is consistent with the K-type randomization mechanism described by Bake et al. (2002), in which vortex-induced wall-parallel pressure gradients modify the production of vorticity at the wall. Irrespective of the receptivity or origin, once a disturbance projects onto ϕ_1^a, its subsequent growth follows the deterministic

anti-symmetric instability established in Sec. 3.3.

3.5 Discussion: Nonlinear symmetry breaking feedback on harmonic solutions

3.5.1 Impact on the skin friction curve and C_f-maximum

We show in the following that the nonlinear feedback from symmetry-breaking fluctuations is required to close the FHR wall-friction budget near the C_f-maximum. It enters the FHR equation through the quadratic correlations on the right-hand side of Eq. (3.11). These terms form the divergence of a phase-averaged, time-periodic velocity covariance in the incompressible equations. We therefore refer to the covariance as the symmetry breaking residual-stress and to the resulting term $\tilde{\mathscr{R}}^s$ as its divergence.

Let $\langle\cdot\rangle_{T,z}$ denote averaging over one FHR period and the spanwise domain. Time-periodicity of the FHR gives $\langle\partial_t\tilde{u}\rangle_{T,z}=0$. We rearrange and apply $\langle\cdot\rangle_{T,z}$ to the streamwise component of Eq. (3.11),

$$-\nu\left\langle\frac{\partial^2\tilde{u}}{\partial x_j^2}\right\rangle_{T,z}=-\left\langle\tilde{u}_j\frac{\partial\tilde{u}}{\partial x_j}\right\rangle_{T,z}-\left\langle\frac{\partial\tilde{p}}{\partial x}\right\rangle_{T,z}+\langle\tilde{\mathscr{R}}^s_x\rangle_{T,z}. \tag{3.33}$$

Further wall-normal integration to height H and normalization by $U_\infty^2/2$ yields

$$\begin{aligned}C_\nu(H)&\equiv-\frac{2\nu}{U_\infty^2}\int_0^H\left\langle\frac{\partial^2\tilde{u}}{\partial x_j^2}\right\rangle_{T,z}\mathrm{d}y\\&=\underbrace{-\frac{2}{U_\infty^2}\int_0^H\left\langle\tilde{u}_j\frac{\partial\tilde{u}}{\partial x_j}\right\rangle_{T,z}\mathrm{d}y}_{C_{\mathrm{adv}}(H)}+\underbrace{-\frac{2}{U_\infty^2}\int_0^H\left\langle\frac{\partial\tilde{p}}{\partial x}\right\rangle_{T,z}\mathrm{d}y}_{C_p(H)}+\underbrace{\frac{2}{U_\infty^2}\int_0^H\langle\tilde{\mathscr{R}}^s_x\rangle_{T,z}\mathrm{d}y}_{C_R(H)}.\end{aligned} \tag{3.34}$$

The period and spanwise averages and subsequent wall-normal integration are all linear operations. The resulting relation is therefore the same streamwise momentum balance projected onto a scalar wall-stress budget, without additional modeling assumptions.

Writing the time- and spanwise-averaged streamwise velocity as $U(x,y) \equiv \langle \tilde{u} \rangle_{T,z}$, spanwise periodicity and the no-slip condition give the once-integrated viscous identity (Ricco and Skote, 2022)

$$\begin{aligned} C_\nu(H) &= -\frac{2\nu}{U_\infty^2}\left[\frac{\partial^2}{\partial x^2}\int_0^H U\,\mathrm{d}y + \left.\frac{\partial U}{\partial y}\right|_{y=H} - \left.\frac{\partial U}{\partial y}\right|_{y=0}\right] \\ &= \underbrace{\frac{2\nu}{U_\infty^2}\left.\frac{\partial U}{\partial y}\right|_{y=0}}_{C_f} - \frac{2\nu}{U_\infty^2}\left[\left.\frac{\partial U}{\partial y}\right|_{y=H} + \frac{\partial^2}{\partial x^2}\int_0^H U\,\mathrm{d}y\right] \simeq C_f, \end{aligned} \tag{3.35}$$

Here H is the fixed upper boundary of the sampled domain, which lies in the uniform free stream. The resulting collapse of C_ν onto the directly evaluated C_f-curve (Fig. 3.9) computationally confirms that both the upper-boundary shear and streamwise-diffusion corrections are negligible, as expected for a sufficiently high domain and a boundary layer flow, where $\mathscr{O}(\delta^2/x^2) \ll 1$.

These operations yield a very practical budget for the wall stress

$$C_f \simeq C_\nu = C_{\mathrm{adv}} + C_p + C_R\,, \tag{3.36}$$

which is therefore effectively a "C_f-budget": it partitions how different physical terms affect the C_f-curve. As shown in Fig. 3.9, the unclosed FHR terms $C_{\mathrm{adv}} + C_p$ significantly overpredict the wall stress through the turnover region. The integrated residual contribution C_R is negative and supplies the missing correction, bringing the closed reconstruction into near coincidence with both C_ν and C_f, while leaving a negligibly small balance defect $\varepsilon_{\mathrm{bal}} \equiv C_{\mathrm{adv}} + C_p + C_R - C_\nu \simeq 0$ associated with numerical processing inaccuracies.

The direct evaluation of C_R from the quadratic $\mathbf{u}^s$ and $\mathbf{u}^a$ fluctuation correlations makes this an a posteriori closure test. Near the turnover/C_f-max, wall-normal integration and cancellation between the larger FHR terms make the signed contribution of $\tilde{\mathscr{R}}^s$ consequential despite its small vector norm in the earlier linear-growth window.

These results have the following implication: The present DNS-computed empirical FHR

reproduces the "correct" literature-validated C_f curve. However, it cannot *by itself* satisfy the momentum balance required for it, i.e., the corresponding unclosed form of (3.11) obtained by setting $\tilde{\mathscr{R}}^s = 0$. The nonlinear symmetry breaking residual-stress feedback $\tilde{\mathscr{R}}^s$ was required to *close* the FHR wall-friction budget that obtained the correct C_f. Its strongest negative contribution occurs near $C_f^{\max}$, identifying a direct wall-stress-opposing feedback associated predominantly with time-symmetry breaking.

The cyan-dashed curve $C_{\text{adv}} + C_p$ in Fig. 3.9 is a diagnostic formed by removing C_R while holding the present FHR fixed. It is not the C_f curve of a separately computed hypothetical unclosed harmonic solution; without the residual feedback, that solution and its other budget terms would generally change. Nevertheless, the negative C_R measured through the turnover region suggests that symmetry-breaking fluctuations help suppress the C_f overshoot. A harmonic solution that omits this feedback may therefore overpredict the wall stress near the C_f overshoot in currently unknown ways, even when spectrally converged. We hypothesize that this missing feedback may help explain the difficulties that recent harmonic Navier–Stokes methods (Rigas et al., 2021; Sleeman et al., 2026) have encountered in continuing downstream to capture the full C_f maximum. This connection remains hypothetical, however, and testing it requires direct comparison with an unclosed harmonic solution. Such a *true* limit cycle (as opposed to the *empirical* FHR base state used here) may be obtained by stabilizing the unstable symmetry-breaking directions a priori (e.g. Frantz et al. (2023)).

3.5.2 Implications for harmonic Navier–Stokes methods

Frequency-domain Navier–Stokes methods resolve nonlinear wave interactions using discrete temporal components. Recent harmonic-balance Navier–Stokes (HBNS) calculations have captured resonant growth, early vortex formation and interaction with finite harmonic sets (Rigas et al., 2021; Savarino et al., 2025), while recent nonlinear one-way Navier–Stokes (NOWNS) calculations have marched coupled frequency components downstream (Sleeman et al., 2026) beyond the laminar regime. Yet the presented harmonic solutions reach only

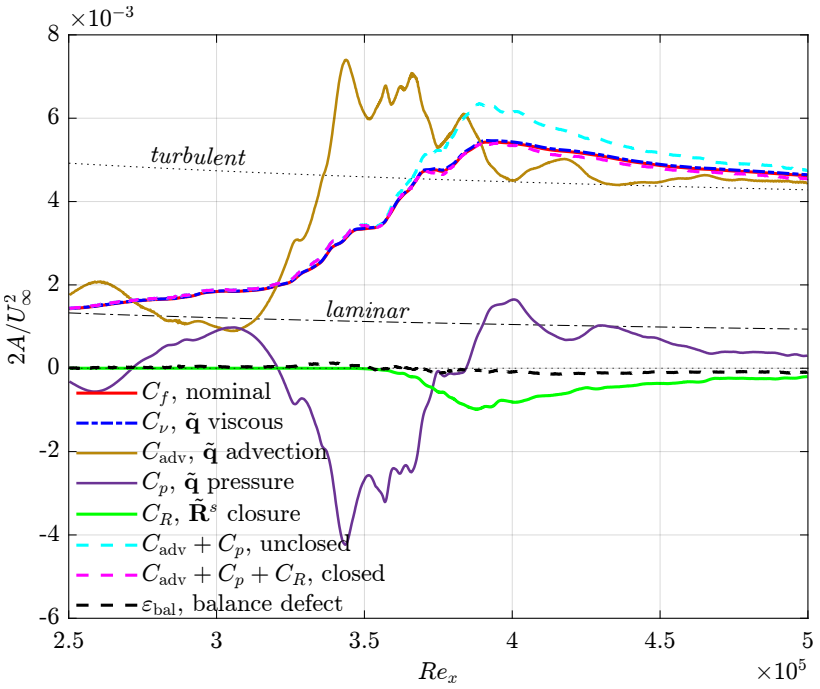


Figure 3.9. C_f budget for the DNS-conditioned FHR. The FHR advection and pressure-gradient contributions form the unclosed balance. The residual-stress divergence is evaluated independently from quadratic correlations of the symmetry-breaking fluctuations, and its period- and spanwise-averaged, wall-normal-integrated contribution C_R supplies the negative correction that closes the wall-stress budget.

the initial C_f rise; neither proceeds through a complete C_f maximum into the downstream relaxation. That apparent limitation is consistent with (but does not establish) the hypothesis above that missing symmetry breaking feedback may permit excessive wall-stress growth. The collective evidence raises a nuanced question: what is missing from harmonic descriptions near the C_f-maximum?

Two distinct limitations must be separated. The first is finite-harmonic inefficiency: the highly localized vortex structures of the FHR converge slowly in a Fourier expansion. Lin and Schmidt (2024) showed that even relatively high-order harmonic superpositions retain spurious oscillations that disappear only when nearly all available harmonics are included. This is an ordinary Fourier-truncation problem that can, in principle, be reduced by increasing the number of retained harmonics. The second limitation remains even if every integer harmonic of the periodic FHR is retained: those harmonics do not determine the covariance of the symmetry-breaking fluctuations. That covariance is separate second-order information and cannot be recovered by increasing the number of harmonics. We show in the following that it is a statistical closure problem.

Data-driven closure has already been proposed for finite-harmonic inefficiency by modeling the effect of omitted higher integer harmonics in frequency-truncated HBNS equations (Rigas and Schmid, 2022). The closure diagnosed here is different in nature. It arises from fluctuations outside the periodic solution and therefore remains absent even when that solution is spectrally converged.

To show this distinction, we expand the FHR and its time-periodic residual-stress divergence in Fourier series,

$$\tilde{\boldsymbol{q}}(\boldsymbol{x},t) = \sum_{n\in\mathbb{Z}} \hat{\boldsymbol{q}}_n(\boldsymbol{x}) e^{in\omega_1 t}, \qquad \tilde{\mathscr{R}}^s(\boldsymbol{x},t) = \sum_{n\in\mathbb{Z}} \widehat{\mathscr{R}}^s_n(\boldsymbol{x}) e^{in\omega_1 t}. \tag{3.37}$$

Transforming Eq. (3.11) into the frequency domain gives the momentum balance for the n-th

harmonic,

$$in\omega_1\hat{u}_{i,n} + \sum_{m\in\mathbb{Z}} \hat{u}_{j,m}\frac{\partial \hat{u}_{i,n-m}}{\partial x_j} + \frac{\partial \hat{p}_n}{\partial x_i} - \nu\frac{\partial^2 \hat{u}_{i,n}}{\partial x_j^2} = \widehat{\mathscr{R}}^s_{i,n}, \qquad \frac{\partial \hat{u}_{i,n}}{\partial x_i} = 0. \tag{3.38}$$

A harmonic method such as HBNS retains a finite set $n \in \{-N,\ldots,N\}$ and evaluates the nonlinear interactions among those harmonics. Increasing N improves the spectral convergence, but it does not determine the right-hand side of Eq. (3.38), which is dependent on fluctuations outside the FHR and its time-periodic phase-locked state.

We visualize this distinction as a simplified schematic on the continuous frequency axis:

$$\begin{aligned}
\omega = \omega_1 \quad &: \quad \hat{\boldsymbol{u}}_1 \longleftarrow \widehat{\mathscr{R}}^s_1 && \text{periodic fundamental} \\
0 < \omega < \omega_1 \quad &: \quad \hat{\boldsymbol{u}}^{s/a}(\omega) \nearrow\!\searrow && \text{broadband fluctuations} \\
\omega = 0 \quad &: \quad \hat{\boldsymbol{u}}_0 \longleftarrow \widehat{\mathscr{R}}^s_0 && \text{mean-flow deformation} \rightarrow C_f\text{-curve} \\
-\omega_1 < \omega < 0 \quad &: \quad \hat{\boldsymbol{u}}^{s/a}(\omega) \nearrow\!\searrow && \text{broadband fluctuations} \\
\omega = -\omega_1 \quad &: \quad \hat{\boldsymbol{u}}_{-1} \longleftarrow \widehat{\mathscr{R}}^s_{-1} && \text{conjugate fundamental.}
\end{aligned} \tag{3.39}$$

Analogous broadband intervals lie between every pair of adjacent higher harmonics. HBNS solves only for states at the discrete frequencies $\omega = n\omega_1$, whereas the residual at each harmonic receives contributions from all broadband frequency pairs whose frequencies sum to $n\omega_1$. Denoting the continuous Fourier transforms of the symmetry-breaking fluctuations by $\hat{u}_i^{s/a}(\omega)$ and the phase average over periods by $\langle\cdot\rangle$, the residual Fourier coefficient required on the right-hand side of Eq. (3.38) is given by the convolution

$$\widehat{\mathscr{R}}^s_{i,n} = -\frac{\partial}{\partial x_j}\int_{-\infty}^{\infty} \left\langle \hat{u}_i^s(\omega)\hat{u}_j^s(n\omega_1-\omega) + \hat{u}_i^a(\omega)\hat{u}_j^a(n\omega_1-\omega)\right\rangle \frac{\mathrm{d}\omega}{2\pi} \tag{3.40}$$

for any harmonic component $n \in \mathbb{Z}$.

The important observation is that for $n = 0$, every fluctuation pair ω and $-\omega$, broadband and harmonic alike, contributes to $\widehat{\mathscr{R}}^s_0$, which directly modifies the mean-flow deformation and

hence the skin-friction C_f-curve. For $n \neq 0$, every broadband or harmonic frequency triad whose frequencies sum to $n\omega_1$ contributes to the periodic feedback at that harmonic.

This yields the key conclusion: although $\tilde{\mathscr{R}}^s(t)$ is time-periodic and can be expanded at the same harmonic frequencies as the FHR, its Fourier coefficients *cannot* be determined from the harmonics of the FHR. Its periodicity follows by construction from the cyclostationarity of the signal because the underlying phase-averaged fluctuation covariance repeats with the forcing period, even though the individual fluctuations need not be periodic and may be broadband (Gardner et al., 2006). Importantly, the FHR contains only the first moment, whereas $\tilde{\mathscr{R}}^s$ depends on a second moment. The former does not determine the latter, thereby making this a statistical closure problem.

The appropriate extension is not to abandon harmonic methods, but to close them. We recommend future harmonic-type methods for canonical transition to augment each integer-harmonic equation with the symmetry-breaking residual-stress coefficient $\widehat{\mathscr{R}}^s_n$ identified here. These coefficients may be supplied empirically from DNS, predicted via coupled broadband fluctuation equations, or approximated by a reduced model of the phase-averaged fluctuation covariance. The present result constitutes an *a posteriori* closure calculation rather than a predictive model, but it identifies exactly what a model must provide: $\widehat{\mathscr{R}}^s_{n=0}$ to close the mean-flow deformation and skin-friction balance, and $\widehat{\mathscr{R}}^s_{n\neq 0}$ to close the periodic harmonic feedback. Such a hybrid formulation would retain the efficiency and interpretability of harmonic analysis while incorporating nonlinear feedback from temporal and spatial symmetry breaking, which is fundamental to laminar–turbulent transition.

3.6 Conclusions

This work shows why temporal and spatial symmetry breaking is inevitable and required in canonical laminar–turbulent transition: it is the linear instability by which the flow escapes its deterministic harmonic response and, at finite amplitude, provides the nonlinear feedback needed

to close that response's momentum/wall-stress balance. Periodic TS-wave actuation generates a fully nonlinear, harmonically saturated Fundamental Harmonic Response (FHR) containing Λ-vortices, hairpin packets and their downstream development, yet this state remains spatially compact, time-periodic and spanwise symmetric. Its spatial compactness visibly marks the finite streamwise reach of the deterministic harmonic regime, beyond which transition necessarily proceeds via symmetry-broken dynamics. The first departures appear as localized near-wall "seeds" around the spanwise symmetry plane, embedded within the developed and saturated FHR structure. We identify these seeds as unstable symmetric and anti-symmetric structures of the FHR-linearized dynamics. A flow confined to the periodic FHR cannot develop the broadband non-periodicity of turbulence; temporal symmetry breaking is therefore a required step in transition. In the present canonical K-type simulation, the flow additionally leaves the reflection-symmetric subspace through a synchronous anti-symmetric instability. Symmetry breaking is thus not a late symptom of nonlinear breakdown, but the linear-time-periodic Floquet instability by which the flow escapes its deterministic harmonic state.

We establish a data-driven Floquet analysis through a chain of computational methods, accompanied by mathematical disambiguation and independent tests. Starting from the exact symmetry-decomposed Navier–Stokes equations (Lin and Schmidt, 2026), we show that, at first order, the symmetric and anti-symmetric fluctuations are governed by the same FHR-linearized linear-time-periodic (LTP) operator, while each fluctuation remains within its own symmetry subspace. Direct comparisons of the equation terms show that the FHR residual and symmetry-specific nonlinear contributions remain negligible relative to the first-order dynamics over the relevant growth windows, i.e., the first symmetry-breaking seeds are naturally already in a linear perturbation regime within the DNS. Tracking their trajectories in a frame moving with the FHR renders the local base state quasi-steady and enables the inference of autonomous Galilean-frame stability operators. Separate regressions within the two invariant symmetry subspaces yield reduced, symmetry-restricted representations of the common FHR-linearized dynamics, and each is dominated by a real unstable mode with nearly the same growth rate. These rates agree

with independently measured laboratory-frame spatial amplifications to within 7.3% and 2.7% for the symmetric and anti-symmetric components, respectively, while the inferred operators also generalize to complete trajectories that were excluded from training. Furthermore, their predictions reproduce the independently obtained dominant STPOD structures, and mode-wise Floquet-residual tests show that ϕ_1^s, ϕ_2^s and ϕ_1^a satisfy the FHR-linearized governing equations substantially better than the higher modes. The resulting confidence in the data-driven stability analysis thus comes from clearly separating what mathematical formulation is exact, when an approximation truly applies and what is independently verified: the symmetry-decomposed NSE define the common linear dynamics, measured equation terms establish the linear regime, and growth-rate, trajectory and Floquet-residual tests cross-validate the inferred instability.

We further connect these Floquet instabilities directly to the physical formation of the first symmetry-breaking seeds. The leading symmetric seed begins with weak disturbances around developing hairpin-vortex heads. Induction and the high-shear environment along and between the hairpin legs transport these disturbances towards the wall, where wall-normal variations in convection speed spread them streamwise and bring contributions delivered during successive forcing periods into spatial overlap. Their amplification within the unstable symmetric mode produces a localized near-wall burst that remains coherent and synchronous with the FHR while varying in amplitude between realizations, thereby breaking time-periodicity. The anti-symmetric seed follows a different receptivity pathway. Reflection symmetry forces its spanwise-vorticity component to vanish on the symmetry plane, so it cannot contain the analogous hairpin-head precursor; its activation is instead revealed directly by non-zero spanwise velocity across that plane. The symmetric and anti-symmetric seeds nevertheless emerge in the same streamwise region and amplify in synchrony until nonlinear saturation. In the exceptionally low-disturbance environment of the present DNS the most plausible triggers of the anti-symmetric mode are weak numerical asymmetries or upstream traveling disturbances from downstream turbulence, thus, the larger unavoidable asymmetries of experimental and natural environments should excite the same unstable subspace at least as readily. Irrespective of receptivity pathways, once a disturbance is

supplied and projects onto an unstable mode, the resulting seed amplification is coherent and deterministic.

Crucially, we show that finite-amplitude symmetry breaking feeds back on the FHR, and is required to close its wall-stress balance. From the streamwise momentum equation, we derive a wall-friction budget in which the phase-averaged quadratic fluctuation covariance produces a symmetry breaking residual-stress divergence $\tilde{\mathscr{R}}$. Its integrated contribution C_R supplies the negative correction required to close the DNS-computed FHR budget near the C_f maximum. The strongest contribution opposes the FHR wall stress through the turnover region and suggests that the feedback, associated predominantly with temporal symmetry breaking, helps suppress the C_f overshoot. Symmetry breaking therefore does more than populate the broadband spectrum: its finite-amplitude covariance modifies the mean-flow deformation and the skin-friction curve at the most critical point. Including more integer harmonics may converge the Fourier representation of the harmonic solution, but cannot determine the required symmetry breaking residual-stress. The FHR provides the first moment, whereas the closure depends on a phase-averaged second moment: the residual is itself periodic and harmonically representable, but its coefficients depend on correlations of broadband fluctuations outside the FHR. A spectrally converged harmonic solution would therefore still miss the broadband symmetry breaking closure that shapes the momentum balance and skin friction. This result exposes a fundamental limitation of purely harmonic Navier Stokes methods for transition: They suffer from a statistical closure problem that only time-symmetry breaking can alleviate.

Together, these results establish a two-stage mechanism of symmetry breaking in deterministic transition:

(i) *Seed formation and linear amplification:* Linear Floquet instability of the nonlinear FHR creates organized temporal and spatial symmetry-breaking seeds that amplify.

(ii) *Finite-amplitude nonlinear feedback:* Once these fluctuations reach finite amplitude, their quadratic correlations supply the residual-stress feedback required to restore the FHR

wall-stress balance as the flow progresses towards broadband turbulence.

An adequate reduced description of complete canonical transition should therefore contain the finite-amplitude nonlinear harmonic response, its unstable symmetry-breaking directions and the residual-stress feedback generated by those directions. These findings suggest a concrete extension of harmonic methods that retains their efficiency and interpretability: close each integer-harmonic equation with the corresponding symmetry breaking residual-stress coefficients. The present calculation readily provides these coefficients *a posteriori*, while a predictive formulation could obtain them from coupled broadband fluctuation equations or a reduced model of the phase-averaged covariance. A complementary study could be to *a priori* stabilize the unstable symmetry-breaking directions and compute the corresponding unclosed periodic solution, thereby isolating the effect of this feedback on the C_f maximum. More broadly, the present framework shows how symmetry breaking in the Navier–Stokes equations arises from the instability of a fully deterministic, symmetric and harmonic state at finite amplitude and how the resulting symmetry-breaking structures feed back nonlinearly on that state, once *those* reach finite amplitude. Symmetry breaking is therefore fundamental to canonical laminar–turbulent transition: it supplies both the linear route out of the deterministic harmonic regime and the nonlinear feedback required to complete the transition towards turbulence.

3.7 Acknowledgements

We gratefully acknowledge support from the National Science Foundation under Award no. 2046311.

3.8 Appendix

3.8.1 Exact semi-discrete descriptor systems.

After spatial discretization, we collect velocity and pressure into $\mathbf{q}^{s/a} = [\mathbf{u}^{s/a}, \mathbf{p}^{s/a}]^\top$. The symmetric and anti-symmetric perturbations are governed by the same LTP operator $\mathbf{A}(t)$,

but retain their respective exact forcing contributions:

$$\underbrace{\begin{bmatrix} I & 0 \\ 0 & 0 \end{bmatrix}}_{\mathbf{M}} \frac{d}{dt} \begin{bmatrix} \mathbf{u}^s \\ \mathbf{p}^s \end{bmatrix} = \underbrace{\begin{bmatrix} -\mathbf{C}(\tilde{\mathbf{u}}(t)) + \nu\mathbf{L} & -\mathbf{G} \\ \mathbf{D} & 0 \end{bmatrix}}_{\mathbf{A}(t)\text{ Linear Time-Periodic NSE operator}} \begin{bmatrix} \mathbf{u}^s \\ \mathbf{p}^s \end{bmatrix} + \underbrace{\begin{bmatrix} \mathbf{N}^s \\ 0 \end{bmatrix}}_{\text{small}} + \underbrace{\begin{bmatrix} -\tilde{\mathbf{R}}^s \\ 0 \end{bmatrix}}_{\text{small}}. \tag{3.41}$$

$$\underbrace{\begin{bmatrix} I & 0 \\ 0 & 0 \end{bmatrix}}_{\mathbf{M}} \frac{d}{dt} \begin{bmatrix} \mathbf{u}^a \\ \mathbf{p}^a \end{bmatrix} = \underbrace{\begin{bmatrix} -\mathbf{C}(\tilde{\mathbf{u}}(t)) + \nu\mathbf{L} & -\mathbf{G} \\ \mathbf{D} & 0 \end{bmatrix}}_{\mathbf{A}(t)\text{ Linear Time-Periodic NSE operator}} \begin{bmatrix} \mathbf{u}^a \\ \mathbf{p}^a \end{bmatrix} + \underbrace{\begin{bmatrix} \mathbf{N}^a \\ 0 \end{bmatrix}}_{\text{small}}. \tag{3.42}$$

The combined discrete convection operator represents advection by the FHR and deformation by its velocity gradients. Its action on a discrete perturbation velocity is

$$[\mathbf{C}(\tilde{\mathbf{u}}(t))\mathbf{u}]_i = \sum_j \left[\operatorname{diag}(\tilde{\mathbf{u}}_j(t))\,\mathbf{D}_j\mathbf{u}_i + \operatorname{diag}(\mathbf{D}_j\tilde{\mathbf{u}}_i(t))\,\mathbf{u}_j\right],$$

which convectively couples FHR and fluctuation components across $i, j = \{1,2,3\}$. The remaining assembled operators are defined by

$$\mathbf{D} = \begin{bmatrix} \mathbf{D}_x & \mathbf{D}_y & \mathbf{D}_z \end{bmatrix}, \qquad \mathbf{G} = \begin{bmatrix} \mathbf{D}_x \\ \mathbf{D}_y \\ \mathbf{D}_z \end{bmatrix},$$

$$\mathbf{L} = \operatorname{diag}(\mathbf{L}_\Delta, \mathbf{L}_\Delta, \mathbf{L}_\Delta), \qquad \mathbf{L}_\Delta = \mathbf{D}_{xx} + \mathbf{D}_{yy} + \mathbf{D}_{zz}.$$

Here $\mathbf{D}$ and $\mathbf{G}$ are the discrete divergence and (pressure-) gradient maps, and $\mathbf{L}$ is the block-diagonal vector Laplacian. The singular mass matrix $\mathbf{M}$ characterizes the system as a descriptor system; incompressibility is imposed by the algebraic row $\mathbf{D}\mathbf{u}^{s/a} = 0$.

3.8.2 Floquet Theory and Identities

Theorem Consider the linear-time periodic system $\dot{\mathbf{x}} = \mathbf{A}(t)\mathbf{x}$ with period T such that $\mathbf{A}(t+T) = \mathbf{A}(t)$. Let μ be a Floquet exponent and ρ be the characteristic multiplier such that $\rho = e^{\mu T}$. Then, a solution $\mathbf{x}(t)$ exists such that:

i. $\mathbf{x}(t+T) = \rho\mathbf{x}(t)$

ii. $\mathbf{x}(t) = e^{\mu t}\varphi(t)$, where $\varphi(t)$ is a periodic Floquet mode with period T. Thus, re-inserting the Floquet ansatz into the system

$$\dot{\mathbf{x}} = \mathbf{A}(t)\mathbf{x} = \mathbf{A}(t)\varphi(t)e^{\mu t}$$

and differentiating the left-hand side

$$\frac{\mathrm{d}}{\mathrm{d}t}(e^{\mu t}\varphi(t)) = \mu e^{\mu t}\varphi(t) + e^{\mu t}\dot{\varphi}(t)$$

leads to

$$(\mu\varphi(t) + \dot{\varphi}(t))e^{\mu t} = \mathbf{A}(t)\varphi(t)e^{\mu t}.$$

Canceling $e^{\mu t}$ and isolating the time-derivative $\dot{\varphi}(t)$ produces a fundamental identity for the Floquet mode

$$\dot{\varphi}(t) = \big(\mathbf{A}(t) - \mu I\big)\varphi(t)$$

which shows how its periodic dynamics is governed by the system $\mathbf{A}(t)$ and its Floquet exponent μ.

Fig. 3.11a and Fig. 3.12a demonstrate that the leading STPOD modes (ϕ_1^s, ϕ_2^s and ϕ_1^a) satisfy the Floquet equation/identity eq. 3.31, which suggests that these STPOD modes identify Floquet modes here.

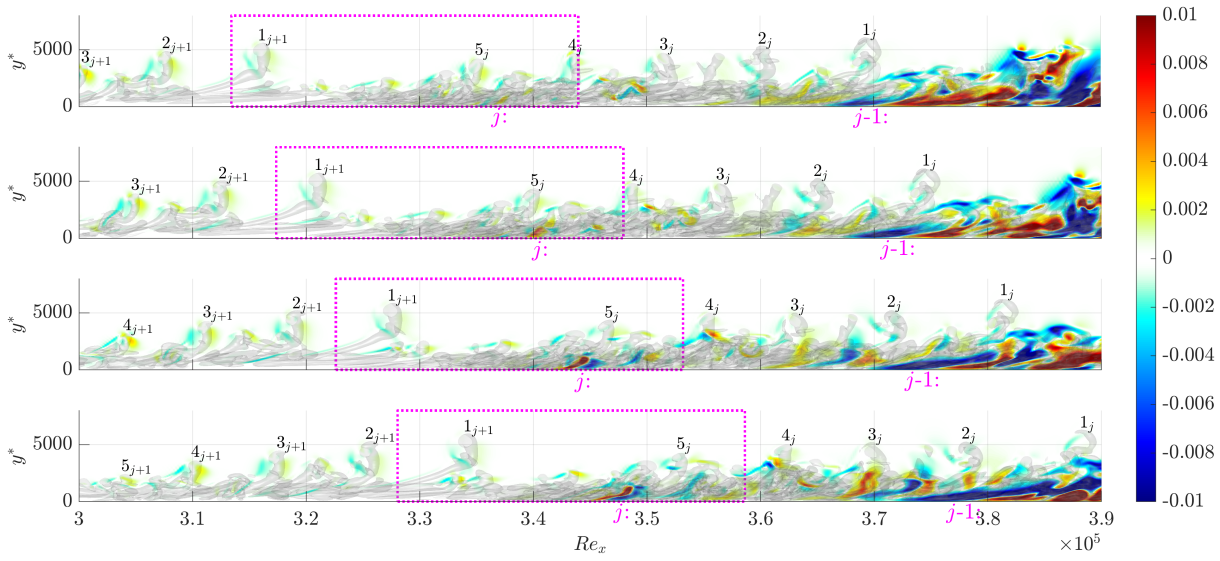


Figure 3.10. Formation process of the prototypical time-symmetry-breaking seed: symmetric ϕ_2^s mode shown by u-velocity contours on the centre plane $z^* = 0$ at four equidistant phases, in the context of Q-criterion isocontours ($Q = 10^3$) of the FHR. Labels and annotations follow the same convention as in Fig. 3.7.

3.8.3 Methods

Space-Time Proper Orthogonal Decomposition (STPOD)

The space and finite-time POD problem, first formulated by Lumley (1970) and recently computed by Schmidt and Schmid (2019) with a conditional formulation for finite events of interest, can be solved via the following Fredholm eigenvalue problem

$$\int_{\Delta T}\int_{V} E\{\mathbf{q}(\mathbf{x},t)\mathbf{q}^*(\mathbf{x}',t')\}\boldsymbol{W}(\mathbf{x})\phi(\mathbf{x},t)\,d\mathbf{x}'\,dt' = \lambda\phi(\mathbf{x},t), \tag{3.43}$$

defined over a specific finite time interval ΔT. Here, $(\cdot)^*$ denotes the complex conjugate, V the spatial domain, and $\boldsymbol{W}(\mathbf{x})$ is a positive definite spatial weight matrix. This yields the space-time POD modes given by $\phi(\mathbf{x},t)$ that are orthogonal in the space-time inner product

$$\langle \mathbf{q}_1, \mathbf{q}_2 \rangle_{\mathbf{x},\Delta T} = \int_{\Delta T}\int_{V} \mathbf{q}_1^*(\mathbf{x},t)\boldsymbol{W}(\mathbf{x})\mathbf{q}_2(\mathbf{x},t)dV\,dt \tag{3.44}$$

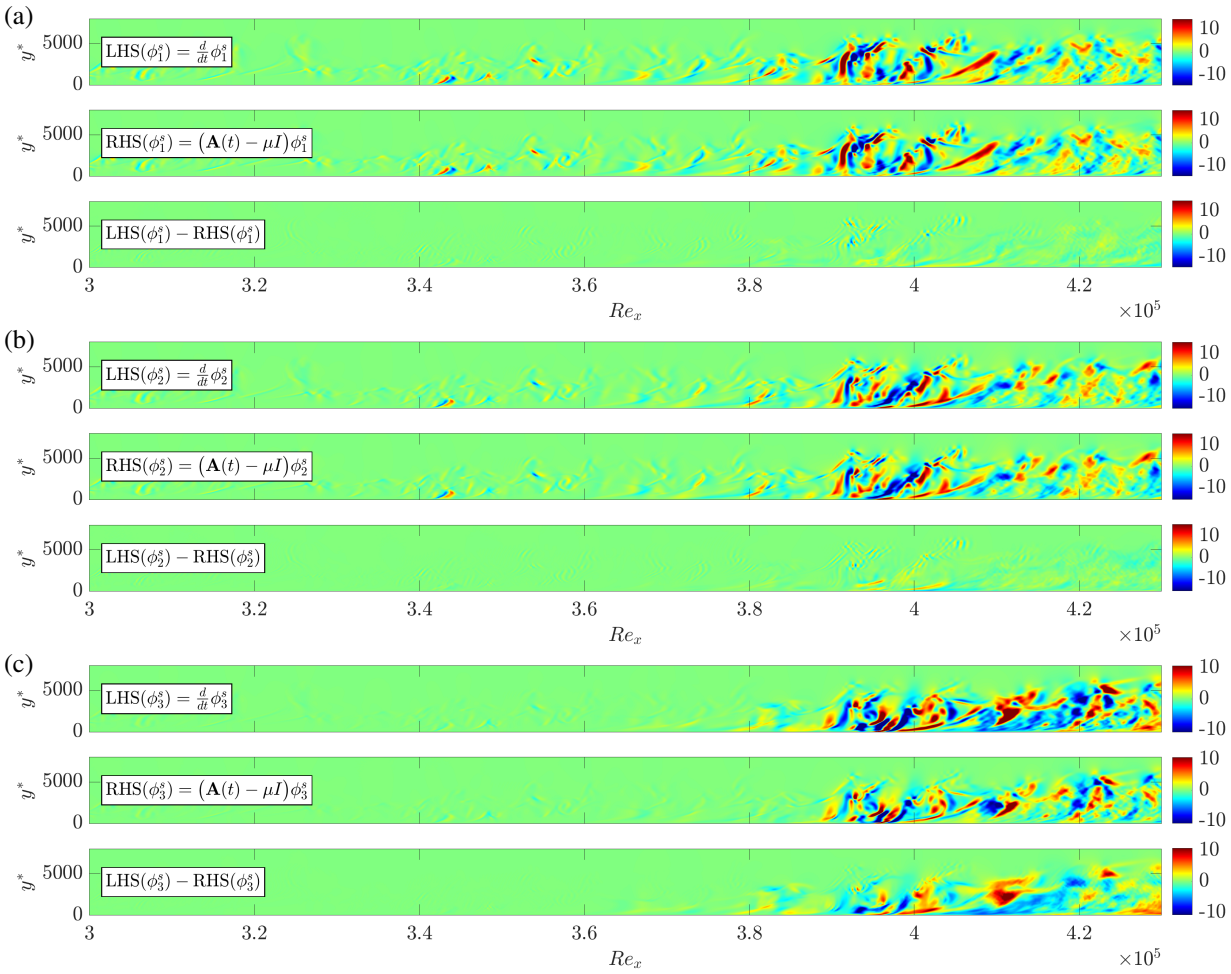


Figure 3.11. Floquet identity terms evaluated for representative symmetric STPOD modes that do (e.g. (a) ϕ_1^s and (b) ϕ_2^s) and do not (e.g. (c) ϕ_3^s and higher) satisfy the identity.

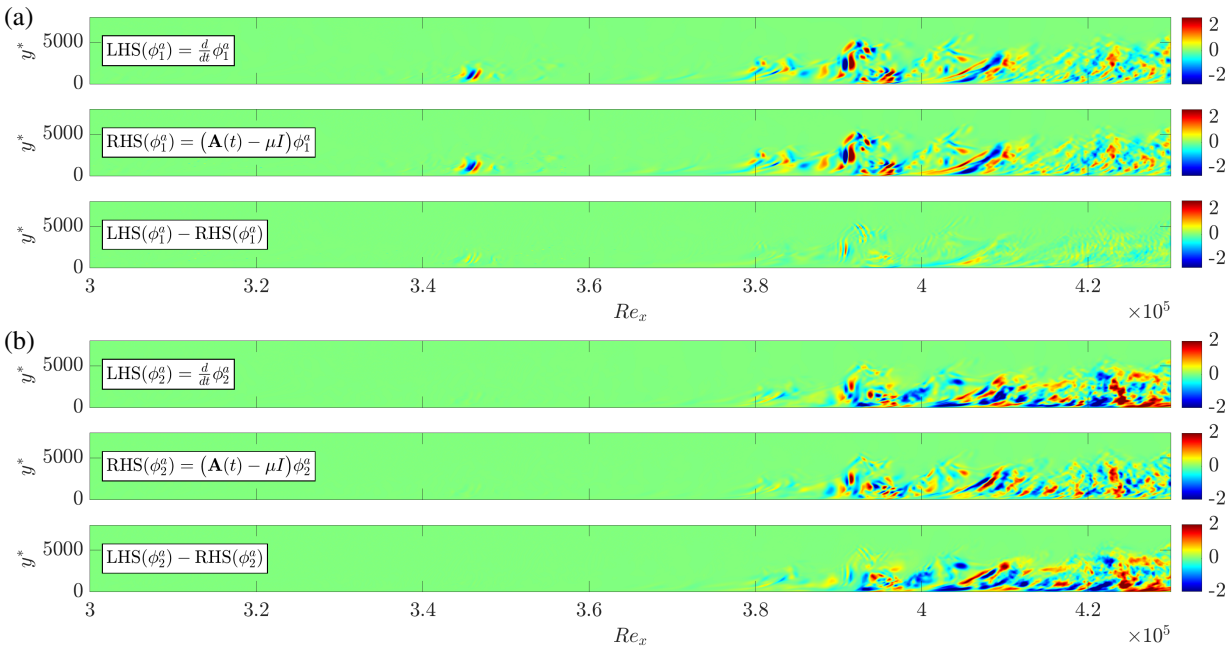


Figure 3.12. Floquet identity terms evaluated for representative anti-symmetric STPOD modes that do (e.g. (a) ϕ_1^a) and do not (e.g. (b) ϕ_2^a and higher) satisfy the identity.

and respective eigenvalues λ that maximize

$$\lambda = \frac{E\{|\langle \mathbf{q}(\mathbf{x},t), \phi(\mathbf{x},t)\rangle_{\mathbf{x},\Delta T}|^2\}}{\langle \phi(\mathbf{x},t), \phi(\mathbf{x},t)\rangle_{\mathbf{x},\Delta T}}. \tag{3.45}$$

Here, $E\{\mathbf{q}(\mathbf{x},t)\mathbf{q}^*(\mathbf{x}',t')\} = \boldsymbol{C}(\mathbf{x},\mathbf{x}',t,t')$ is the statistical estimate of the two-point space–time correlation tensor, where $\mathbf{q}(\mathbf{x},t)$ is sampled with respect to the event of interest H. Thus, in its discrete space and time equivalent the STPOD problem can be realized by the eigen-decomposition

$$\mathbf{Q}\mathbf{Q}^*\mathbf{W}\boldsymbol{\Phi} = \boldsymbol{\Phi}\boldsymbol{\Lambda} \tag{3.46}$$

where, for each realization of the event H, the snapshots of $\mathbf{q}(\mathbf{x},t)$ are stacked vertically on each other over the finite time window ΔT in the column space of $\mathbf{Q}$ and different realizations are then concatenated in row-order. For further details of the algorithm we refer to Schmidt and Schmid (2019); Frame and Towne (2023). The space-time POD modes are then coherent structures, orthogonal by construction in space and over finite time ΔT, with their evolution recovered in

the columns of ϕ each and their eigenvalues (i.e. energies) recovered in $\mathbf{\Lambda}$.

In the context of this work, ΔT spans the length of one period. We remark that STPOD is the most general method here that makes the least restrictive assumptions about the space-time signal $\mathbf{q}(\mathbf{x},t)$. There are two notable limit cases for STPOD, as recently generalized by Frame and Towne (2023): In the limit of $\Delta T \to 0$, we recover the popular "space-only" POD or "snapshot" POD (Sirovich (1987a), Aubry (1991)). In the formal limit of $\Delta T \to [-\infty,\infty]$ and assuming statistical stationarity, the STPOD problem becomes SPOD, which we will briefly introduce in the following.

3.8.4 Galilean Transformations in Boundary Layer Stability Analysis

The general framework for linear stability analysis of the full perturbation state $\boldsymbol{q}^{(n)} = [\boldsymbol{u}^{(n)}, p^{(n)}]^\top$ about its respective base velocity field $\boldsymbol{u}^{(n-1)}$ is given by the well-known linearized Navier–Stokes equations (LNSE), here written in continuous primitive-variable form:

$$\underbrace{\begin{bmatrix} I & 0 \\ 0 & 0 \end{bmatrix}}_{\mathscr{M}} \frac{\partial}{\partial t} \underbrace{\begin{bmatrix} \boldsymbol{u}^{(n)} \\ p^{(n)} \end{bmatrix}}_{\boldsymbol{q}^{(n)}} = \underbrace{\begin{bmatrix} -\big(\boldsymbol{u}^{(n-1)} \cdot \boldsymbol{\nabla}\big)\{\cdot\} - \big(\{\cdot\} \cdot \boldsymbol{\nabla}\big)\boldsymbol{u}^{(n-1)} + \nu\Delta\{\cdot\} & -\boldsymbol{\nabla}\{\cdot\} \\ \boldsymbol{\nabla} \cdot \{\cdot\} & 0 \end{bmatrix}}_{\mathscr{A}(\boldsymbol{u}^{(n-1)})\text{ LNSE operator}} \underbrace{\begin{bmatrix} \boldsymbol{u}^{(n)} \\ p^{(n)} \end{bmatrix}}_{\boldsymbol{q}^{(n)}} + \underbrace{\mathscr{N}(\boldsymbol{q}^{(n)})}_{\mathscr{O}(\varepsilon^2)} \tag{3.47}$$

where $\boldsymbol{\nabla}$ and Δ denote the spatial gradient and Laplacian, respectively, in the coordinate system $\boldsymbol{x}$, ν is the kinematic viscosity and n denotes the *order* of the perturbation analysis. As the NSE are Galilean-invariant, the flow physics do not change depending on the viewer's coordinate system, however, the mathematical structure for stability analysis has potential to be simplified by transforming to a reference frame that moves with the phase velocity of $\boldsymbol{u}^{(n-1)}$. To illustrate this, we briefly recap and compare the examples of primary ($n = 1$) and secondary ($n = 2$) boundary layer stability in two different frames of reference and then demonstrate how the same methodology is applicable to symmetry breaking.

For a Galilean transformation from laboratory coordinates (x,t) to a frame moving with

arbitrary real speed c we use

$$\underline{x} = x - ct \tag{3.48}$$

$$\underline{t} = t \tag{3.49}$$

The general transformation rule for partial derivatives with respect to any coordinate x_μ is given by

$$\frac{\partial}{\partial x_\mu} = \sum_\nu \frac{\partial \underline{x}_\nu}{\partial x_\mu} \frac{\partial}{\partial \underline{x}_\nu}, \tag{3.50}$$

thus, the transformation rules for partial derivatives are

$$\frac{\partial}{\partial x} = \frac{\partial}{\partial \underline{x}} \tag{3.51}$$

$$\frac{\partial}{\partial t} = \frac{\partial}{\partial \underline{t}} - c\frac{\partial}{\partial \underline{x}}. \tag{3.52}$$

To demonstrate how this transformation can make a difference, consider the primary linear instability (steady Blasius â†' TS wave, $n = 1$) mode ansatz in the laboratory frame:

$$\boldsymbol{q}^{(1)}(x,y,t) = \hat{\boldsymbol{q}}^{(1)}(y)\exp(i\alpha_1 x - i\omega_1 t + \mu_1 t) \tag{3.53}$$

where α_1 is the primary-wave streamwise wavenumber, ω_1 is the real temporal frequency and μ_1 is the real temporal growth rate. To transform to the moving Galilean frame, we insert $x = \underline{x} + ct$ from transformation (3.48),

$$\underline{\boldsymbol{q}}^{(1)}(\underline{x},y,t) = \underline{\hat{\boldsymbol{q}}}^{(1)}(y)e^{i\alpha_1 \underline{x}}e^{\mu_1 t}e^{i(\alpha_1 c - \omega_1)t}, \tag{3.54}$$

and observe that the oscillatory contribution cancels only for the synchronous choice $c = \omega_1/\alpha_1$. An observer moving synchronously with the TS wave no longer experiences its oscillations in time, but only observes its spatial structure $\underline{\hat{\boldsymbol{q}}}^{(1)}(y)e^{i\alpha_1 \underline{x}}$ grow or decay according to $e^{\mu_1 t}$;

otherwise, $e^{i(\alpha_1 c-\omega_1)t}$ represents residual phase drift. Regarding the mathematical structure of the LNSE, both laboratory and Galilean frame systems remain LTI for primary stability analysis, as the base velocity field is steady in both frames:

$$\text{Laboratory Frame:} \quad \boldsymbol{u}^{(0)} = U_0(y) \tag{3.55}$$

$$\text{Galilean Frame:} \quad \underline{\boldsymbol{u}}^{(0)} = U_0(y) - c. \tag{3.56}$$

For secondary stability analysis ($n = 2$, i.e. TS base flow $\rightarrow$ 3D secondary instabilities), however, the Galilean transformation fundamentally changes the mathematical nature of the stability problem. Here, Herbert (1988) introduced three key approximations:

1. The assumption of a locally parallel flow (as before)

2. A locally constant amplitude A_1 of the TS wave ($e^{\mu_1 t} \approx A_1$), justified by substantially faster growth of secondary instabilities relative to the TS base velocity field

3. The shape assumption, neglecting nonlinear distortion of the velocity distribution. Under these approximations, the base velocity field becomes

$$\boldsymbol{u}^{(1)}(x,y,t) = U_0(y) + A_1 \hat{\boldsymbol{u}}^{(1)}(y) e^{i\alpha_1 x - i\omega_1 t}. \tag{3.57}$$

Writing $x = \underline{x} + ct$, the phase transforms as

$$e^{i\alpha_1 x - i\omega_1 t} = e^{i\alpha_1 \underline{x}} e^{i(\alpha_1 c - \omega_1)t}, \tag{3.58}$$

and the base velocity field in the moving frame is

$$\underline{\boldsymbol{u}}^{(1)}(\underline{x},y,t) = U_0(y) - c + A_1 \hat{\boldsymbol{u}}^{(1)}(y) e^{i\alpha_1 \underline{x}} e^{i(\alpha_1 c - \omega_1)t}. \tag{3.59}$$

The base velocity field becomes effectively steady in the Galilean frame specifically for the

synchronous choice $c = \omega_1/\alpha_1$; otherwise $e^{i(\alpha_1 c-\omega_1)t}$ represents residual phase drift relative to the chosen moving frame. Thus, after applying the synchronous frame $c = \omega_1/\alpha_1$,

$$\underline{\boldsymbol{u}}^{(1)}(\underline{x},y) = U_0(y) - c + A_1\hat{\boldsymbol{u}}^{(1)}(y)e^{i\alpha_1\underline{x}}, \tag{3.60}$$

the base flow is *quasi-steady* in this Galilean frame.

Crucially, the Galilean transformation changes the LNSE operator from a linear time-periodic (LTP) operator in the stationary frame to a linear time-invariant (LTI) operator in the synchronous Galilean frame:

$$\text{Laboratory Frame:} \quad \mathscr{M}\frac{d}{dt}\boldsymbol{q}^{(2)} = \mathscr{A}(\boldsymbol{u}^{(1)}(t))\boldsymbol{q}^{(2)} \quad \text{(LTP)} \tag{3.61}$$

$$\text{Galilean Frame:} \quad \mathscr{M}\frac{d}{dt}\underline{\boldsymbol{q}}^{(2)} = \underline{\mathscr{A}}(\underline{\boldsymbol{u}}^{(1)})\underline{\boldsymbol{q}}^{(2)} \quad \text{(LTI)} \tag{3.62}$$

The LTI nature of the transformed system eliminates the need for a *temporal* Floquet analysis. Consequently, the mathematical structure of the secondary perturbation ansatz changes from

$$\text{Laboratory Frame:} \quad \boldsymbol{q}^{(2)}(x,y,z,t) = \hat{\boldsymbol{q}}^{(2)}(t,x,y,z)e^{\mu_2 t}e^{-i\omega_2 t} \quad \text{(Floquet mode)}, \tag{3.63}$$

where $\hat{\boldsymbol{q}}^{(2)}$ is a time-periodic Floquet mode with primary-wave period $T = 2\pi/\omega_1$, while μ_2 and ω_2 denote its real growth rate and residual frequency, respectively, to

$$\text{Galilean Frame:} \quad \underline{\boldsymbol{q}}^{(2)}(\underline{x},y,z,t) = \underline{\hat{\boldsymbol{q}}}^{(2)}(\underline{x},y,z)e^{\mu_2 t}e^{-i\omega_2 t} \quad \text{(LTI mode)} \tag{3.64}$$

a conventional LTI eigenmode in time, where modes with $\omega_2 = 0$ travel synchronously with the phase speed of the sinusoidally modulated base velocity field $\boldsymbol{u}^{(1)}$. As the base velocity field in the Galilean frame $\underline{\boldsymbol{u}}^{(1)}$ is now quasi-steady and purely periodic in $\underline{x}$ with wavelength $\lambda_x = 2\pi/\alpha_1$, it naturally suggests a *spatial* Floquet expansion for the secondary perturbation

structure $\hat{\underline{\boldsymbol{q}}}^{(2)}(\underline{x},y,z)$:

$$\underline{\boldsymbol{q}}^{(2)}(\underline{x},y,z,t) = \underbrace{\hat{\underline{\boldsymbol{q}}}^{(2)}(\underline{x},y,z)}_{\sum_m \hat{\underline{q}}^{(2),m}(y)e^{i(m\alpha_1-\delta)\underline{x}}e^{i\gamma z}} e^{\mu_2 t}\cancel{e^{-i\omega_2 t}}^{\omega_2=0}. \tag{3.65}$$

Although the ansatz theoretically allows for different modes to travel asynchronously, ultimately, Herbert (1988)'s eigenvalue analysis revealed that secondary modes naturally phase-lock to the TS wave ($\omega_2 = 0$) at sufficiently large amplitudes, as a synchronous motion maximizes energy transfer from primary to secondary perturbations, resulting in optimal amplification rates for transition. The detuning parameter δ determines the fundamental secondary instability type (harmonic K-type with $\delta = 0$, subharmonic H-type with $\delta = \frac{1}{2}\alpha_1$), while the spanwise wavenumber γ characterizes the three-dimensionality of the perturbation.

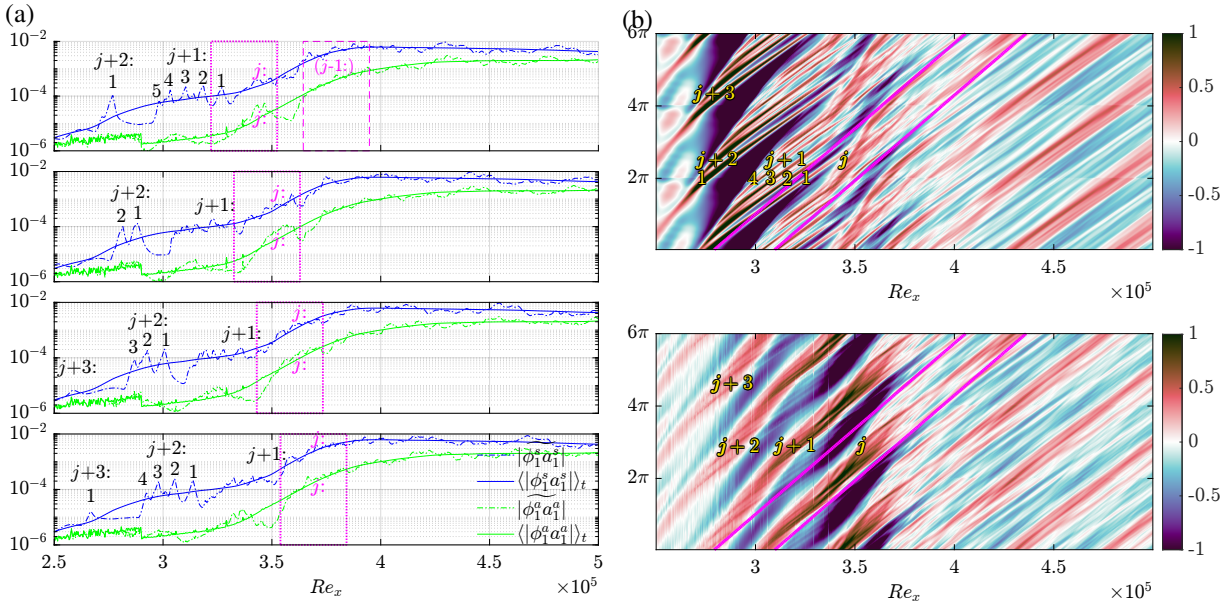


Figure 3.13. The equivalent phase-resolved amplitude and space-time diagrams to Fig. 3.5(a) and Fig. 3.5(b) created with the dominant symmetric and anti-symmetric STPOD modes ϕ_1^s and ϕ_1^a.

Acknowledgments

Chapter 3, in full, consists of the manuscript by Cong Lin and Oliver T. Schmidt, "Nature of Symmetry Breaking Seeds in Laminar–Turbulent Transition: Data-driven Stability Analysis."

The manuscript is to be submitted. The dissertation author was the primary investigator and primary author of this work.

Bibliography

R. J. Adrian. Hairpin vortex organization in wall turbulence. Phys. Fluids, 19, 2007.

Nadine Aubry. On the hidden beauty of the proper orthogonal decomposition. Theoretical and Computational Fluid Dynamics, 2(5-6):339–352, 1991.

S Bake, DGW Meyer, and U Rist. Turbulence mechanism in klebanoff transition: a quantitative comparison of experiment and direct numerical simulation. Journal of Fluid Mechanics, 459: 217–243, 2002.

D. Barkley and R. D. Henderson. Three-dimensional Floquet stability analysis of the wake of a circular cylinder. J. Fluid Mech., 322:215–241, 1996.

H. M. Blackburn, F. Marques, and J. M. Lopez. Symmetry breaking of two-dimensional time-periodic wakes. J. Fluid Mech., 522:395–411, 2005.

J. J. Bramburger, J. N. Kutz, and S. L. Brunton. Data-driven stabilization of periodic orbits. IEEE Access, 9:43504–43521, 2021.

Jason J Bramburger and J Nathan Kutz. Poincaré maps for multiscale physics discovery and nonlinear floquet theory. Physica D: Nonlinear Phenomena, 408:132479, 2020.

Guillaume A. Brès, Frank E. Ham, Joseph W. Nichols, and Sanjiva K. Lele. Unstructured large-eddy simulations of supersonic jets. AIAA Journal, 55(4):1164–1184, 2017.

S. Cherubini, P. De Palma, J.-C. Robinet, and A. Bottaro. The minimal seed of turbulent transition in the boundary layer. J. Fluid Mech., 689:221–253, 2011.

P. Cvitanović and J. F. Gibson. Geometry of the turbulence in wall-bounded shear flows: periodic orbits. Phys. Scr., 2010:014007, 2010.

Hermann F Fasel, Ulrich Rist, and Uwe Konzelmann. Numerical investigation of the three-dimensional development in boundary-layer transition. AIAA journal, 28(1):29–37, 1990.

P. Frame and A. Towne. Space-time POD and the Hankel matrix. PLoS One, 18:e0289637,

2023.

R. A. S. Frantz, J.-C. Loiseau, and J.-C. Robinet. Krylov methods for large-scale dynamical systems: Application in fluid dynamics. Appl. Mech. Rev., 75:030802, 2023.

William A Gardner, Antonio Napolitano, and Luigi Paura. Cyclostationarity: Half a century of research. Signal processing, 86(4):639–697, 2006.

J. Guckenheimer and P. Holmes. Nonlinear Oscillations, Dynamical Systems, and Bifurcations of Vector Fields. Springer, New York, 1983.

MJ Philipp Hack and Oliver T Schmidt. Extreme events in wall turbulence. Journal of Fluid Mechanics, 907:A9, 2021.

L. Heidt and T. Colonius. Spectral proper orthogonal decomposition of harmonically forced turbulent flows. J. Fluid Mech., 985:A42, 2024.

Liam Heidt and Tim Colonius. Spectral proper orthogonal decomposition of harmonically forced turbulent flows. arXiv preprint arXiv:2305.05628, 2023.

T. Herbert. Secondary instability of boundary layers. Annu. Rev. Fluid Mech., 20:487–526, 1988.

B. Herrmann, P. J. Baddoo, R. Semaan, S. L. Brunton, and B. J. McKeon. Data-driven resolvent analysis. J. Fluid Mech., 918:A10, 2021.

Abul Khair Muhammad Fazle Hussain and William C Reynolds. The mechanics of an organized wave in turbulent shear flow. Journal of Fluid Mechanics, 41(2):241–258, 1970.

Yu S Kachanov and V Ya Levchenko. The resonant interaction of disturbances at laminar-turbulent transition in a boundary layer. Journal of Fluid Mechanics, 138:209–247, 1984.

Yu S Kachanov, VV Kozlov, and V Ya Levchenko. Nonlinear development of a wave in a boundary layer. Fluid dynamics, 12(3):383–390, 1977.

Yu S Kachanov, VV Kozlov, V Ya Levchenko, and MP Ramazanov. On nature of k-breakdown of a laminar boundary layer. new experimental data. In Laminar-Turbulent Transition: Symposium, Novosibirsk, USSR July 9–13, 1984, pages 61–73. Springer, 1985.

G. Kawahara and S. Kida. Periodic motion embedded in plane couette turbulence: regeneration cycle and burst. J. Fluid Mech., 449:291–300, 2001.

Philip S Klebanoff, KD Tidstrom, and LM Sargent. The three-dimensional nature of boundary-layer instability. Journal of Fluid Mechanics, 12(1):1–34, 1962.

C. Lin and O. T. Schmidt. Modal decomposition of K-type boundary layer transition. In AIAA SCITECH 2024 Forum, page 0495, 2024. doi: 10.2514/6.2024-0495.

C. Lin and O. T. Schmidt. Boundary layer transition as succession of temporal and spatial symmetry breaking. J. Fluid Mech., 1033:R4, 2026.

Y. Liu, T. A. Zaki, and P. A. Durbin. Floquet analysis of secondary instability of boundary layers distorted by Klebanoff streaks and Tollmien–Schlichting waves. Phys. Fluids, 20:124102, 2008.

John L. Lumley. Stochastic Tools in Turbulence. Academic Press, New York, 1 edition, 1970.

I. Mezić. Analysis of fluid flows via spectral properties of the Koopman operator. Annu. Rev. Fluid Mech., 45:357–378, 2013.

A. Monokrousos, E. Akervik, L. Brandt, and D. S. Henningson. Global three-dimensional optimal disturbances in the Blasius boundary-layer flow using time-steppers. J. Fluid Mech., 650:181–214, 2010.

Akhil Nekkanti, Igor Maia, Peter Jordan, Liam Heidt, Tim Colonius, and Oliver T Schmidt. Triadic nonlinear interactions and acoustics of forced versus unforced turbulent jets. In Twelveth International Symposium on Turbulence and Shear Flow Phenomena (TSFP12), pages 19–22, 2022.

D. Rempfer and H. F. Fasel. Dynamics of three-dimensional coherent structures in a flat-plate boundary layer. J. Fluid Mech., 275:257–283, 1994a.

D. Rempfer and H. F. Fasel. Evolution of three-dimensional coherent structures in a flat-plate boundary layer. J. Fluid Mech., 260:351–375, 1994b.

P. Ricco and M. Skote. Integral relations for the skin-friction coefficient of canonical flows. J. Fluid Mech., 943:A50, 2022.

Georgios Rigas and Peter J. Schmid. Data-driven closure of the harmonic-balanced navier–stokes equations in the frequency domain. In Proceedings of the Summer Program 2022, pages 67–76. Center for Turbulence Research, Stanford University, 2022.

Georgios Rigas, Denis Sipp, and Tim Colonius. Nonlinear input/output analysis: application to boundary layer transition. Journal of Fluid Mechanics, 911, 2021.

Ulrich Rist and H Fasel. Direct numerical simulation of controlled transition in a flat-plate boundary layer. Journal of Fluid Mechanics, 298:211–248, 1995.

C. W. Rowley, I. Mezić, S. Bagheri, P. Schlatter, and D. S. Henningson. Spectral analysis of

nonlinear flows. J. Fluid Mech., 641:115–127, 2009.

Flavio Savarino, Denis Sipp, and Georgios Rigas. Optimal transitional mechanisms of incompressible separated shear layers subject to external disturbances. Journal of Fluid Mechanics, 1016:A43, 2025. doi: 10.1017/jfm.2025.10444.

Taraneh Sayadi, Curtis W Hamman, and Parviz Moin. Direct numerical simulation of complete h-type and k-type transitions with implications for the dynamics of turbulent boundary layers. Journal of Fluid Mechanics, 724:480–509, 2013.

P. J. Schmid. Dynamic mode decomposition of numerical and experimental data. J. Fluid Mech., 656:5–28, 2010.

Oliver T. Schmidt. Bispectral mode decomposition of nonlinear flows. Nonlinear Dynamics, 102:2479–2501, 2020.

Oliver T. Schmidt and Tim Colonius. Guide to spectral proper orthogonal decomposition. AIAA Journal, 58(3):1023–1033, 2020.

Oliver T Schmidt and Peter J Schmid. A conditional space–time pod formalism for intermittent and rare events: example of acoustic bursts in turbulent jets. Journal of Fluid Mechanics, 867: R2, 2019.

Lawrence Sirovich. Turbulence and the dynamics of coherent structures. i. coherent structures. Quarterly of applied mathematics, 45(3):561–571, 1987a.

Lawrence Sirovich. Turbulence and the dynamics of coherent structures. ii. symmetries and transformations. Quarterly of Applied mathematics, 45(3):573–582, 1987b.

M. K. Sleeman, M. T. Lakebrink, and T. Colonius. Simulation of K-Type and H-Type Transition Using the Nonlinear One-Way Navier–Stokes Approach. In Proceedings of the 10th IUTAM Symposium on Laminar–Turbulent Transition, pages 143–149. Springer, 2026. doi: 10.1007/978-981-96-9829-5_19.

Aaron Towne, André V. G. Cavalieri, Peter Jordan, Tim Colonius, Oliver Schmidt, Vincent Jaunet, and Guillaume A. Brès. Acoustic resonance in the potential core of subsonic jets. Journal of Fluid Mechanics, 825:1113–1152, 2017.

Aaron Towne, Oliver T. Schmidt, and Tim Colonius. Spectral proper orthogonal decomposition and its relationship to dynamic mode decomposition and resolvent analysis. Journal of Fluid Mechanics, 847:821–867, 2018.

J. H. Tu. Dynamic mode decomposition: Theory and applications. PhD thesis, Princeton University, 2013.

M. Tutkun and W. K. George. Lumley decomposition of turbulent boundary layer at high Reynolds numbers. Phys. Fluids, 29:025108, 2017.

D. Viswanath. Recurrent motions within plane couette turbulence. J. Fluid Mech., 580:339–358, 2007.

Peter Welch. The use of fast fourier transform for the estimation of power spectra: a method based on time averaging over short, modified periodograms. IEEE Transactions on audio and electroacoustics, 15(2):70–73, 1967a.

Peter D. Welch. The use of fast fourier transform for the estimation of power spectra: A method based on time averaging over short, modified periodograms. IEEE Transactions on Audio and Electroacoustics, 15(2):70–73, 1967b.

Frank M White. Viscous fluid flow, volume 3. McGraw-Hill New York, 2006.

Xiaohua Wu and Parviz Moin. Direct numerical simulation of turbulence in a nominally zero-pressure-gradient flat-plate boundary layer. Journal of Fluid Mechanics, 630:5–41, 2009.

Xiaohua Wu and Parviz Moin. Transitional and turbulent boundary layer with heat transfer. Physics of Fluids, 22(8), 2010.